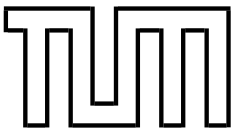

Fakultät für Physik
der Technischen Universität München

Max-Planck-Institut für Biochemie Abteilung
für Molekulare Strukturbiologie

Development and applications of a phase contrast method for cryo-electron microscopy

Maryamsadat Khoshouei Esfahani

Vollständiger Abdruck der von der Fakultät für Physik der
Technischen Universität München
zur Erlangung des akademischen Grades eines
Doktors der Naturwissenschaften (Dr. rer. nat.)
genehmigten Dissertation.

Vorsitzender:	Prof. Dr. Andreas Bausch
Prüfer der Dissertation:	1. Hon.-Prof. Dr. Wolfgang Baumeister
	2. Prof. Dr. Martin Zacharias

Die Dissertation wurde am 11.10.2018 an der Technischen Universität München eingereicht und durch die Fakultät für Physik am 06.11.2018 angenommen

Contents

List of figures

List of tables

Abstract

Phase contrast has been used in light microscopy for more than 80 years. It has also become an essential method in cryo-electron microscopy (cryo-EM) for the imaging of unstained biological samples. Traditionally, phase contrast in cryo-EM is produced by defocusing the objective lens. This approach has several drawbacks, the main being relatively poor performance for low spatial frequencies which results in overall low image contrast. To address this issue, a new generation of thin film phase plate was developed in 2014, called the Volta phase plate (VPP), at the Max-Planck Institute of Biochemistry in Martinsried, Germany. The VPP is nowadays routinely used for data collection in the two, main 3D cryo-EM fields, single particle analysis (SPA) and cryo-electron tomography (CET).

At the current level of technology, some protein complexes still remain challenging for conventional SPA. In this thesis, VPP was used to determine the structures of rather difficult samples which have not been solved to date. The structures of human peroxiredoxin-3, a class B GPCR-G-protein complex and human haemoglobin with a molecular weight of 64 kDa were solved using the VPP. Furthermore, 2D classes of myoglobin with a molecular weight of 17 kDa were shown. The smallest protein structure successfully solved by conventional SPA is that of isocitrate dehydrogenase with a molecular weight of 93 kDa at 3.8 Å resolution. The results presented here suggest that VPP is beneficial for the study of small protein complexes, such as membrane receptors, and thus could contribute in the long run to structure-based drug design.

The VPP was also applied to CET. One of the model systems used to evaluate the performance of the VPP was earth worm sperm *Lumbricus terrestris*. VPP imaging was used to elucidate morphological and ultrastructural details of the sperm cells. Individual compartments of the cells were imaged with high contrast providing new information about their organization and structure.

Subtomogram averaging is a technique which applies averaging methods to CET data in order to improve the signal-to-noise ratio (SNR) and the resolution. Ice-embedded *in vitro* mammalian 80S ribosomes were used to evaluate and compare the subtomogram averaging performance of the VPP with the conventional defocus method. These results indicated a benefit of using the VPP by an overall improved performance in the particle alignment and more uniform spectral information coverage.

This thesis provides clear evidence of the advantages offered by the VPP in the two major cryo-EM 3D structure determination techniques, SPA and CET. The high contrast provided by the VPP could make it an

ideal tool for quick sample screening, initial model building and/or structure determination of challenging and small complexes at near atomic resolutions. In addition, VPP can facilitate structure determination of important pharmacological targets that control various physiological functions and are relevant for the treatment of some chronic diseases such as diabetes, cancer, migraine and obesity.

Zusammenfassung

Seit mehr als 80 Jahren wird der Phasenkontrast in der Lichtmikroskopie eingesetzt. Auch in der Kryo-Transmissionselektronenmikroskopie (Kryo-EM) ist der Phasenkontrast unverzichtbar für die Abbildung nicht-kontrastierter biologischer Proben. Üblicherweise wird der Phasenkontrast in der Kryo-EM durch Defokussieren der Objektivlinse erzeugt. Dieser Ansatz hat jedoch mehrere Nachteile, vor allem die relativ schwache Übertragung niedriger Ortsfrequenzen, was zu einem insgesamt schwachen Bildkontrast führt. Um dieses Problem zu umgehen wurde seit 2012 am Max-Planck-Institut für Biochemie in Martinsried eine neue Generation von Dünnfilm-Phasenplatten entwickelt, die Volta Phasenplatte (VPP). Die VPP findet heute routinemäßige ihre Anwendung in den beiden Hauptbereichen der dreidimensionalen (3D) Kryo-EM, der Einzelpartikelanalyse (SPA) und der Kryo-Elektronentomografie (CET).

Selbst auf dem heutigen Stand der Technik sind einige Proteinkomplexe noch immer eine Herausforderung für die konventionelle Einzelpartikelanalyse. In dieser Dissertation wurde die VPP verwendet, um die Strukturen schwieriger Proben zu bestimmen, die bisher nicht gelöst wurden. So gelang die Strukturbestimmung des humanen Peroxiredoxin-3, einem Klasse B GPCR Proteinkomplexes und des humanen Hämoglobins mit einem Molekulargewicht von 64 kDa durch die Anwendung der VPP. Darüber hinaus gelang die Darstellung zweidimensionale Klassen von Myoglobin mit einem Molekulargewicht von 17 kDa. Zum Vergleich, die kleinste Proteinstruktur, die bisher durch konventionelle Einzelpartikelanalyse erfolgreich bestimmt werden konnte, ist die der Isocitrat-Dehydrogenase mit einem Molekulargewicht von 93 kDa bei einer Auflösung von 3.8 A. Die hier vorgestellten Ergebnisse deuten darauf hin, dass die VPP für die Untersuchung von kleinen Proteinkomplexen, wie z.B. membranständigen Rezeptoren vorteilhaft ist und somit langfristig zum strukturbasierten Wirkstoffdesign beitragen könnte.

Auch in der Kryo-Elektronentomografie fand die VPP ihre Anwendung. Eines der Modellsysteme zur Bewertung des Nutzens der VPP waren Spermien von Lumbricus terrestris. Mit Hilfe der VPP konnten sowohl morphologische als auch ultrastrukturelle Details dieser Spermien kontrastreich abgebildet werden und ergaben neue Einblicke in ihre Organisation und Struktur.

Subtomogram averaging (Mittelung von repetitiven Strukturen innerhalb eines oder mehrerer Tomogramme) ist eine Methode, um das Signal-Rausch-Verhältnis und damit die Auflösung innerhalb eines Tomogramms zu verbessern. In Eis eingebettete *in vitro*-Proben von 80S-Ribosomen aus Säugerzellen wurden verwendet, um das Leistungsvermögen der VPP im Zusammenhang mit subtomogram averaging zu testen und mit der konventionellen Defokusmethode zu vergleichen. Die so

erhaltenen Ergebnisse zeigten eine Verbesserung bei Verwendung der VPP vor allem in der Partikelalignierung durch eine einheitlichere Abdeckung des Bild-Signals über alle Raumfrequenzen.

Diese Dissertation stellt die Vorteile dar, die die VPP in den beiden Hauptbereichen der dreidimensionalen Strukturbestimmung durch Kryo-EM bietet. Die Bild-Kontraststeigerung macht die VPP zum idealen Hilfsmittel für das schnelle Probensichten bzw. “screenen”, für die initiale Modellentwicklung und/oder für die Strukturbestimmung von kleinen Proteinkomplexen bei nahezu atomarer Auflösung. Darüber hinaus kann VPP die strukturelle Bestimmung wichtiger pharmakologischer Ziele erleichtern, die verschiedene physiologische Funktionen steuern und für die Behandlung einiger chronischer Krankheiten wie Diabetes, Krebs, Migräne und Adipositas relevant sind.

1. Introduction

Light microscopes (LM) and electron microscopes (EM) share various common concepts in terms of Fourier optics and image formation. In general, the wave at the back-focal plane (diffraction plane) of the objective lens can be calculated as a Fourier transform of the object wave coming from a specimen. At the back-focal plane, the wave is modulated by the contrast transfer function (CTF) which congregates the effects of various optical aberrations. By taking another Fourier transform of the wave at the diffraction plane the image wave and consequently the image intensity can be calculated.

One of the illumination modes in LM for enhancement and modification of image contrast is the phase contrast method. Phase contrast has been in use in LM for about hundred years for imaging of unstained biological specimens. It is produced and based on different refractive indices between specimen structures and the surrounding medium in such a way that light is differently bend and delayed through the different materials. This results in a diffracted light wave from the specimen that is 90 ° retarded relative to the not diffracted light wave.

The phase contrast concept was proposed for EM by introducing additional hardware located at the back focal plane of the objective lens. The theoretical aspects are similar to those used in LM. However, implementation of hardware in EM is more challenging, because of manufacturing and operational difficulties.

In general phase plates are tools for enhancing the contrast of low contrast biological and especially radiation sensitive frozen-hydrated specimens which mainly consist of light elements. Weak phase objects modify the phase of the electron wave only weakly and produce an almost negligible amount of spatial modulation of the amplitude of the electron wave. Therefore, it would be desirable to produce an additional phase contrast by modulating the diffraction wave to allow the extraction of a maximum of the image information in cryo-EM from biological specimens.

In this chapter, a brief description of light microscopy is presented in section 1.1 followed by a detailed introduction to electron microscopy in section 1.2. Section 1.2 also introduces the two most common methods for 3D structure determination by EM, namely SPA and CET. The last subsection describes different types of phase plates with emphasis on the thin film phase plates.

1.1. Light microscopy

Light microscopy is a fundamental imaging technique for the direct visualization of structures down to the sub-micrometer scale. Light microscopes allow the study of fully hydrated biological specimens in their native and dynamic state. Furthermore, various contrast and labeling methods have been developed in light microscopy which greatly enhanced the capabilities of the technique. The idea of phase contrast was first proposed by Fritz Zernike in 1942 for observing transparent objects (Zernike, 1942). In phase contrast imaging, contrast arises from different refractive indices stemming from the specimen material and its surrounding medium: diffracted light becomes retarded in phase relative to unscattered light. However, the resolution in LM is by-and-large diffraction-limited by the wavelength of light to about 200-300 nm in the lateral direction and 500-700 nm in the axial direction. Amongst LM techniques, fluorescence microscopy provides observation of specific cellular components through specific labeling in real time manner. In the last couple of years super-resolution fluorescence microscopy techniques became available which bypassed elegantly the diffraction limitation thus improving the spatial resolution in all three dimensions. Nowadays it is possible to reach molecular scale resolution by using super-resolution fluorescence microscopy but at the expense of being affected from labeling density, probe size, laser power and how well the labeled ultrastructures can be preserved (Huang et al., 2009),(Hoppert, 2005b).

1.2. Electron microscopy

Electron microscopy has two main modalities – scanning electron microscopy (SEM) and transmission electron microscopy (TEM). As the name suggests, SEM is based on scanning the sample with a focused electron beam (probe) and is typically used for surface observations of inorganic and organic materials. Biological samples are not the main area of SEM applications. SEM can generate topographic images and elemental composition maps. It is also part of the cryo-focused ion beam (cryo-FIB) approach for preparing thin slices of cellular specimens for cryo-transmission electron microscopy (cryo-TEM) (Williams, 2009). The interaction of the electron beam with the sample produces secondary electrons, back scattered electrons, x-rays and photons which can be detected during the scan to generate an image. The resolution of SEM is limited by the interaction volume of the focused beam with the sample surface and it typically in the nanometer range (Goldstein et al., 2003). In TEM, on the other hand, electrons are transmitted through thin specimens and their interaction with the sample material produce an image with

high resolution information. One of the applications of TEM is so called cryo-EM to study biological specimens in a frozen-hydrated state at liquid nitrogen temperature. The sample thickness has to be less than 0.5 µm to be electron transparent for 300 keV electrons, which is even less for the microscopes having lower beam energies, respectively acceleration voltages. However, resolution in cryo-EM was limited by the sample's sensitivity to radiation resulting in 'low-contrast' images, sample and beam-induced motion and the low-speed and sensitivity of the detection devices and only occasionally reached a resolution in the sub-nanometer range. However, recently cryo-EM has experienced a "resolution revolution" due to technical advances in direct electron detection, stable and automated microscopes and stages that improved the attainable resolution in a profound manner (Kuhlbrandt, 2014; Nogales, 2016).

Scanning transmission electron microscopy (STEM) is a third modality of EM on thin samples. It is based on scanning with a fine focused beam and using the transmitted signal to generate the images. In STEM transmitted radiation is detected from both, scattered or unscattered events by using disk-shaped detectors for the bright or dark-field signals. Unlike defocused based TEM which requires phase-coherence to generate phase contrast, STEM is using the amplitude signal and allows imaging of much thicker specimens. STEM has shown its ability in bringing up high resolution structures in material science such as semiconductor devices, batteries and catalysts however no high-resolution structure is reported up to date using cryo-STEM (Elbaum et al., 2016; Wolf et al., 2014).

The TEM concept and the underlying principles of electron-specimen interactions will be the focus of the next section.

1.2.1. Electron-specimen interactions

Electrons interact with the specimen elastically and inelestically. The elastic scattering does not involve energy transfer and is based on the interaction of the incident electron with the electrostatic Coulomb potential of atoms and molecules present in the sample. Elastic scattering is the principle source of high-resolution image contrast in cryo-EM (Förster et al., 2012). On the other hand, inelastic scattering transfers energy from the incident electrons to the sample and is the origin of radiation damage through chemical bond breakage and free radical creation. In that context, the ratio of elastic scattered electrons to inelastic scattered electrons should be high to obtain sufficient high-resolution information, which in turn requires thin specimens (Förster et al., 2012; Reimer and Kohl, 2008). The following inelastic excitations may occur (Reimer and Kohl, 2008):

1- Phonon excitation and excitation of oscillations in molecules. The energy loss of these is in the range of 20 meV to 1 eV. This excitation has no practical interest for biological electron microscopy. It can be observed after monochromatization of the primary electron beam and is more important for studies in material science and solid-state physics.
2- Intra- and interband excitation of outer atomic electrons as well as collective oscillations of the conduction or valence electrons (plasmons). It has an energy-loss in the range of 3 eV to 25 eV.
3- Electron ionization from inner atomic shells to a non-occupied energy state above the Fermi level. Secondary electrons are the result of this ionization event.

Electrons with kinetic energy of 300 keV and wave length of around 2 pm have an inelastic mean-free path of 100-200 nm which represents the average distance between two scattering events. The mean-free path is inversely proportional to the inelastic scattering cross section multiplied by the density of atoms along the beam path.

1.2.2. Transmission electron microscope

EM and LM are based on the same optical principles and are built from similar optical elements, i.e. lenses. In light microscopy the lenses are made from transparent materials, such as glass. In electron microscopy the lenses are magnetic coils arranged vertically along a high vacuum tube (i.e. column) in which the electron beam propagates (Hoppert, 2005a). The wavelength of electrons is five orders of magnitude shorter than that of visible light. Therefore, theoretically it should be possible to reach a much higher resolution. However, electrons interact much stronger with the sample and can therefore cause damage that prevents the use of high exposure times and limits the final SNR in the images. The main building blocks of a TEM from top to bottom are:

Electron gun: This is the source of the electron beam. Electrons are emitted from a sharp tip and are then accelerated to their final energy by an electrostatic linear accelerator. The main characteristics of the electron gun are the energy spread and brightness. Those properties determine the temporal (energy spread) and spatial (brightness) coherency of the beam. Field emission guns provide high spatial coherency and are currently the standard type of source used for high resolution imaging (Hoppert, 2005a).

Condenser lenses: Condenser lenses form the illumination on the sample. There are usually two or three condenser lenses in a TEM illumination system. The first lens creates a de-magnified image of the source. The second and the third lenses control the beam convergence angle and the beam diameter on the

specimen. A third condenser lens allows independent control of the convergence angle and beam diameter and is therefore used to maintain parallel illumination on the sample. A three-condenser lens TEM was used for all experiments presented in this thesis, except for the experiments related to the development of the phase plate.

Objective lens, objective aperture and phase plate: Similar to light microscopy, the objective lens in a TEM is the most important lens and its characteristic determines the overall performance of the microscope. After passing through the specimen the beams of scattered and unscattered electrons are focused by the objective lens at the back-focal (diffraction) plane. An objective aperture or a phase plate can be positioned at the back-focal plane. An objective aperture intercepts high-angle scattered electrons, that do not contribute information to the image, and thus generates scattering amplitude contrast. A phase plate introduces a phase shift between the scattered and unscattered beams and generates phase contrast (Hoppert, 2005a; Reimer and Kohl, 2008; Williams, 2009).

Image forming lenses: Several intermediate lenses exist below the objective lens to magnify the image coming from the objective lens. Moreover, a number of projector lenses magnify the image further until it reaches the detection device, e.g. camera (Hoppert, 2005a; Reimer and Kohl, 2008; Williams, 2009).

Camera: The detector performance has been a major limiting factor for cryo-EM in the past three decades. During this time there was a gradual evolution of the technology. It started with photographic film which was not usable for automatic data collection. Charged coupled device (CCD) cameras were introduced in the 1990s and for the first time allowed the computer controlled and automated data collection. However, CCDs had a poor detection yield (detection quantum efficiency, DQE) and a very limited transfer compared to film. The main reason for the poor performance was the scintillator layer to decelerate the electrons and to convert the electron signal to photons and the fiber optical stack, where a lot of signal was lost. A few years ago, a new type of detector was developed to circumvent the conversion of electrons into photons and directly detect the incoming electrons. It is based on complementary metal-oxide-semiconductor (CMOS) technology with the ability of a fast and direct readout. Current models can read out up to 1500 frames per second. This read-out speed and the chips internal architecture allows for individual electron counting which significantly improves the SNR. Moreover, sample and beam-induced specimen motion can be compensated through alignment of individual frames for further improving the detectors performance. With those capabilities, direct electron detectors opened a new era in cryo-EM with various near atomic resolution structures up to date. Direct detection device (DDD) cameras are now

the basis for a high-performance platform (Bai et al., 2015a; Li et al., 2013; McMullan et al., 2014; Zheng et al., 2017).

1.2.3. Image formation principles in TEM

Elastic scattering of electrons by the specimen manifests phase shift in the object wave below the specimen. The phase shift is proportional to the integrated Coulomb potential along the beam path (Frank, 2006):

$$\varphi(\boldsymbol{r}) = \int c(\boldsymbol{r}, z)dz. \quad (1)$$

In this formula $\boldsymbol{r}$ is a 2D vector, c is the 3D Coulomb potential distribution within the object (micrographs are line projections of the Coulomb potential). The incident plane wave ψ_0 is modulated by the phase shift and produces the object wave (Frank, 2006):

$$\Psi(\boldsymbol{r}) = \psi 0 exp[i\varphi(\boldsymbol{r})]. \quad (2)$$

In a weak-phase object approximation, which is applicable to thin samples consisting of light elements (such as frozen organic matter), the phase shift is small ($\varphi(\boldsymbol{r})$<< 1) and the object wave can be simplified to the first two terms of the Taylor expansion:

$$\Psi(\boldsymbol{r}) = \psi 0[1 + i\varphi(\boldsymbol{r})], \quad (3)$$

Where the object wave comprises the incoming wave "1" and the scattered wave $i\varphi(\boldsymbol{r})$. If the phase of the scattered wave is shifted by 90° the resulting image intensity shows positive phase contrast. If the scattered wave is phase shifted by -90° the resulting image intensity will be larger than the initial intensity which produces negative phase contrast (Frank, 2006; Reimer and Kohl, 2008).

If $\Psi(\boldsymbol{r})$<< $\psi 0$ the object wave amplitude is approximately the same as that of the incoming wave therefore weak phase objects are not visible in the image. Traditionally in order to visualize such objects optical aberrations are used to introduce additional phase shift to the scattered wave. The main such aberrations are spherical aberration and intentional defocus of the objective lens (ignoring the effect of astigmatism) (Frank, 2006):

$$\chi(\mathrm{k}) = \frac{-1}{2}\,\Delta z\lambda k^2 + \frac{1}{4}\,\lambda^3 \mathrm{C_s} k^4 \quad (4)$$

$$\gamma(k)A = 2\pi\chi(\mathrm{k}),$$

where λ is the electron wavelength, Δz is the defocus, C_s is the spherical aberration, χ(k) is the wave aberration function, k is the amplitude of the spatial frequency and $\gamma(k)$ is the induced phase shift.

The wave function in the back focal plane of the objective lens then becomes (Frank, 2006; Reimer and Kohl, 2008):

$$\Psi\mathrm{bf}(\boldsymbol{K}) = \mathrm{F}\big(\psi\mathrm{sc}(\mathbf{r})\big)\exp\,[\mathrm{i}\,\gamma(\mathbf{k})], \tag{5}$$

Where $\mathrm{F}\big(\psi\mathrm{sc}(\mathbf{r})\big)$ is the Fourier transform of the scattered wave. The wave function in the image plane will be then (Frank, 2006):

$$\Psi\mathrm{ip}(\boldsymbol{r}) = F^{-1}\big(F\big(\psi sc(\boldsymbol{r})\big)A(\mathbf{k})\big]exp\,[i\,\gamma(\boldsymbol{k})]. \tag{6}$$

The wave function in the image plane is already modified by an aperture function $A(\mathbf{k})$ (Frank, 2006):

$$A(\mathbf{k}) = \begin{cases} 1\,, & for\ |k| = \frac{\theta}{\lambda}, \theta \leq radius\ of\ objective\ aperture \\ 0, & for\ |k| = \frac{\theta}{\lambda}, \theta > radius\ of\ objective\ aperture \end{cases} \tag{7}$$

The intensity in the image plane is (Frank, 2006):

$$I(\boldsymbol{r}) = |\Psi\mathrm{ip}(\boldsymbol{r})|^2. \tag{8}$$

In the case of a weak phase object it can be shown that the image intensity is approximately:

$$I(\boldsymbol{r}) \approx 1 - 2\mathcal{F}^{-1}\{\Phi(\boldsymbol{k})\sin(\gamma(k))\}, \tag{9}$$

Where $\Phi(\boldsymbol{k})$ is the Fourier transform of the object phase $\varphi(\boldsymbol{r})$. The sine part in the above equation is the phase contrast transfer function (CTF):

$$CTF(k) = \sin(\gamma(k)) = \sin\left[2\pi\left(-\tfrac{1}{2}\Delta z\lambda k^2 + \tfrac{1}{4}C_S\lambda^3k^4\right)\right]. \tag{10}$$

The introduction of a phase plate adds a phase shift term into the argument of the sine:

$$CTF_{PP}(k) = \sin\left[2\pi\left(-\tfrac{1}{2}\Delta z\lambda k^2 + \tfrac{1}{4}C_S\lambda^3k^4\right) + \varphi_{PP}\right], \tag{11}$$

where φ_{PP} is the additional phase shift of the phase plate.

In the above section where the concept of phase contrast was shortly explained there is also a minor contribution from amplitude contrast in the image formation. Amplitude contrast comes from two possible sources; from high angle elastically scattered electrons intercepted by the aperture or

idealistically scattered electrons removed by an energy filter. For ice-embedded biological samples amplitude contrast is very small (less than 10%) (Frank, 2006).

The CTF performance in terms of information transfer is influenced by three factors (Frank, 2006; Williams, 2009):

1- **Aperture effect**: If the objective aperture is not large enough it will intercept electrons above a certain spatial frequency and thus limit the resolution of the image. Therefore, the diameter of the aperture has to be large enough to accommodate the expected information limit of the image.
2- **Envelope function**: The CTF envelope is affected by the partial coherence of the electron source. The source size is finite (spatial coherence) and it has an energy spread (temporal coherence). Combined with the chromatic aberration of the objective lens this partial coherence reduces the CTF amplitude at high spatial frequencies thus limiting the performance.
3- **Optical aberrations:** The spherical aberration, defocus, astigmatism and most importantly coma aberration can limit the high-resolution performance further.

The amount of defocus is a key parameter in order to reach a certain resolution. Figure 1 shows the CTF simulation for a phase plate with 90° phase shift at three different defocus values after considering the effect of spherical aberration. The resolution criterion is when the CTF amplitude drops below 0.5. By slightly increasing the defocus value, the resolution becomes better than for the in-focus case but at higher defocus values there is a drop in the flat part of CTF, which becomes the new resolution limit. Figure 1B shows resolution versus defocus diagrams. The shaded areas refer to defocus values where the CTF amplitude is below 0.5 and the corresponding resolution is impossible to reach. Therefore, the resolution is very sensitive to even few nm defocus deviations. Figure 1C shows the resolution behavior versus intended defocus for three different phase shifts and Figure 1D illustrates resolution versus defocus for a Cs corrected microscope where there is slightly more freedom in terms of defocus variation. Theoretically, it should be possible to obtain a higher resolution structure using a phase plate and the in-focus (focusing precisely) procedure in combination with a Cs-corrected microscope (Danev and Baumeister, 2016). In theory obtaining high resolution structure using in-focus VPP scheme is possible but the permitted defocus range becomes narrower compared to the defocused VPP data acquisition. Therefore, in practice it is almost impossible to reach below 2Å resolution because of required high focusing accuracy during the data acquisition. However, this experiment is pending and still needs to be performed.

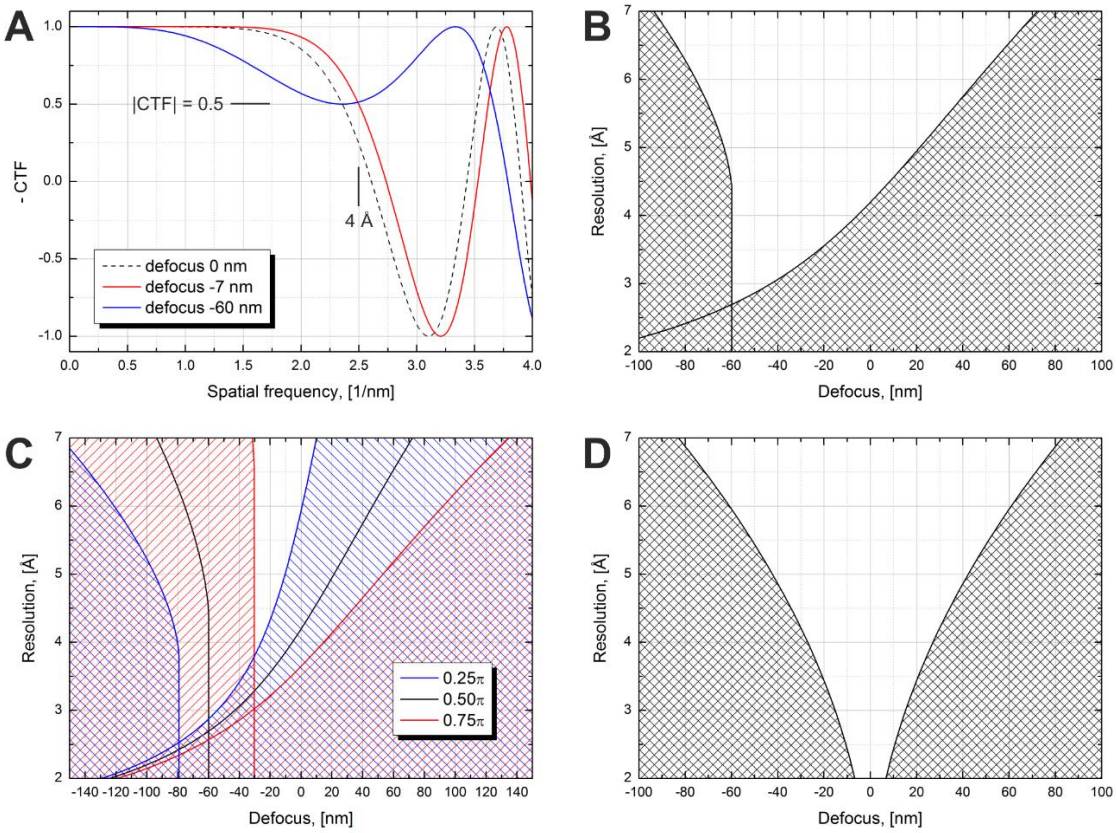

Figure 1: VPP simulated CTFs and resolution versus defocus with a criterion of CTF amplitude dropping below 0.5. (A) Simulated CTFs with three different defocus values and a phase shift of π /2 showing the possible defocus range to achieve 4 Å resolution for SPA. Dashed curve shows spherical aberration effect at zero defocus. In the presence of a small defocus, CTF drops below 0.5 at a resolution better than 4 Å (blue curve). (B) Resolution versus defocus showing the usable defocus range in order to reach a certain resolution. The prohibited areas are shaded (criterion is when |CTF|=0.5, the phase shift is π/2 and the spherical aberration is 2.7 mm). (C) Shows three different resolutions versus defocus curves for three different phase shifts. (D) The same as (B) but for Cs-corrected microscope. Figure was adapted from (Danev and Baumeister, 2016).

1.2.4. Phase contrast transmission electron microscope

Phase plates for TEM were initially proposed by Boersch after being used successfully for light microscopy (Boersch, 1947). The theoretical principles are the same except that the implementation of phase plates for EM is practically much more challenging. The phase plate is an additional hardware mounted in the back focal plane of the objective lens of the TEM. It produces more contrast and thus improves the SNR for radiation sensitive specimens. In general, there are two ways of generating phase contrast for cryo-samples. The first, conventional transmission electron microscopy approach (CTEM), utilizes inherent aberrations (spherical aberration) and induced aberrations (defocus) of the microscope resulting in image intensity variations as a function of phase variations in the object wave. The drawback of this approach is the loss of phase information in the low frequency region. The second approach utilizes an additional

phase shift introduced by a phase plate. Phase plates provide very good performance at low frequencies and, in principle, do not require defocus to generate phase contrast (Danev and Nagayama, 2010).

There are two types of phase plates for TEM depending on the symmetry of the modulation pattern they produce. The first type is the so-called Hilbert phase plate, which modulates the diffracted wave asymmetrically producing anisotropic contrast in the image. The second type is the Zernike phase plate (ZPP) which produces circularly symmetric modulation pattern leading to an isotropic image contrast. An ideal ZPP has a phase shift of -π/2 (90 °) and thus changes the conventional TEM sine-type CTF to a cosine-type, therefore both CTFs are complementary. The phase plate CTF starts at a frequency called the "cut-on" frequency:

$$k_0 = \frac{r_0}{\lambda f}. \tag{12}$$

The formula above shows the relation between the cut-on frequency k_0, the real space distance from the center of the diffraction plane (r_0), the electron wave length (λ) and the focal length of the objective lens (f). In the case of a ZPP, r_0 is the radius of the central hole of the phase plate. Good information transfer started at the cut-on frequency which is usually much lower than the lowest frequencies imaged by conventional defocus phase contrast. By varying the defocus value some low frequency information can be retrieved but at the expense of rapid CTF oscillations at higher frequencies (Danev and Nagayama, 2010; Nagayama and Danev, 2009).

Over the years, phase plates designs based on various technologies have been proposed, such as thin film, electrostatic, magnetic, photonic, anamorphotic and electrostatic mirror (Danev and Nagayama, 2010). Below are those phase plate types briefly described, which got the most practical attention or which hold the biggest promise for a success in future. The thin film phase plate is described in more details because it is the base of the newly developed phase plate and used in this thesis.

Electrostatic phase plates: This type consists of three consecutive ring-shaped electrodes similar to the Einzel-lens proposed by Boersch in 1947 (Boersch, 1947). It is positioned on the zero-order diffraction beam and electrons passing through the lens experience a phase shift proportional to the voltage applied on the central electrode. The central electrode is surrounded by two outer electrodes at ground potential. The main advantages of these phase plates are the real-time control of the phase shift with the applied voltage and no signal loss at high spatial frequencies. However, a big practical disadvantage is the presence of solid structural elements in the bam path that are very susceptible to beam induced contamination and electrostatic charging (Danev and Nagayama, 2010).

Photonic phase plates: This design uses a high intensity focused laser in the path of the electron beam. Electrons passing through the laser focus are affected by the intense oscillating electric field which leads to an elongation of their optical path and therefore a phase shift. The main challenge in the practical realization of photonic phase plates is that they require high light/laser intensity. One possible solution is to use an optical resonance cavity for amplification. There are several practical advantages of the photonic phase plate, such as no materials and related difficulties in the electron beam path, and the possibility of real-time control of the phase shift. At present there are no working prototypes but the first proof of principle experiments are promising and a usable prototype is expected in the very near future (Danev and Nagayama, 2010; Müller et al., 2010; Schwartz et al., 2016).

Thin film phase plates: The type with the longest experimental history is the thin film phase plates. Boersch suggested this type of phase plate in 1947 (Boersch, 1947). The ZPP made of a thin film with a small hole in the middle is the first proposed thin film phase plate. In early experiments phase plates were made of collodion film which had a poor performance. Collodion film is a non-conductive polymer which will be strongly charged when inserted in the electron beam path. Later, amorphous carbon was used but with a large central hole that omitted the low spatial frequency region (Danev and Nagayama, 2010).

Most of the initial applications used non-biological or negatively stained samples. There was no significant progress in that direction until 2001 when the development of the ZPP saw a revival. It was suggested that two sequentially collected images, one with conventional defocus TEM and the other one with phase plate TEM, could be numerically combined to reconstruct the complex form of the object wave since both amplitude and phase of the wave are present in the phase plate/non-phase plate images (Danev and Nagayama, 2001a). However, this approach is practically difficult since two images are acquired from the same position after inserting the phase plate and the objective aperture. Therefore, this proposal was followed shortly by an experimental investigation of the ZPP made of amorphous carbon film with a 1 µm central hole (Danev and Nagayama, 2001b). In that study phase plate and CTEM images of horse spleen ferritin were compared. To this date, amorphous carbon is the material of choice for thin film phase plates because of its favorable properties, such as easy to prepare, chemical inertness, electrical conductivity and mechanical strength (Danev and Nagayama, 2010).

After the proof of concept experiments in the early 2000s the ZPP was used in several publications with biological applications in both SPA and CET (Danev et al., 2010; Danev and Nagayama, 2008; Fukuda et al., 2009; Furuhata et al., 2008; Shimada et al., 2007; Tosaka et al., 2005; Yamaguchi et al., 2008; Yui et al., 2008). Apart from its strengths, the ZPP has some drawbacks, such as quality inconsistency after

fabrication, around 13% signal loss depending on the thickness of the carbon film (electrons are scattered by the film) and ageing (loss of performance with time). Aging was practically the most debilitating factor and was thought to be due to physical and chemical modification of the amorphous carbon film during exposure leading to reduced conductivity and beam induced electrostatic charging. Phase plates deteriorated in a matter of hours or a few days necessitating frequent exchanges (Danev et al., 2009; Danev and Nagayama, 2010).

The VPP was developed during an attempt to improve the performance of the ZPP. The VPP works based on the Volta potential which causes phase retardation of unscattered electron beam relative to the scattered ones. The VPP has to be heated to ~200 °C to prevent contamination on the film of the phase plate which would otherwise lead to poor CTF performance. The benefits of the VPP relative to the ZPP are longer life time, no fringing artifacts in the image and no need for precise alignment of the central hole, since it does not have a hole. Surface modification of the phase plate film by the incident electron beam combined with a chemical equilibrium between the film surface and residual gases in the vacuum are considered to be the main factors producing the phase shift with the VPP (Danev et al., 2014).

The following sections describe SPA and CET, the two main 3D structural analysis cryo-EM techniques.

1.2.5. Cryo-electron microscopy

Single particle analysis (SPA): Development of cryo-EM started in 1970s, following the development of other techniques for macromolecular structure determination. X-ray crystallography is one of the most prolific methods in structural biology and was used to solve most of the known structures today (Jazayeri et al., 2017; Manglik et al., 2015; Rasmussen et al., 2011; Rosenbaum et al., 2007; Song et al., 2017). However, it has its own limitations the main of which is the requirement for a crystallized specimen. SPA was developed as an alternative tool based on TEM. It uses random 2D projections of individual particles which when computationally combined can generate a 3D reconstruction of the target structure (Nogales and Scheres, 2015).

In 1968, De Rosier and Klug managed to get a 3D electron microscopy reconstruction of the helical assembly of a T4 bacteriophage tail (De Rosier and Klug, 1968). A few years later, Henderson and Unwin determined the structure of bacteriorhodopsin at 7 Å resolution using 2D electron crystallography (Henderson and Unwin, 1975). This effort was the first glimpse on a membrane protein structure solved by EM. In fact, a few more structures came along using electron crystallography but it was limited due to difficulties in producing well-ordered 2D crystals and obtaining a sufficient high resolution in electron

micrographs at high tilt angles. In the 1980s, the concept of SPA was introduced with the ability to get a structure from micrographs containing randomly oriented particles (Frank and van Heel, 1982; van Heel and Frank, 1981). Initially the samples were embedded in heavy metal salts (negative staining) in order to increase the contrast and make them compatible with the vacuum environment inside the TEM. However, negative staining limited the achievable resolution to about 2 nm (the staining salts grain size). The first attempt in observing hydrated samples was in 1972 by Matricardi et al. They showed that fully hydrated catalase crystals can diffract electrons to high resolution (Matricardi et al., 1972). In 1974, a similar experiment was performed by Taylor and Glaeser but using a frozen-hydrated catalase crystals with similar resolution (Taylor and Glaeser, 1974). In 1981, Dubochet and McDowall published a quick-freezing method capable of vitrifying pure water and thus set the base for cryo-EM (Dubochet and McDowall, 1981). For more than two decades the resolutions in single particle cryo-EM were at best around 1 nm. To help with the interpretation of the relatively low resolution maps, hybrid approaches were developed based on cross-linkers, mass spectrometry or docking high resolution structures from different techniques into the cryo-EM maps to build a pseudoatomic model (Lasker et al., 2012). In recent years, new technological and methodological advances, including more stable and automated electron microscopes, direct electron detectors, data processing software and phase plates transformed cryo-EM from a low resolution technique (a.k.a. “blobology”) into a rapidly expanding field capable of producing near atomic resolution maps and *de novo* atomic model building (Glaeser, 2016; Khoshouei et al., 2017a; Kuhlbrandt, 2014; Nogales, 2016).

Samples for SPA should be prepared in such a way that they can tolerate the high vacuum of the TEM and the exposure to electrons. To that end, the specimen is applied to a glow discharged TEM grid, which makes the carbon support hydrophilic, and then it is rapidly frozen by plunging in liquid ethane. This process is called “vitrification” because the freezing speed is high enough to preserve the disordered structure of water in the form of amorphous ice. There are various grid types, most commonly based on amorphous carbon film, with some new types designed to minimize beam-induced motion using doped silicon carbide or gold films (Russo and Passmore, 2016; Yoshioka et al., 2010). After vitrification, protein molecules are embedded in an amorphous ice layer, its thickness determines to a large extent the SPA performance. Thinner ice layers improve the contrast and minimize defocus variations and are therefore desirable for high resolution structure determination (Cheng et al., 2015). However, the layer cannot be thinner than the protein size/dimensions.

Other parameters follow to optimize the experiment, i.e. magnification and the corresponding pixel size which should be chosen carefully in order to achieve a good balance between the detector performance and the field of view. Higher magnifications (smaller pixel sizes) provide better SNR for high frequencies but reduce the image area and thus the number of particles per image (Penczek, 2010).

With modern direct electron detectors each micrograph contains a series of frames, i.e. a ”movie”. As a first step of the data processing the frames are aligned and then summed in order to negate the effects of beam-induced motion. There are several free software packages for frame alignment (Rubinstein and Brubaker, 2015; Scheres, 2014; Zheng et al., 2017). As part of the frame averaging process, it is common to use “dose weighting” filtering according to the accumulated dose for each frame. The initial frames contain high resolution information because the sample will be less damaged by the electron beam. As the exposure progresses high frequency information gradually disappears. Dose weighing uses a properly tuned low pass filter, which becomes more “aggressive” depending on the accumulated dose, to maximize the SNR for all spatial frequencies in the movie sum. After motion correction, image processing is done with one of the available software packages e.g. RELION (Scheres, 2012b), EMAN2 (Tang et al., 2007), SPHIRE (Moriya et al., 2017), SPIDER (Frank, 1981), FREALIGN (Grigorieff, 2007), SPARX (Hohn et al., 2007) and cryoSPARC (Punjani et al., 2017).

Particle picking is the next step in the SPA workflow. Traditionally it was done manually but nowadays this is replaced by either a semi-automated (manual training on a few micrographs) manner or with fully automated procedures. One of the most convenient and efficient particle picking software packages is GAUTOMATCH (Zhang, 2016a) which was used in most of the projects in the current thesis. GAUTOMATCH is GPU accelerated and picks particles based on provided templates or without a template (internally generated Gaussian template).

After particle picking CTF estimation is done using CTFFIND4 (Rohou and Grigorieff, 2015) or Gctf (Zhang, 2016b). CTF estimation is a very important step in the data analysis because errors in the measured defocus, astigmatism and phase shift will have a strong influence on the final resolution. In order to improve the accuracy of the CTF fits it is important to choose the fitting parameters such, that they are close or corresponding to the experimental values (Zhang, 2016b).

The first step in the reconstruction process is 2D classification. It classifies the particles in a number of 2D classes and allows removal of false positives, damaged particles, different oligomers etc. 2D classification provides the first look into the actual quality of a dataset. It also helps to diagnose problems such as

preferred orientation, heterogeneity and flexibility. Especially for projects dealing with an unknown structure, first 2D classes are used to generate an initial 3D model that serves as a reference in the upcoming 3D steps. Relion is the mainly used program which performs a 2D multi-reference maximum-likelihood classification. It starts with random subsets of particles as seeds for the classes and then goes through a specified number of alignment and maximization iterations (Scheres, 2010).

Following the 2D classification step is the 3D classification step. Particles are compared with projections of several 3D references at various angles and thus the Euler angles, in-plane rotations and XY translations for each particle can be determined (Frank, 2006; Sigworth et al., 2010). As said, Relion uses a maximum-likelihood approach which instead of selecting a single set of alignment parameters for each particle assigns probabilities to the full orientation space (Scheres, 2012a; Sigworth et al., 2010). Each particle is then used with the calculated probabilities as weights to reconstructs a set of new 3D volumes, which are then used as references for the next iteration. After a certain number of iterations (typically ~25) the structures and the particle sets of the 3D classes reach a steady state (convergence). In the case of a homogeneous, non-flexible structure the particles from the highest resolution class are used for the final 3D refinement step. If the sample contains several conformational states and/or oligomers, 3D classification can be done multiple times until homogeneous classes are obtained. The particles from each class are then subjected to a 3D refinement step in order to generate a 3D map for each state/oligomer.

3D refinement is the last step of the reconstruction. It is similar to 3D classification but uses a single 3D starting reference and the “gold standard” approach. This approach involves splitting the dataset into two random halves, which are processed completely independently from each other. After the refinement of each half has converged, the resolution of the reconstruction is assessed by a Fourier Shell Correlation (FSC) between the two, independent 3D half-maps. As a last step, the two half-maps are combined to produce the final reconstructed 3D map (Scheres, 2012b).

At the time of writing this thesis, statistics from Protein Data Bank in Europe (A public data bank for electron microscopy density map deposition using various techniques) show that the number of released maps is increasing annually. Among all deposited maps from various available techniques for structure determination most have been obtained by the single particle technique (~80%). (Figure 2).

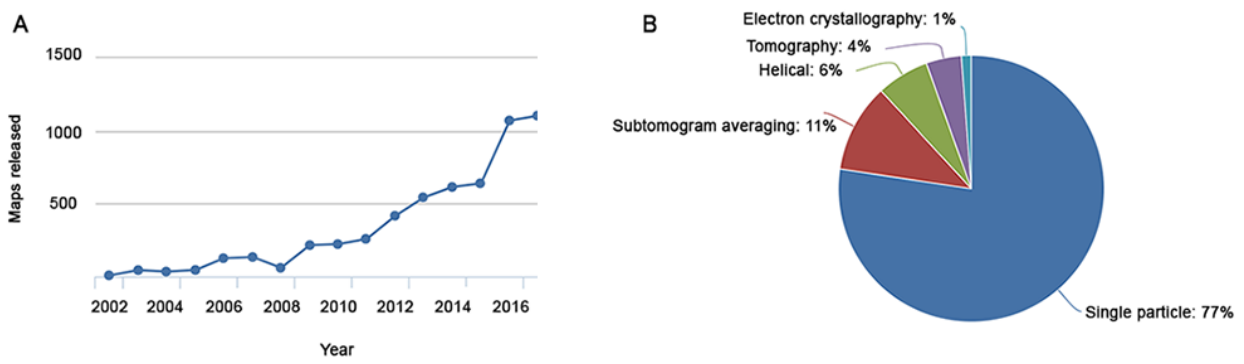

Figure 2: Electron microscopy data bank statistics from released maps. (A) Cumulative number of released maps from 2002 until the end of 2016. (B) Distribution of 5560 released maps versus different used techniques.

Figure 3 shows the resolution trends from 2002 until 2018. The average resolution of single particle analysis in 2017 is below 8 Å while the highest resolution is 2.3 Å (Figure 3A). The highest resolution (1.8 Å) was reported in 2016 from glutamate dehydrogenase with the molecular weight of 334 kDa (Merk et al., 2016). (Figure 3B).

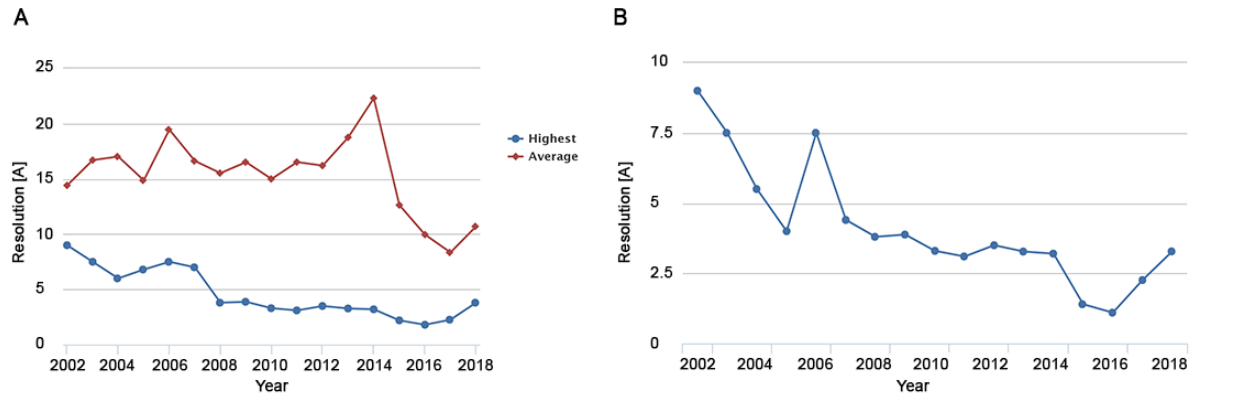

Figure 3: Resolution trends of single particle released maps from 2002 to 2017. (A) Average resolution and highest resolution in 2002 are 14.4 Å and 9 Å respectively. (B) Highest resolution achieved in a given year showing average resolution and highest resolution in 2016 are 10 Å and 1.8 Å respectively.

Single particle analysis has delivered high resolution structures of biological specimens with molecular weight of 100 kDa or larger. Given the fact that few structures of below 100 kDa are available at near atomic resolution, VPP could be an alternative tool which could deliver such structures in a time-efficient manner. Figure 4 shows that 2% of the available structures are from proteins with molecular weight of 100 kDa or below.

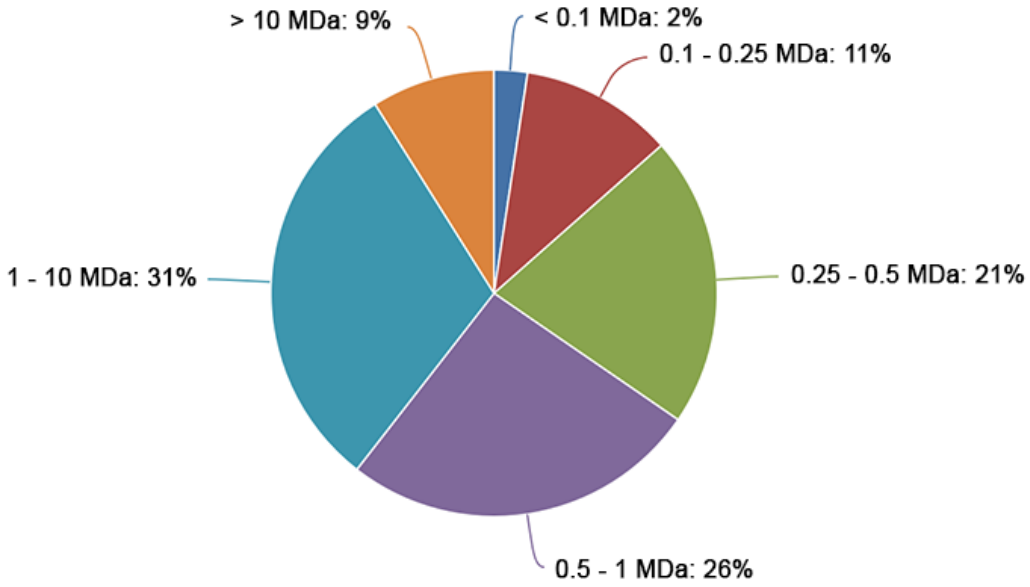

Figure 4: Molecular weight distribution of released single particle maps. Only a small fraction of released structure has a molecular weight of 100 kDa or below.

In 1995 (Henderson, 1995), it was predicted that in presence of ideal imaging conditions the size of the smallest particle one could observe and thus solve by SPA is inversely proportional to the contrast of the image to the power of 2 (C^2). Phase plates producing a higher image contrast, therefore could become a critical tool in solving especially small complexes.

First part of the results chapter shows applications of the VPP to SPA of challenging protein complexes with molecular weights between 17 and 257 kDa. All results have been published in peer-reviewed journals and this chapter is based on those publications.

Cryo-electron tomography: If the sample is not a purified protein but intact biological systems, such as cells or organelles, then electron tomography is the technique of choice. Electron tomography uses multiple projections of the same area at different tilt angles. The set of projections from the sample area is called tilt series. Usually the sample is tilted from -60° to +60° and in some cases from -70° to +70° but it is not possible to tilt the sample from -90° to +90° because of the specimen holder geometry. This limited tilt range is the reason for missing 3D information resulting in a missing wedge in Fourier space which leads to anisotropic resolutions of the reconstructions (lowest along the z-axis, i.e. perpendicular to the sample surface).

After the tilt series are acquired, reconstruction of the projections can be performed by different software packages (Kremer et al., 1996; Nickell et al., 2005). One of the most common, and oldest, algorithms for 3D tomographic reconstruction is weighted back-projection.

The attainable resolution in tomograms is limited due to two main factors: the low SNR because of the limited applied dose and the incomplete angular sampling. Theoretically, Crowther showed that the attainable resolution is the inverse of the angular increment (measured in radians) multiplied by the object diameter (for aspherical object), the so-called Crowther criterion (Crowther et al., 1970). In practice, the resolution of single reconstructions is much lower than that because of the limited dose. However, it is possible to increase the resolution by performing subtomogram averaging. If identical copies of a macromolecule or a complex are present in a tomogram(s), they can be extracted as subvolumes (subtomograms) and then aligned and averaged to increase the SNR and thus the Fourier space coverage. A part of this thesis is focused on achieving subnanometer resolution from phase contrast subtomogram averaging (Forster and Hegerl, 2007).

1.2.6. VPP Cryo-electron microscopy

Zernike phase plates were the most successful phase plate types in the early 2000s. They were used by several groups for real biological applications and already demonstrated the advantages. However, ZPP have significant practical limitations, such as a short lifespan, fringing artifacts around strongly scattering objects in the micrographs and moreover they were difficult to use and due to their limited lifetime inapplicable for automated data collection (Nagayama and Danev, 2008).

In 2011 a joint project between FEI and MPI was initiated with the goal to improve the performance of the ZPP and in particular its lifespan and usability. The main approach was to test different materials with the hope of finding a material which performed better than amorphous carbon. To test the performance of different materials, a beam-induced phase shift (BIPS) test was used. Numerous materials were tested, such as silicon nitride (SiN), silicon carbide (SiC), combination of Silicon and Platinum, coated carbon and doped carbon. None of the tested materials provided better overall performance than amorphous carbon. However, during those tests a phenomenon was discovered: the interaction of the focused central beam with the carbon film created a phase shift. This characteristic led to the development of the Volta phase plate (Danev et al., 2014; Danev and Nagayama, 2011; Fukuda et al., 2009).

The idea of using a continuous film as a phase plate is not new. In the 1970s Johnson and Parsons used a beam-created contamination spot on a carbon film as a phase plate (Johnson and Parsons, 1973). Later in

2012, Malac et al. used local positive charging of the film due to secondary electron emission for contrast enhancement. However, in this case electrostatic charging caused severe CTF distortion which prevented CTF fitting and correction (Johnson and Parsons, 1973; Malac et al., 2012).

In 2014, first VPP results were presented using a heated thin amorphous carbon film (12 nm film thickness), positioned at the back-focal plane of the objective lens. The heating of the film prevented the formation of beam-induced contamination. The observed phase shift was a result of a negative Volta potential. Volta potential is the difference between the inner potential and the surface potential. The phase shift between scattered and un-scattered electron beams was caused by the 3D electrostatic potential distribution in the vacuum above the Volta potential patch on the surface of the film and not by the inner potential of the film (Danev et al., 2014).

1.2.7. VPP application in single particle analysis

Peroxiredoxins (Prxs) are a ubiquitous class of thiol-dependent peroxidases which are responsible for detoxification of reactive oxygen species. Human Prx3 was the first non-test system which the structure was solved by VPP single particle analysis (Khoshouei et al., 2016). Prx3 is one of very few small complexes which have been solved to date by cryo-EM. (Bai et al., 2015b; Bartesaghi et al., 2015; Liao et al., 2013).

Prx3 has a molecular weight of 257 kDa and thus exhibits poor contrast in conventional defocus images. It is susceptible to beam-induced motion and has a tendency of preferred orientation in thin ice. These issues are major limiting factors in SPA and have been discussed previously (Cheng et al., 2015; Khoshouei et al., 2016).

G-protein-coupled receptors (GPCRs) are one of the largest families of cell-surface receptors. GPCRs could allosterically transmit extracellular signals to the inside of the cell. There are several classes of GPCRs, such as class A, B, C, D, E and F. One particular family of GPCRs, the class B GPCRs, is the major target for treatment of chronic diseases, such as osteoporosis, diabetes and obesity. Elucidating the structure of GPCRs is pivotal in understanding its functionality, which could be essential for harnessing its therapeutic potential (Congreve and Marshall, 2010). A class B GPCR was subjected to SPA with the VPP (Liang et al., 2017).

Despite various high-resolution structures of protein complexes solved by cryo-EM (Nogales and Scheres, 2015) and vast performance improvement provided by direct detecting cameras (Vinothkumar and Henderson, 2016), there are still limitations in the applicability of cryo-EM, one of which is the molecular weight of the protein (Khoshouei et al., 2017c). At the time of our VPP experimental attempt with hemoglobin, the smallest available structure from SPA was that of isocitrate dehydrogenase with a molecular weight of 93 kDa at 3.8 Å resolution (Merk et al., 2016). Back in 1995, the predicted lowest molecular weight of a complex which could be solved by single particle analysis was 38 kDa (Henderson, 1995). This estimation was based purely on theoretical considerations and was shortly thereafter followed by another estimation stating that the molecular weight threshold could be as low as 17 kDa (Glaeser, 1999). The difficulties in obtaining high resolution structures of small complexes arise from the poor signal-to-noise in low-dose cryo-EM images (Sigworth, 2016).

Here, the structure of tetrameric human haemoglobin (Hgb) with molecular weight of 64 kDa was determined using the VPP (Khoshouei et al., 2017c). Hgb was also chosen due to its iconic status as one

of the first structures determined using X-ray crystallography by Max Perutz in 1960, coincidently by solving the phase problem in crystallography (Perutz et al., 1960).

Organic molecule studies by X-ray crystallography began in 1930s. In 1953, Max Perutz showed that X-ray diffraction patterns from protein crystals could be phased by comparing the patterns from crystals of proteins with and without attached heavy atoms. In 1956, a true milestone was achieved in the history of structural molecular biology by John Kendrew and his colleagues who determined the structure of myoglobin at a resolution of 6Å (Kendrew et al., 1958). Kendrew chose myoglobin from sperm whale because of its low molecular weight, easy preparation and easy crystallization (Kendrew, 1962). The structure of myoglobin, the molecule which stores and releases oxygen in the muscles, was solved after overcoming the phase problem in crystal structure analysis. Obtaining such a structure had long been considered impossible in the field of X-ray crystallography. John Kendrew improved his original crystals which then revealed the complexity of the atomic structure of myoglobin at a resolution of 2Å (Kendrew et al., 1960). The structure featured 8 α-helices and atomic features, such as the binding site of a single oxygen molecule.

When Max Perutz solved the three-dimensional structure of haemoglobin in 1960s, it was rather astonishing that the tertiary structure of each of the four subunits resembled that of myoglobin. A chronicle of the events leading to the structure determination of haemoglobin and myoglobin was published by Strandberg, Dickerson and Rossmann in 2009 (Strandberg et al., 2009).

Up to date, over 120000 structures have been solved by x-ray crystallography, giving answers to a multitude of biological questions at the molecular level. X-ray crystallography was not the sole method capable of unravelling the structures of biological molecules at the atomic level, nuclear magnetic resonance (NMR) had a significant contribution as well (Wuthrich, 2001). In the current thesis imaging of myoglobin with molecular weight of 17 kDa was achieved using the VPP (Khoshouei et al., 2017a).

In recent years, new technological and methodological advances, including direct electron detectors, data processing software and phase plates transformed cryo-EM from a low-resolution technique (a.k.a. “blobology”) into a rapidly expanding field capable of producing near atomic resolution maps and *de novo* atomic model building. (Figure 5) (Glaeser, 2016; Khoshouei et al., 2017a; Kuhlbrandt, 2014; Nogales, 2016).

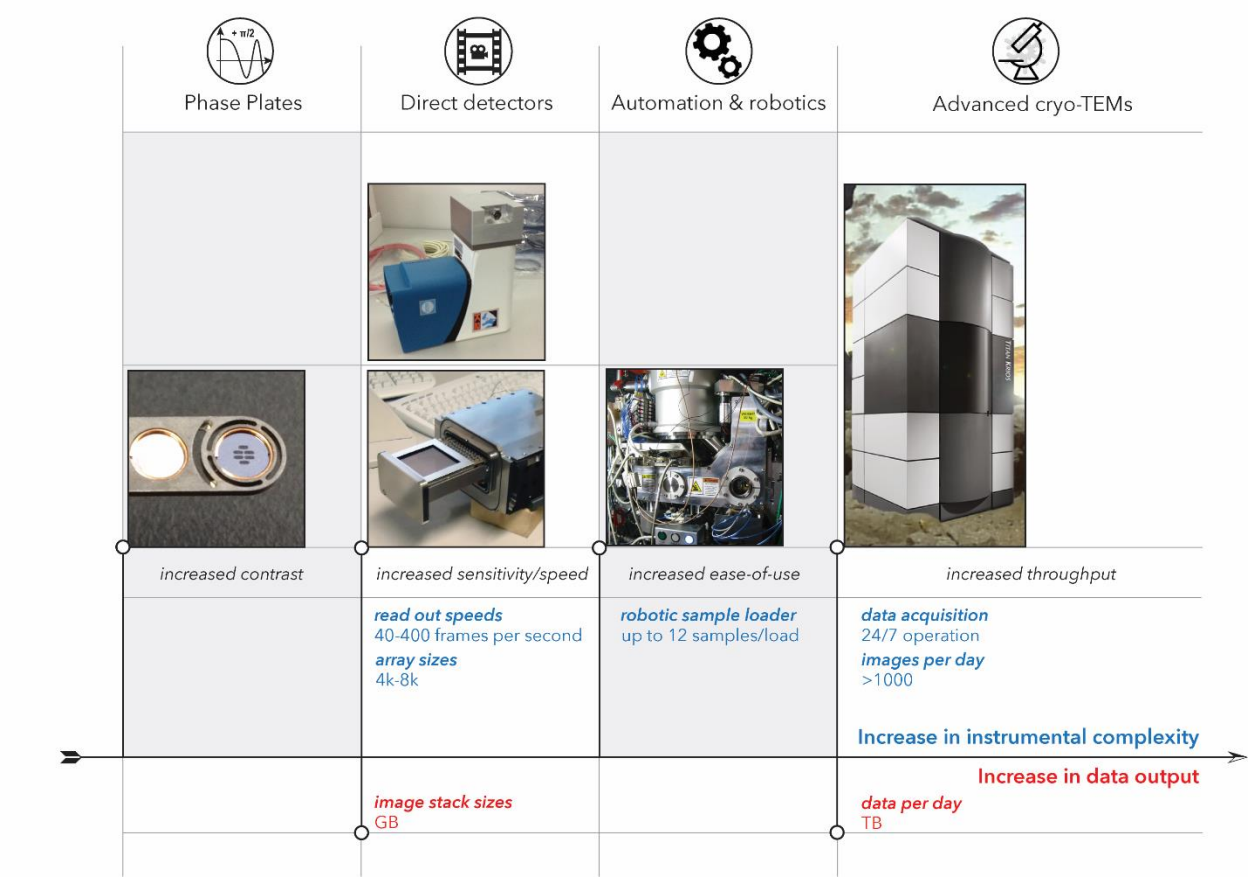

Figure 5: Technological advances in cryo-EM based on the development of detectors, phase plates, software and hardware automation for data acquisition. Figure was adopted from (Khoshouei et al., 2017a).

Nowadays cryo-EM allows structure determination of complexes which are accessible by X-ray crystallography or NMR (Danev et al., 2017; Khoshouei et al., 2017c; Khoshouei et al., 2016; Liang et al., 2017; Schweitzer et al., 2016). (Figure 6).

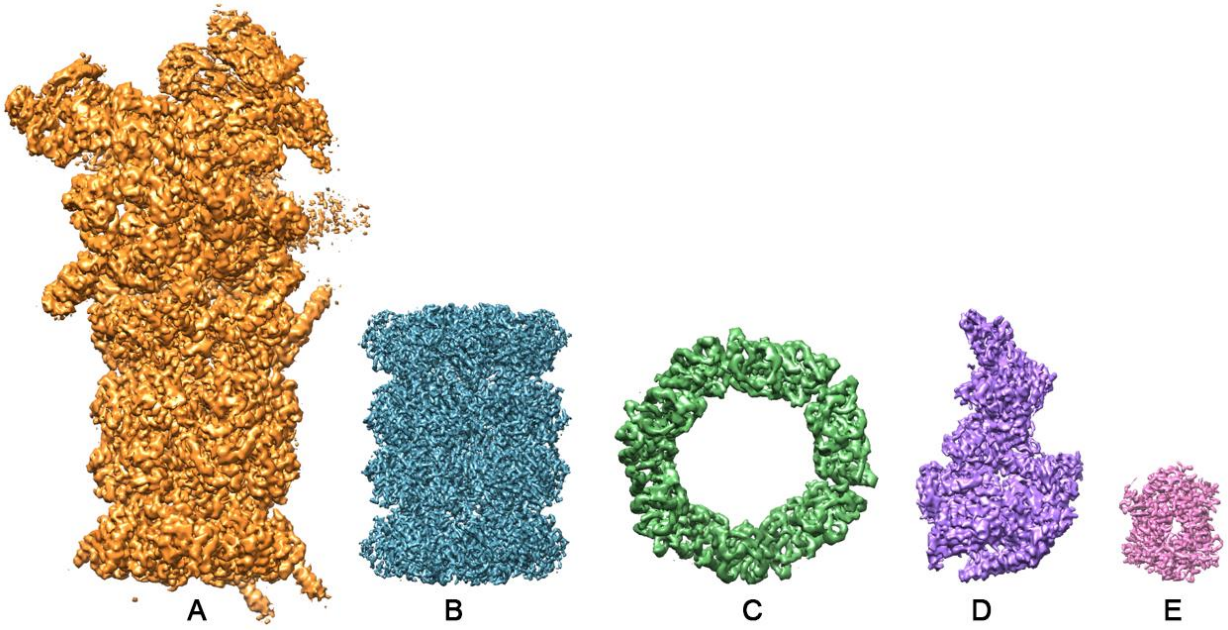

Figure 6: Examples of structures solved by single particle cryo-EM. (A) Single capped 26 S proteasome structure with molecular weight of 1.6 MDa using conventional cryo-EM. (B) VPP structure of 20S proteasome with molecular weight of 700 kDa. (C) VPP structure of human Prx3 with molecular weight of 257 kDa. (D) VPP structure of class B GPCR-G protein complex with molecular weight of 150 kDa. (E) VPP structure of human haemoglobin with molecular weight of 64 kDa. Figure was adopted from (Khoshouei et al., 2017a).

1.2.8. VPP application in cryo-electron tomography

In recent years, CET has shown its strength in providing three-dimensional views of the molecular organization within cells or isolated cellular organelles (Lučić et al., 2013). In that context, advanced image processing tools have become of great importance for extracting structural information from tomographic data (Briggs, 2013; Forster and Hegerl, 2007). In order to evaluate the VPP performance for CET in combination with subtomogram averaging, ribosomes were used. Their structure has been extensively studied at atomic resolution by techniques such as single particle cryo-EM and x-ray crystallography (Anger et al., 2013; Ben-Shem et al., 2010). Ribosomes have a molecular weight of 3-4 MDa and are involved in protein synthesis by converting transcribed messenger RNA into polypeptide chains (Steitz, 2008).

CET is based on collecting several tens of projections with low SNR. The final resolution of subtomogram averaging depends on how accurately macromolecules can be localized and then aligned (Scheres and Chen, 2012). These steps depend to a large extent on the low-frequency components of the signal and thus the contrast enhancement provided by the use of phase plates could be advantageous. (Khoshouei et al., 2017b).

Sperm cells are highly specialized and their shape and structure reflect the sole purpose of delivering genetic material and fertilizing the ovum. They consist of well-defined compartments segregated along the length of the cell (Jamieson, 1978). Each compartment serves a particular function, starting from the tip of the cell: the acrosome is responsible for recognition and fusion with the ovum and facilitates the DNA transfer; the nucleus contains the main cargo - highly condensed DNA which is dormant and does not undergo expression; the midpiece contains mitochondria which convert stored energy into ATP used for the propulsion of the cell, i.e. the flagellum, which is a mechanical motor pushing the cell forward. Detailed structural knowledge about each of the cell compartments can help to elucidate their mechanisms of action.

This study is focused on investigating the ultrastructure of earth worm (*Lumbricus terrestris*) sperm cells by CET augmented with the VPP (Danev et al., 2014). Previous structural studies of these cells have been performed using conventional sample preparation techniques, such as resin embedding and negative staining (Jamieson, 1978).These techniques while capable of providing overall structural information suffer from artefacts introduced by the specimen preparation process. CET of vitrified specimens provides structural information which represents as close as possible the physiological state of the system. However, CET is limited by radiation damage and overall low contrast which result in low SNR of the images. The VPP improves the contrast and consequently the SNR and enables artifact-free visualization of fine structural features (Asano et al., 2015; Bauerlein et al., 2017; Fukuda et al., 2017; Fukuda et al., 2015; Mahamid et al., 2016).

The ultrastructural and morphological information can be beneficial for taxonomic and phylogenetic studies. Furthermore, knowing the structural details of the cell plays a significant role in understanding the functionality of the sperm. Spermiogenesis of different types of earth worm sperm has been reported in previous works such as the overall shape of this cell and different compartments but diminutive attention has been invested to the mature earth worm sperm. The last studies of this system are based on tissue fixation and plastic embedded samples (Gatenby and Dalton, 1959; Shay, 1972). Changes in the specimen during chemical fixation, dehydration and staining prevent the preservation of fine ultrastructural details and hinder the interpretation of the images.

2. Materials and methods

2.1. Development of the Volta phase plate

2.1.1. Fabrication of the Volta phase plate

3 mm titanium TEM grids were cleaned with acetone in order to remove possible contaminants. Freshly cleaved mica was inserted in a BAL-TEC MED-020 (now Leica Microsystems) electron beam evaporator and the chamber was pumped until it reached a vacuum in the range of 10^{-5} or 10^{-6} mbar. The electron beam evaporator was set to 1.85 kV and 85 mA and carbon was deposited on the mica. The thickness of the deposited film was controlled by a Quartz crystal thickness monitor and was measured to be around 12 nm. After taking out the mica from the evaporator the film was transferred to 3 mm titanium TEM grids by floating off the carbon layer on distilled water surface followed by decreasing the water level. Grids were kept in a glass Petri dish for a day in order to dry completely (Danev et al., 2014).

2.1.2. Phase shift characterization

The initial experiments were performed on an FEI Tecnai F20 electron microscope equipped with an FEI Eagle 4K CCD camera. Beam-induced phase shift characterization was done by taking image series (e.g. 50 subsequently images and 2 sec exposure time per image with 100 nC total dose) after inserting the amorphous carbon film at the back focal plane of the objective lens. The film was continuously heated to 200 °C. The microscope was aligned in terms of beam tilt pivot point in X and Y direction, beam shift, rotation center and stigmatism. In order to reach 1 nA beam current, condenser aperture (50 µm), suitable spot size and extraction voltage of the field emission gun of FEI Tecnai F20 microscope were chosen. The Tecnai F20 is a two-condenser lens system where the second condenser lens is used to adjust the on-plane condition of the phase plate. In order to visualize the beam spot the phase plate was brought to an off-plane condition by subtracting 0.2% of the on-plane condition from the excitation value of the condenser lens (in this case from 45,2% on-plane to 45% off-plane condition). The magnification was set to 29Kx with a pixel size of 0.75 nm after one time binning. A defocus of -15 µm was applied to observe several Thon rings, necessary to fit the CTF (Danev et al., 2014). CTF fitting is done using any software which has implemented phase shift estimation such as CTFFIND4 (Rohou and Grigorieff, 2015) or Gctf (Zhang, 2016b).

2.2. High resolution structure of the protein complex Prx3

2.2.1. Sample preparation

Protein expression was done in *E. coli* Rosetta cells and lysed in 20 mM HEPES, 150 mM NaCl and 10 mM imidazole buffer at pH of 8 using a Microfluidics M110-P lab homogenizer. The soluble fraction was subjected to nickel immobilized metal affinity chromatography (Ni-IMAC) with 5-ml HisTrap FF column. Subsequently Gel filtration on a HiLoad 16/60 Superdex 200 column (GE Healthcare) was performed in order to remove imidazole from the protein solution using a buffer composed of 20 mM HEPES and 150 mM NaCl at pH 8.0. His-Tag was removed from the target protein by TEV protease treatment. Untagged Prx3 was separated from poly histidine peptide by reverse Ni-IMAC (Khoshouei et al., 2016).

2.2.2. Sample vitrification

Two datasets were taken which produced two structures with 7.3 Å and 4.4 Å resolution respectively. For the first dataset holey EM grids (Quantifoil, Groβlöbichau, Germany, 200 mesh copper R2/1) were glow discharged for 30 s in low pressure air in a Harrick plasma cleaner (Harrick, Ithaca, NY). FEI Vitrobot Mark III (FEI, Hillsboro, OR) chamber was set to 85% humidity, 4 sec blotting time and -1 mm blotting offset. 4 µl of sample was applied on an EM grid and plunged into ethane-propane mixture (37% ethane and 63% propane). After blotting off the excess of ethane propane mixture the grid was transferred to a cryo grid box and placed in a cryo dewar filled with liquid nitrogen. For the second dataset a different EM grid type (Quantifoil, Groβlöbichau, Germany, 200 mesh copper R1.2/1.3) was used but the plunging conditions were the same (Khoshouei et al., 2016).

2.2.3. Electron microscopy

For the first dataset, 44 movies were taken manually using a FEI Titan Krios operated at 300 kV and equipped with a Gatan GIF Quantum energy filter, a Gatan K2 Summit direct detector (Gatan, Pleasanton, CA) and an FEI VPP (FEI, Hillsboro, OR). Each movie comprises 10 frames with a total dose of 20 $e^-/Å^2$ at a corresponding magnification of 37000x (1.35 Å/pixel). EFTEM microprobe in counting mode with zero-loss imaging was used and the energy filter slit width was set to 20 eV (Khoshouei et al., 2016).

For the second dataset the same microscope was used as described for the first dataset. In this case 700 movies were taken with 15 frames at a magnification of 28700x and a pixel size of 1.74 Å/pixel. The second

dataset was taken automatically using SerialEM software (Khoshouei et al., 2016; Mastronarde, 2005). Both first and second data set were taken in focus. The second dataset was taken by positioning two focusing area on both sides of the acquisition area and by linear interpolation the correct focus was measured. In this case the target defocus was 20 nm.

2.2.4. Image processing

For the first dataset, 44 movies were subjected to motion correction using optical flow analysis which corrects the global and local movement of particles (Abrishami et al., 2015). One micrograph was used to pick the particles using e2boxer in EMAN2 (Tang et al., 2007). Coordinates of the picked particles were extracted using Relion 1.3 (Scheres, 2012a) with a box size of 152 pixels. 2D classification with 10 classes was done from 500 picked particles and three representative classes were chosen as side view, top view and tilted view to be used as templates for automatic picking in Relion. 30000 particles were picked automatically and were subjected to 2D classification to remove false positives. After 2D classification, 10000 particles were used in 3D classification with D6 symmetry imposed. At the end, 7000 particles from the best 3D classes were processed with 3D auto-refinement in Relion and the resolution was estimated using the gold standard Fourier shell correlation (FSC=0.143) criterion. Chimera software was used for 3D visualization and rigid-body docking (Goddard et al., 2007).

For the second dataset, the 700 movies were processed with the motion correction software (Li et al., 2013). 354000 particles were picked using EMAN2 (Tang et al., 2007) followed by particle extraction in Relion 1.3 with a box size of 152 pixels. CTF estimation was skipped since the dataset was acquired in focus. Three rounds of 2D classification were done to remove false positives which were followed by four rounds of 3D classification in Relion 1.3. At the end, 8580 particles from the best class were further processed with 3D auto-refinement in Relion. Particle polishing was done after refinement which was followed by post processing with an estimated -137 B-factor in Relion (Goddard et al., 2007).

2.3. High resolution structure of class B GPCR-G-protein complex

2.3.1. Sample preparation

CTR, human $G\alpha_s$ short, His6-tagged human Gβ1 and $G\gamma_2$ were expressed in HighFive insect cells (Thermo Fisher Scientific) using baculovirus. Cells were grown to a density of 4 million cells per ml and then infected with three separate baculovirus at a ratio of 1:2:2 for hCTR, $G\alpha_s$ and $G\beta_1\gamma_2$. Cultures were grown at 27 °C and harvested by centrifugation 45 hours post infection. Cells were suspended in 20 mM HEPES pH 7.4, 50 mM NaCl, 2 mM MgCl2 supplemented with protease inhibitors. Complex formation was initiated by addition of 1 μM salmon calcitonin, Nb35–His (10 μ g ml^{-1}) to stabilize the G protein heterotrimer and Apyrase (25 mU ml^{-1}, NEB) to remove excess nucleotides; the suspension was incubated for 1 hour at room temperature. Membranes were collected by centrifugation at 30,000 g for 30 min and solubilized by detergent 0.5% (w/v) lauryl maltose neopentyl glycol (LMNG, Anatrace) supplemented with 0.03% (w/v) cholesteryl hemisuccinate (CHS, Anatrace) for 2 hours at 4 °C. Insoluble material was removed by centrifugation at 30, 000 g for 30 min and the solubilized complex was immobilized onto M1 anti-Flag affinity resin. The resin was washed with 20 column volumes of wash buffer (20 mM HEPES pH 7.4, 100 mM NaCl, 2 mM MgCl2, 3 mM CaCl2, 100 nM sCT, 0.01% (w/v) MNG and 0.006% (w/v) CHS) before bound material was eluted. The complex was then subjected to size-exclusion chromatography to separate the complex from contaminants. Eluted fractions consisting of receptor and G-protein complex were pooled and concentrated. Final yield of purified complex was approximately 0.5 mg per liter of insect cell culture (Liang et al., 2017).

2.3.2. Sample vitrification

Holey EM grids (Quantifoil, Groβlöbichau, Germany, 300 mesh copper R1.2/1.3) were glow discharged before applying the sample. 5 μl of protein was applied on the grid in the chamber of FEI Vitrobot Mark IV (FEI, Hillsboro, OR) while the blot time and drain time were set to 3 secs and 0.5 sec respectively. The EM grid was plunged into liquid ethane cooled by liquid nitrogen (Liang et al., 2017).

2.3.3. Electron microscopy

2780 movies were taken using FEI Titan Krios operated at 300 kV equipped with a Gatan GIF Quantum energy filter, a Gatan K2 Summit direct detector (Gatan, Pleasanton, CA) and an FEI VPP (FEI, Hillsboro,

OR). Each movie comprises 50 frames with a total dose of 50 $e^-/Å^2$ with a corresponding magnification of 47,170x (1.06 Å/pixel). EFTEM nanoprobe in counting mode with zero-loss imaging was used and the energy filter slit width was set to 20 eV. Data acquisition was done in a fully automated way using SerialEM software and custom macros for single particle data acquisition with the VPP at 500 nm defocus (Liang et al., 2017; Mastronarde, 2005).

2.3.4. Image processing

2780 movies were subjected to MotionCor2 software to correct global and local movement of particles together with dose weighting of subframes (Zheng et al., 2017). Since the micrographs were taken with 0.5 µm defocus, CTF estimation was done using CTFFIND4 (Rohou and Grigorieff, 2015). 1213995 particles were picked and subjected to reference-free 2D classification with a binned pixel size of 2.12 Å to remove false positives. 426001 particles remained after removing false positives and were used with VIPER (Penczek et al., 1994) software to generate *ab initio* map as a reference for Relion 3D classification (Scheres, 2012b). The best class with 106838 particles with detailed features was chosen for focused refinement with a soft mask around the receptor and the G_s protein. The final map was post processed, which resulted in global nominal resolution of 4.1 Å and a nominal resolution of 3.8 Å in the receptor and G-protein regions. The resolution was estimated using gold standard Fourier shell correlation (FSC=0.143) criterion after modulation transfer function correction for the K2 summit direct detector. Local resolution map was created using ResMap implemented in Relion (Liang et al., 2017).

2.4. High resolution structure of human haemoglobin

2.4.1. Sample preparation

Human haemoglobin lyophilized powder was purchased from Sigma (Sigma-Aldrich, St Louis, MO, USA), product code H7379. The powder was dissolved in 50 mM Tris at pH 7.6 to get a concentration of 1.5 mg ml^{-1} (Khoshouei et al., 2017c).

2.4.2. Sample vitrification

Holey EM grids (Quantifoil, Groβlöbichau, Germany, 200 mesh copper R1.2/1.3) were washed using acetone and left in a glass petri dish to be dry. Thereafter, the grids were glow discharged for 30 sec.

4 µl of protein was applied on the grid in the chamber of FEI Vitrobot Mark III (FEI, Hillsboro, OR) with 5 sec blot time and -5 mm blotting offset. The chamber of the Vitrobot was set to 85% humidity and 5 °C temperature. The EM grid was plunged into liquid ethane-propane mixture (37% ethane and 63% propane) cooled by liquid nitrogen. The excess of ethane-propane was blotted away using a filter paper. The grids were stored in a cryo grid box for the imaging session (Khoshouei et al., 2017c).

2.4.3. Electron microscopy

For the first dataset, 223 movies were taken automatically using FEI Titan Krios operated at 300 kV equipped with a Gatan GIF Quantum energy filter, a Gatan K2 Summit direct detector (Gatan, Pleasanton, CA) and an FEI VPP (FEI, Hillsboro, OR). Each movie comprises 13 frames with a total dose of 23 $e^-/Å^2$ at a corresponding magnification of 37000x (1.35 Å/pixel). EFTEM microprobe in counting mode with zero-loss imaging was used and the energy filter slit width was set to 20 eV (Khoshouei et al., 2016).

The first dataset was taken in-focus in a fully automated way using SerialEM software and custom macros for single particle data acquisition with a precise focusing scheme which positions two focusing area on both sides of the acquisition area and the target defocus of 20 nm was measured by linear interpolation (Danev and Baumeister, 2016; Khoshouei et al., 2017c; Khoshouei et al., 2016; Mastronarde, 2005).

For the second dataset the same microscope was used as for the first dataset. In this case 2261 movies were taken at 0.5 µm defocus with 40 frames and a total dose of 40 $e^-/ Å^2$ at a calibrated magnification of 95,200x and a magnified pixel size of 0.525 Å. This pixel size was chosen to get better SNR in the high-

resolution region by placing it below the half-Nyquist frequency of the detector where the detective quantum efficiency is significantly higher. The second dataset was taken automatically using SerialEM software and custom macros for single particle data acquisition (Khoshouei et al., 2017c; Mastronarde, 2005).

2.4.4. Image processing

For the first dataset, 223 movies were subjected to motion correction software (Li et al., 2013). One micrograph was used to pick particles with e2boxer in EMAN2 (Tang et al., 2007). The picked particles were extracted using vlion which is a vectorized version of Relion 1.4 (Scheres, 2012b).

2D classification with 3 classes was performed on the picked particles and the classes were used as templates for automatic particle picking in Relion. 83959 particles were picked automatically and were subjected to two rounds of 2D classification to remove false positives. 47896 particles from the best 2d classes were subjected to 3d auto-refinement. Movie refinement was done afterwards followed by a particle polishing step. 47896 polished particles were refined and given as an input for 3D classification step with 6 classes. The best looking class was selected with 10272 particles as an input for 3D auto-refinement which resulted in 6 Å density map (Scheres, 2012b).

For the second attempt 2261 movies were subjected to motion correction software (Zheng et al., 2017). The output micrographs were binned one time, corresponding to a pixel size of 1.05 Å after binning, and the CTF estimation was done on non-dose weighted micrographs using CTFFIND4 (Rohou and Grigorieff, 2015) implemented in Relion 2.0.

The parameters used for CTF estimation of the second dataset are as indicated in the following table:

Table 2.4.4.1: Parameters used for CTF estimation in CTFFIND4.

Spherical aberration (mm)	2.6
Voltage (kV)	300
Amplitude contrast	0.07
Magnified pixel size (Angstrom)	1.05
Amount of astigmatism (A)	500
FFT box size (pix)	512
Minimum resolution (A)	20
Maximum resolution (A)	3
Minimum defocus value (A)	3000
Maximum defocus value (A)	7000
Defocus step size (A)	500
Estimate phase shifts	Yes
Phase sift - Min, Max, Step (deg)	0-180-10

After CTF estimation 707 micrographs which had estimated resolutions of worse than 4 Å were excluded from further processing. Gautomatch software (Zhang, 2016a) was used to pick the particles. 283600 extracted particles with a box size of 100 pixels were subjected to 2D classification in Relion2 (Scheres, 2012b). The best 2D classes were used to build an initial model in EMAN2 by the common-line approach (Tang et al., 2007). Two rounds of 3D classification were performed and the best class was chosen after each round. 175374 particles went to 3D auto-refinement in Relion with imposed C2 symmetry and a separate round of 3D auto-refinement without imposing any symmetry. The unfiltered maps from each 3D auto-refinement were sharpened which produced maps with 3.2 Å resolution (imposed C2 symmetry) and 3.4 Å resolution (no imposed symmetry). In addition, a subset of 76150 particles was selected after an additional round of 3D classification with 5 classes and no image alignment as an input for 3D auto-refinement without imposing symmetry which resulted in a 3.6 Å resolution map. The B-factors for the full dataset with imposed C2 symmetry, no imposed symmetry and a subset of particles with no imposed symmetry were -176 $Å^2$, -179 $Å^2$ and -157 $Å^2$ respectively (Khoshouei et al., 2017c).

For the modeling of the final map flexible fitting of the available crystal structure was done using nanoscale molecular dynamics (NAMD) implemented in MDFF (Chan et al., 2012) software. COOT (Emsley et al., 2010) and PHENIX (Adams et al., 2010) were used for rebuilding and real-space refinement which was followed by final refinement in REFMAC (Murshudov et al., 2011) with half-map cross validation (Brown et al., 2015).

The following table shows the data refinement parameters and model statistics (Khoshouei et al., 2017c):

Table 2.4.4.2*: Data refinement parameters and model statistics*

R.m.s. deviations	
Bonds (Å)	0.01
Angles (°)	1.53
Validation	
Clashcore, all atoms	3.53
Good outliers (%)	0.0
Ramachandran plot	
Favoured (%)	95.23
Allowed (%)	4.77
Outliers (%)	0.0

2.5. Revisiting the structure of myoglobin

2.5.1. Sample preparation

Myoglobin lyophilized powder from equine skeletal muscle was purchased from Sigma (Sigma-Aldrich, St Louis, MO, USA) with product code M5696. The powder was dissolved in 50 mM Tris at pH 7.6 to get a concentration of 60 mg ml^{-1} (Khoshouei et al., 2017a).

2.5.2. Sample vitrification

For myoglobin, TEM grids (Quantifoil, Großlöbichau, Germany, 200 mesh copper R1.2/1.3) were glow discharged for 30 sec in low pressure air using Harrick plasma cleaner (Harrick, Ithaca, NY). 4 µl of sample at 60 mg ml^{-1} was applied on the grid in the Vitrobot chamber (FEI Vitrobot Mark IV, Hillsboro, OR). The Vitrobot chamber was set to 100% humidity at 4 °C temperature. The sample was blotted for 5 sec with blot force of 20 and then plunged into liquid propane-ethane mixture (37% ethane and 63% propane) (Khoshouei et al., 2017a).

2.5.3. Electron microscopy

1916 movies were taken automatically using FEI Titan Krios operated at 300 kV equipped with a Gatan GIF Quantum energy filter, a Gatan K2 Summit direct detector (Gatan, Pleasanton, CA) and an FEI VPP (FEI, Hillsboro, OR). Each movie comprises 50 frames with a total dose of 50 $e^-/Å^2$ at a corresponding magnification of 95,200x (0.525 Å/pixel). EFTEM nanoprobe in counting mode with zero-loss imaging was used and the energy filter slit width was set to 20 eV. The dataset was taken automatically using SerialEM software and custom macros for single particle data acquisition at 0.5 µm defocus (Khoshouei et al., 2017a; Mastronarde, 2005).

2.5.4. Image processing

1961 movies were recorded and subjected to motion correction software (Zheng et al., 2017). The output micrographs were binned one time and the CTF estimation was done on non-dose weighted micrographs with Gctf (Zhang, 2016b). After CTF estimation 1114 micrographs which had estimated resolutions of better than 7.5 Å were kept for further processing. The fact that 847 micrographs were excluded from

further processing was not surprising since those micrographs have low number of particles therefore the SNR was not sufficient for reliable CTF estimation. Gautomatch software (Zhang, 2016a) was used to pick the particles. 140540 extracted particles with a box size of 64 pixels were subjected to 2D classification in Relion2 (Scheres, 2012b). Around 40000 particles were selected from the best classes for further processing. At the time of writing of the manuscript the amount of data was not sufficient to get a high resolution 3D reconstruction of myoglobin (Khoshouei et al., 2017a).

2.6. Whole cell phase contrast cryo-electron tomography

2.6.1. Sample preparation

The earth worm *Lumbricus terrestris* was obtained from a compost worm farm and was kept in special earth until two days before the experiment. After removing the worms from the soil, they were kept floating in tap water in a refrigerator for two days. The seminal receptacle bags were extracted from the worms while keeping them on ice from the beginning until the end of the dissection. After extraction, the seminal receptacles were transferred into 50 µl of modified earthworm ringer solution (D'Haese and Hinssen, 1987; Drewes and Pax, 1974; Krüger et al., 2008). The modified buffer contains 80mM L-Glutamic acid, 1mM KCl, 5mM TRIS, 0.1 mM CaCl2 with pH 7 adjusted by adding NaOH. The sperm was diluted 50 times in the buffer. Thereafter, the sample was checked under an optical microscope (Axiovert 200M equipped with a NeoFluar 40x objective from Carl Zeiss Microscopy GmbH, Jena, Germany) to confirm the motility and concentration of the sperm cells.

2.6.2. Sample vitrification

Holey EM grids (Quantifoil, Groβlöbichau, Germany, 200 mesh copper R 3.5/1) were treated with a glow discharge for 30 seconds. As fiducial markers for the tilt-series alignment, 10 nm gold nanoparticles were centrifuged with 20817 g relative centrifugal force (14000 rpm) for 20 min and concentrated 3 times. After applying 2 µl of the gold nanoparticle suspension and 4 µl of the sample on a glow discharged Quantifoil grid, the grid was plunge-frozen using a Vitrobot Mark III or IV (FEI Company, Eindhoven, NL). The optimal vitrification conditions for the Vitrobot Mark IV were: blotting time 11 sec, blotting force 10 at 100% humidity. The optimal vitrification conditions for the Vitrobot Mark III were: blotting time 5 sec, blot offset -3 mm at 85% humidity. The samples were vitrified in a propane-ethane cryogen mixture and then transferred and stored in liquid nitrogen.

2.6.3. Electron microscopy

Batch tomography with the VPP

Batch tomography was performed on a 300 kV Titan Krios (FEI Company, Eindhoven, NL) equipped with a 3838 x 3710 pixels, K2 Summit (Gatan Inc., Pleasanton, USA) direct detector camera, a Gatan Quantum post-column energy filter and an FEI VPP. Fifteen single-axis tilt series from a single sperm cell were

acquired at a magnification of 7,000x (7.1 Å/pixel) with an angular range of 100° (-50° to +50°) and a tilt-angle increment of 2° using SerialEM (Mastronarde, 2005). The total electron dose per tomogram did not exceed 25 e^-/A^2 so that overlapping regions could be imaged three times without noticeable radiation damage.

Dual-axis CET with the VPP

Dual-axis tilt-series were acquired on the same Titan Krios microscope as used for the batch acquisition. They were recorded in low-dose mode with a total dose of 70 $e^-/Å^2$, a tilt range of -60° to +50°, 2° angular increment and a defocus of 500 nm. The data was collected using Serial EM (Mastronarde, 2005) at a magnification of 9400x with a corresponding pixel size of 0.531 nm.

Single-axis CET with the VPP

Single-axis CET with the VPP was performed for the different compartments of the sperm cell. The data acquisition was performed using the same microscope and software as described in the above. The data was taken in low dose mode at a magnification of 9400x and 11800x corresponding to a pixel size of 0.531 and 0.421 nm respectively.

The tomogram of the FIB-milled wedge (in section 3.2.5) was recorded in low-dose mode at a magnification of 9400x and a pixel size of 0.531 nm. The total dose was 75 $e^-/Å^2$, tilt range of -45° to +61°, 2° angular increment and a defocus of 500 nm.

Focused ion beam scanning electron microscopy of worm sperm

A dual beam (FIB/SEM) instrument (FEI Quanta 3D FEG) equipped with a Quorum cryo-stage PP3000T (Quorum Technologies Ltd, Laughton, UK) was used to produce thin specimen wedges (Rigort et al., 2010; Rigort et al., 2012). After clipping the plunge-frozen sample in an autogrid and mounting into a shuttle, the specimen was transferred to the Quorum cryo-stage. Wedges were made by using a gallium ion beam with an acceleration voltage of 30 keV and a shallow milling angle of 7 °. An ion beam current of 0.5 nA was used to start the milling which was followed by lower currents of 0.3 nA, 0.1 nA and 50 pA steps. At the end, a final polishing (cleaning cross section method) was performed with a beam current of 30 pA (Schaffer et al., 2017). SEM observation of the milled wedges was performed with electron beam energy of 5 kV and a beam current of 12 pA. Finally, the grids with the milled wedges were stored in liquid nitrogen until TEM observation.

2.6.4. Image processing

Batch tomography reconstruction of VPP dataset

The micrographs of each series were aligned by tracking the gold fiducials. 3D reconstructions were calculated by weighted back-projection with the TOM software package (Nickell et al., 2005). The corresponding individual tomograms were reconstructed with a voxel size of $(2.84\ nm)^3$. A software routine was developed in Matlab [The MathWorks, Natick, USA] for stitching all tomograms to create a composed 3D reconstruction of the full cell body. Briefly, a visually identified 3D point, close to a distinguishable sample feature imaged in both tomograms of a neighboring pair, was used to select sub-volumes in the overlapping regions. These coordinates were also used for a coarse alignment of sub-tomograms down-sampled to $(11.36\ nm)^3$/voxel. The translational alignment was refined by cross-correlation between masked areas in the overlapping sub-tomograms. Rotational misalignment was negligible. Finally, the relative shifts between sub-tomogram pairs were used to paste all tomograms in the same volume, averaging the densities of overlapping areas. Due to the large number of tomograms and the large size of the original images (3838 x3710 pixels), the tomograms were further down sampled to a final voxel size of $(22.72\ nm)^3$ to obtain a volume of a manageable size (1273x227x236 pixels).

Dual-axis CET reconstruction of the VPP

Two tilt series of the same sample area were recorded with two orthogonal tilt axes. Each tomogram has half of the total dose required for a single axis CET. Each tomogram is reconstructed independently and then the two tomograms are aligned to each other. In the last step the 3D Fourier transforms of the two tomograms are combined to obtain one single reconstructed volume (Mastronarde, 1997; Tong et al., 2006).

Single-axis CET reconstruction of the VPP

2D projections of each series were aligned by tracking the ice-embedded gold markers. 3D reconstructions were performed by weighted back-projection in IMOD (Kremer et al., 1996) or the TOM software package (Nickell et al., 2005).

2.7. VPP subtomogram averaging at sub-nm resolution

2.7.1. Sample preparation

Ribosomes were prepared from rabbit reticulocyte lysate (RRL) purchased from Promega (Wisconsin, USA), as follows: 200 µl of RRL were subjected to ultracentrifugation using a TLA 100 rotor for 30 min at 150,000 g and 4 °C. The supernatant was discarded and the resulting ribosome pellet was resuspended in 100 µl of ribosome buffer (20 mM Hepes, pH 7.6; 50 mM KCl; 2 mM MgCl2) and directly used for EM grid preparation.

2.7.2. Sample vitrification

After glow discharging of the TEM grids (Quantifoil, Großlöbichau, Germany, 200 mesh copper R 2/1) for 20 secs, 3 µl of ribosomes with 3 µl of 10-nm colloidal gold particles were added to the grid in the Vitrobot chamber (FEI Vitrobot Mark IV, Hillsboro, OR). The chamber was set to ambient temperature of 22 °C and 60% humidity. The sample was blotted for 3 sec with blot force of 0 and then plunged into liquid ethane (Khoshouei et al., 2017b).

2.7.3. Electron microscopy

Tilt series were taken automatically using a FEI Titan Krios operated at 300 kV equipped with a Gatan GIF Quantum energy filter, a Gatan K2 Summit direct detector (Gatan, Pleasanton, CA) and an FEI VPP. Each movie contained 4-7 frames. Due to slight variations in the FEG emission the exposure time varied between 0.8 sec and 1.4 sec to keep the cumulative total electron dose constant. All tilt series were taken with a pixel size of 2.62 Å. EFTEM microprobe in counting mode with zero-loss imaging was used and the energy filter slit width was set to 20 eV. The data were taken automatically using SerialEM with the standard autofocusing procedure (Mastronarde, 2005). The nominal defocus for the CTEM dataset was -2.4 µm to -3.7 µm while for the VPP dataset it was 0 to -200 nm. In order to evaluate which parameters are the most critical ones for VPP data acquisition, 14 tomograms were taken with different focusing parameters. Out of those 14, only four tomograms showed the best preservation of high-resolution information (Khoshouei et al., 2017b).

Single axis tilt series were taken starting from 20° tilt to -60° tilt and the second half starting from 22° tilt to +60° tilt with an angular increment of 2° and the total dose of 90 - 100 $e^-/Å^2$. For the VPP datasets, the

phase plate was conditioned before starting the tilt series acquisition in order to have sufficient contrast. VPP conditioning was done with a total dose of 12 nC (0.2 nA beam for 60 sec) to generate an initial phase shift of 0.35 π (Danev et al., 2014). Each tilt series acquisition additionally irradiated the VPP with 30 nC (61 images x 2.5 s exposure x 0.2 nA beam current) and together with the 12 nC for the conditioning resulted in a 0.55 π phase shift. Therefore the VPP spot was changed after each tilt series (Khoshouei et al., 2017b).

2.7.4. Image processing

The projections from each tilt series were subjected to motion correction software (Li et al., 2013). After motion correction, CTF estimation and demodulation was done on each projection from the CTEM dataset using a tilt dependent and a local correction of the phase reversal scheme implemented in MATLAB scripts and PyTom (Eibauer et al., 2012; Hrabe et al., 2012). No CTF estimation was done on the VPP dataset since it was taken in-focus and no Thon rings were visible. Template matching was done to pick each subtomogram containing one ribosome according to Gaussian distributed constrained correlation (Khoshouei et al., 2017b).

Each subtomogram was binned one time corresponding to a pixel size of 0.524 nm with a box size of 80^3 voxels and reconstructed from the weighted aligned projections from -60° to +60° tilt. After iterative alignment and averaging of subtomograms, the reconstruction was done on unbinned subtomograms and reduced tilt range (from -20° to +20°) in order to eliminate parts of the tilt series where the sample was damaged. At the end, 30 $e^-/Å^2$ of the total dose contributed in the final reconstruction. Alignment of subtomograms were done iteratively until convergence using PyTom with a reference derived from a high resolution structure of the human ribosome (EMD-5592 (Anger et al., 2013)) by low-pass filtering to 2 nm resolution. After each iteration the average from the previous iteration was used as a reference for the subsequent iteration. For the analysis in section 3.2.6 where the particle number versus resolution is discussed, every subset of subtomograms were averaged using alignment shifts and rotations from the full set of subtomograms containing 1400 ribosomes or the subtomograms were averaged using the alignment shifts and rotations among the reduced subset. Fourier-shell cross resolution with 0.33 criterion was used to assess the resolution against EMD-5592 and the final map was sharpened using an empirically determined B-factor of -500 $Å^2$. For the mean standard deviation curve shown in section 3.2.6, 100 ribosomes from CTEM and VPP dataset were extracted using a pixel size of 1.05 nm and 40^3 voxels to measure their mean standard deviation for all available spatial frequencies (Khoshouei et al., 2017b).

3. Results and discussion

3.1. Development of the thin film phase plate

3.1.1. TEM requirements for the phase plate

Phase plate installation requires some modifications of TEM. One of the requirements is to have an objective aperture holder installed on the back focal plane of the microscope (Figure 7). In some microscopes the objective lens aperture is not located on the back focal plane in order to have short focal length for high resolution imaging therefore they need more modifications for phase plate installation. As it was mentioned in equation 12, the size of the phase plate in Fourier space is inversely proportional to the focal length of the objective lens therefore microscopes equipped with the phase plate have longer focal length and subsequently larger diffraction pattern. The latter fact allows less difficulties in manufacturing of the phase plate (Danev and Nagayama, 2010).

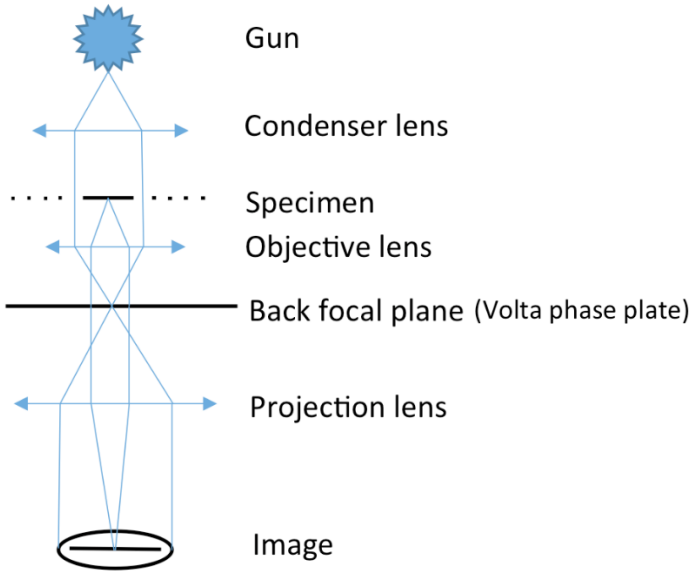

Figure 7: Schmatic diagram of TEM equipped with the VPP. The VPP is inserted at the back focal plane of the objective lens.Figure was adopted from (Khoshouei et al., 2016).

3.1.2. Design of the Volta phase plate

The usual objective aperture holder was replaced with a new ceramic phase plate holder as it is shown in Figure 8. This ceramic holder has a built-in heater which has the capability of heating phase plate up to 225 °C. Two objective apertures and one heated phase plate can be accommodated on the same holder. As it is shown in the left panel of Figure 8, 6 ellipsoid phase plates are located on the tip of the holder where each has 76 positions to be used for data acquisition (Danev et al., 2014). In order to navigate to a specific position on the phase plate there is a built-in section in the GUI of the microscope provided by FEI.

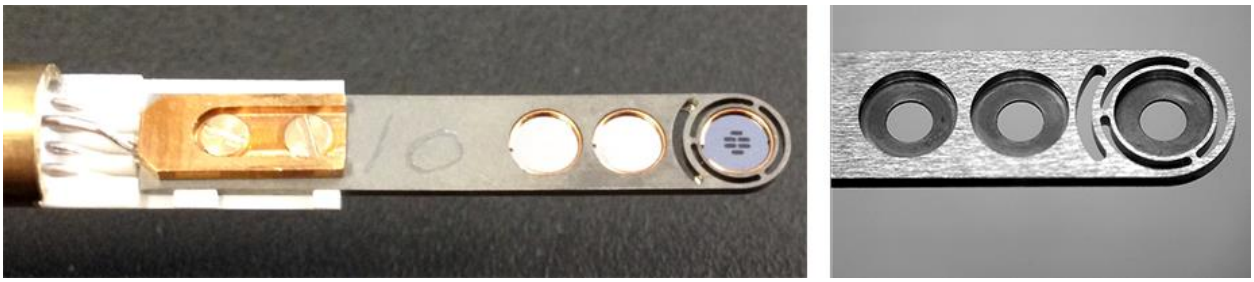

Figure 8: Newly designed ceramic phase plate holder. The tip of the holder was coated by platinum and a built-in platinum heater to prevent electrostatic charging effect. 6 VPP are located in the phase plate slot. The phase plate slot indicated in the left and right panel is located at the tip of the holder. The tip of the phase plate is thermally isolated by a pattern of few cutoffs. Two objective apertures are shown in the non-heated slots of the holder. Figure was adopted from (Danev et al., 2014).

Since the VPP is prepared in a primitive way as it was mentioned in section 2.1.1, the film becomes crinkled after transferring to a 3 mm TEM grid. Figure 9A shows the VPP after fabrication and Figure 9B and Figure 9C show the VPP after being used about 3 years where there are deposited spots which from the specimen while unloading or some deposited residuals from the vacuum of the microscope on the VPP.

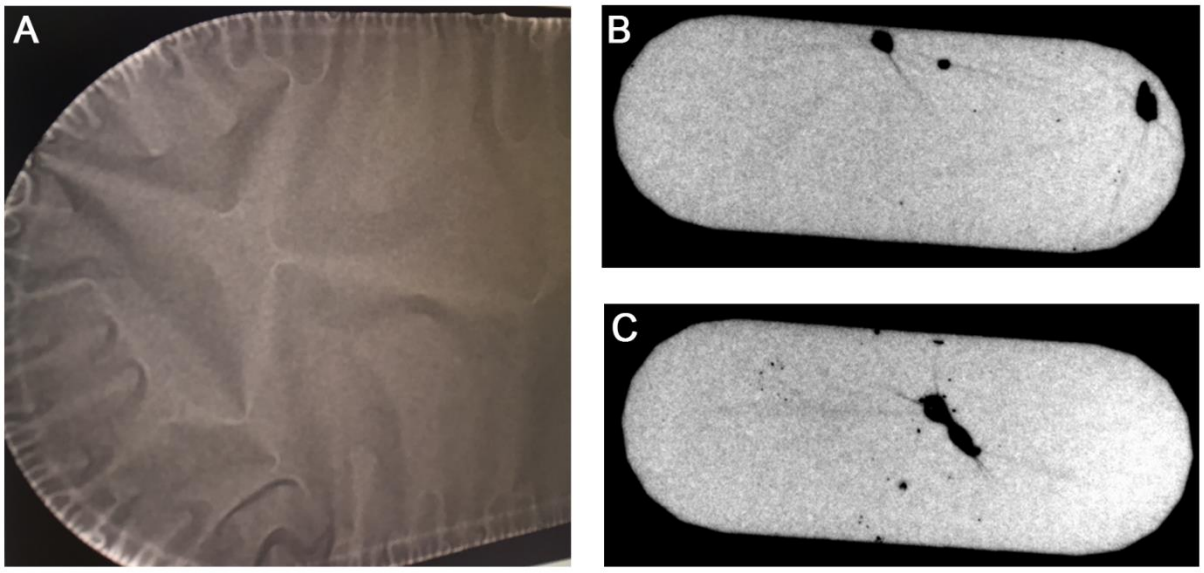

Figure 9: A photograph of the VPP before and after usage. (A) Zoomed-in image of the VPP after installation in the TEM. (B) Visibility of some contaminations after a period of time using the VPP.

The name of the VPP originates from the fact that the phase shift creation comes from the local modification of the Volta potential above the surface of the carbon film. This hypothesis is based on local changes in the carbon film properties after being radiated by the central diffraction beam which leads to changes in the inner potential (the potential experienced by a charged particle moving from an infinity distant to a point inside the material) and the surface potential (the potential experienced by a charged particle moving from a point inside the material to a point very close to the surface of the material) (Danev et al., 2014).

Figure 10 shows the schematic of different potentials where V_1, V_s and V_v are inner potential, surface potential and Volta potential respectively. Beam irradiation may cause local desorption of residual species in the vacuum of the microscope which modifies the work function of the carbon film locally and create the Volta potential. The negative sign of the Volta potential shows the Volta potential of the irradiated area is lower than the surroundings. Numerical simulation of the 3D potential distribution above a 1 µm –diameter grounded conductor with a constant potential (-1V) patch on the surface is shown in Figure 10B. As a result an electron traveling along the z potential profile experiences a phase shift which is proportional to the path integrated potential shown in Figure 10C. Due to highly localized phase shift in Figure 10C the area outside the central potential patch won't be affected and cause no deformation of CTF. Phase shift is linearly proportional to the patch size therefore having a narrow patch size means less phase shift compared to having a wide phase shift (Danev et al., 2014).

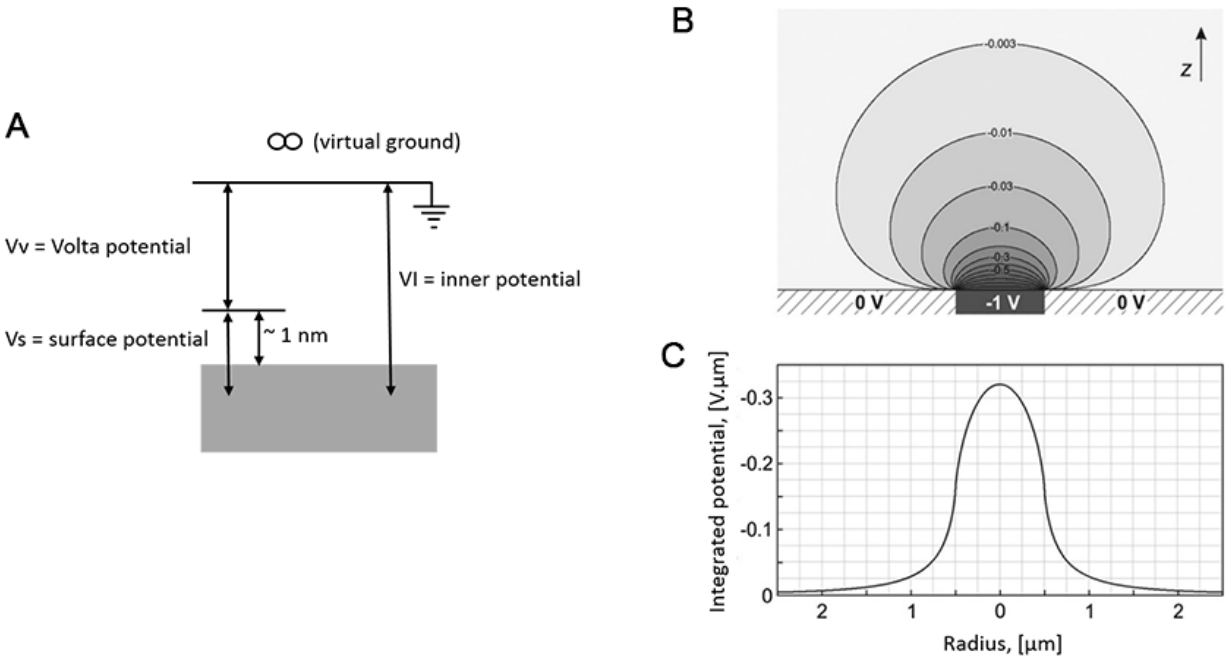

Figure 10: Schematic of different potentials associated with a conducting material in the vaccum and numeric simulation of the electrostatic potential distribution in the vacuum. (A) The Volta potential is the difference between the inner potential V_I (A potential that a charged particle would experience if brought to an infinity distant point) and the surface potential V_s (A potential that a charged particle would experience if moved from a point very close to the surface of the material to a point inside the material). (B) A cross-section through the center of the 3D potential distribution. (C) Integration of the distribution in A along the z axis to calculate the projected potential. Figure was adopted from (Danev et al., 2014).

Proper VPP operation requires “on-plane” condition. Setting the VPP operation in an on-plane condition allows the position of the central beam crossover at the back focal plane where the phase plate is located. Figure 11 shows the schematic of the on-plane and off-plane condition. Microscopes which are suitably designed such as Titan Krios, the on-plane condition corresponds to parallel illumination on the specimen.

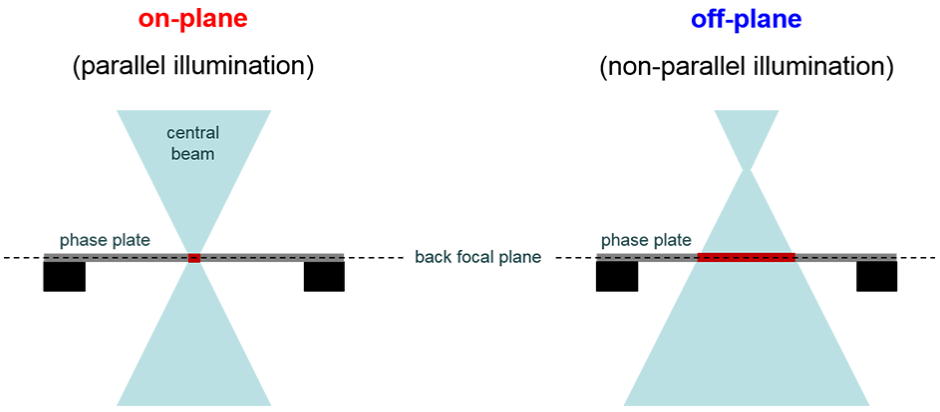

Figure 11: Schematic of on-plane and off-plane condition. Proper VPP operation is the on-plane condition which corresponds to parallel illumination on the specimen. VPP operation in the off-plane condition causes non-parallel illumination on the specimen and a larger area on the VPP is irradiated by the electron beam compared to the on-plane condition (red area).

To set the on-plane condition, Ronchigram observation is used to zoom into the film of the phase plate until no pattern of the film is observed. When the VPP is in the off-plane condition, some pattern of the carbon film is still visible and larger area on the phase plate is irradiated as shown in Figure 11.

To test the performance of different materials for the VPP, a beam-induced phase shift (BIPS) approached was used. This approach measures the phase shift development of the film after being experienced by the central diffraction beam. The resulting curve which is the phase shift vs. total dose on the film shows the stability of the film to electron beam quantitatively (Figure 12). After few days that the VPP was installed in the microscope, the central beam has a phase advance relative to the scattered beams. Moreover, BIPS curves indicate a slight positive charge (negative phase shift) on the first day after installation of the VPP into the microscope (Figure 12A, black squares).

The initial state of the carbon film directly after insertion is different from its state after some time in the vacuum (i.e. equilibrium state). The heated carbon film needs around one week to equilibrate. This transition is mainly due to chemical composition changes on the carbon film surface. Heating of the carbon film is necessary for the proper operation of the VPP since it prevents beam-induced contamination and charging effect. In charging effect, the CTF maxima move outward overtime showing that the central beam experiences phase retardation relative to the scattered beams. This retardation comes from positive charging effect at the position of the beam. However, in the case of no heated carbon film overall contrast increases but the CTF is deformed and cannot be corrected in data processing part. Practical experience with the VPP showed that the time required for reaching the equilibrium state differs for different microscopes indicating that it depends on the different vacuum conditions. With an increase in temperature the beam induced phase shift decreases, thus the BIPS can be controlled within a reasonable range by varying the temperature (Figure 12B). As it is shown in Figure 12A and Figure 12B, BIPS buildup has two components. These two components coms from two asymptotic exponents after fitting BIPS data (equation 13):

$$\varphi(q) = \varphi_1 \left(1 - e^{n-\frac{q}{q_1}}\right) + \varphi_2 \left(1 - e^{n-\frac{q}{q_2}}\right). \quad (13)$$

The first component is responsible for the steep rise of the phase shift during the first few nanocoulombs exposure and the second component is responsible for the gradual increase of the phase shift thereafter. BIPS does not depend on the beam current but it depends on the total applied dose (Figure 12C) (Danev et al., 2014).

In addition Figure 12 shows the phase shift development during the experiment which needs to be taken care during the automated data acquisition. After development of the phase shift beyond 0.7π the image looks blurry therefore there is a need to acquire the rest of the data from a fresh area. The blurriness of the image is not desired and it comes from an extra CTF maximum in the low frequency region (Danev et al., 2017).

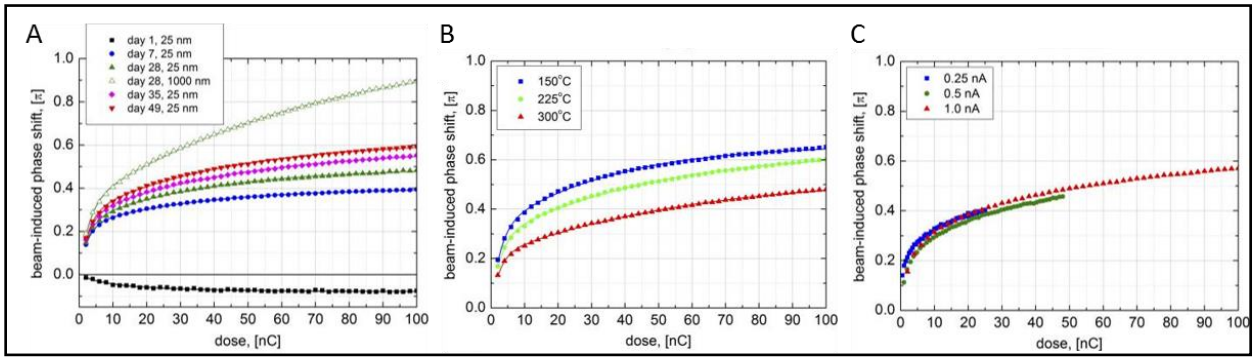

Figure 12: Beam induced phase shift (BIPS) on a 12 nm carbon film as a function of the total dose. (A) BIPS curves for a thin amorphous carbon film heated to 225 °C. Beam current is 1 nA and the beam diameter on the film is 25 nm (on-plane) and 1000 nm (off-plane). After 7 days the phase shift is positive and BIPS has stabilized. (B) BIPS curves at different temperatures (beam diameter is 25 nm); the beam current was 1 nA. Before the first measurement the film was kept at 150 °C for around 24 hours and then for around 1 hour the film was kept at 225 °C and 300 °C before their respective measurements. (C) BIPS curves with various beam currents (on-plane condition and the beam diameter is 25-nm); film age was 52 days, temperature was 225 °C. Plotted phase shift is the phase shift of the central beam relative to the scattered beams. Positive phase shift is a phase advance. Figure was adopted from (Danev et al., 2014).

Phase shift spots (patches) created with a beam diameter of 1 µm on the carbon film are visible in a low magnification image with a few millimeters defocus (Figure 13) (Danev et al., 2014). Spot created on the carbon film by electron beam was reported before and is known as the Berriman effect. Berriman effect is related to beam-induced charging and the beam-created spots appear darker than the background. However Figure 13A shows the spots are brighter than the background. moreover, the spot disappears for the image taken in-focus (Figure 13B) which indicates that the electron beam did in fact induce a phase shift and not beam induced etching of the carbon film., otherwise the spots would be visible with both defocus settings (Danev et al., 2014).

Figure 13C indicates a beam spot after creation next to a focused ion beam milled hole (white arrow). Ion beam milled hole was used as a reference to find the beam spot easier. Figure 13D shows the same spot as shown in Figure 13C but 5 days later where the beam spot disappeared. This suggests that the carbon film recovers itself after a period and being ready to be used again.

Figure 13E shows a fresh beam print on the film close to two old spots which were created over 10 days earlier. Unlike Figure 13D that the beam spot has recovered after 5 days, the two beam spots pointed by

black arrows have not recovered and they look darker than background. This shows a slight overshooting (in a sense of being darker than the background) of the film by electron irradiation which causes a different state of the film. The contrast of the darker spots is less than 1/10 of the contrast of the freshly beam spot therefore assuming the fresh spot has a phase shift of π/2, the overshoot spot in terms of phase is ~π/20. Having overshoot spot close to the central beam cannot cause any CTF distortion close to the central beam.

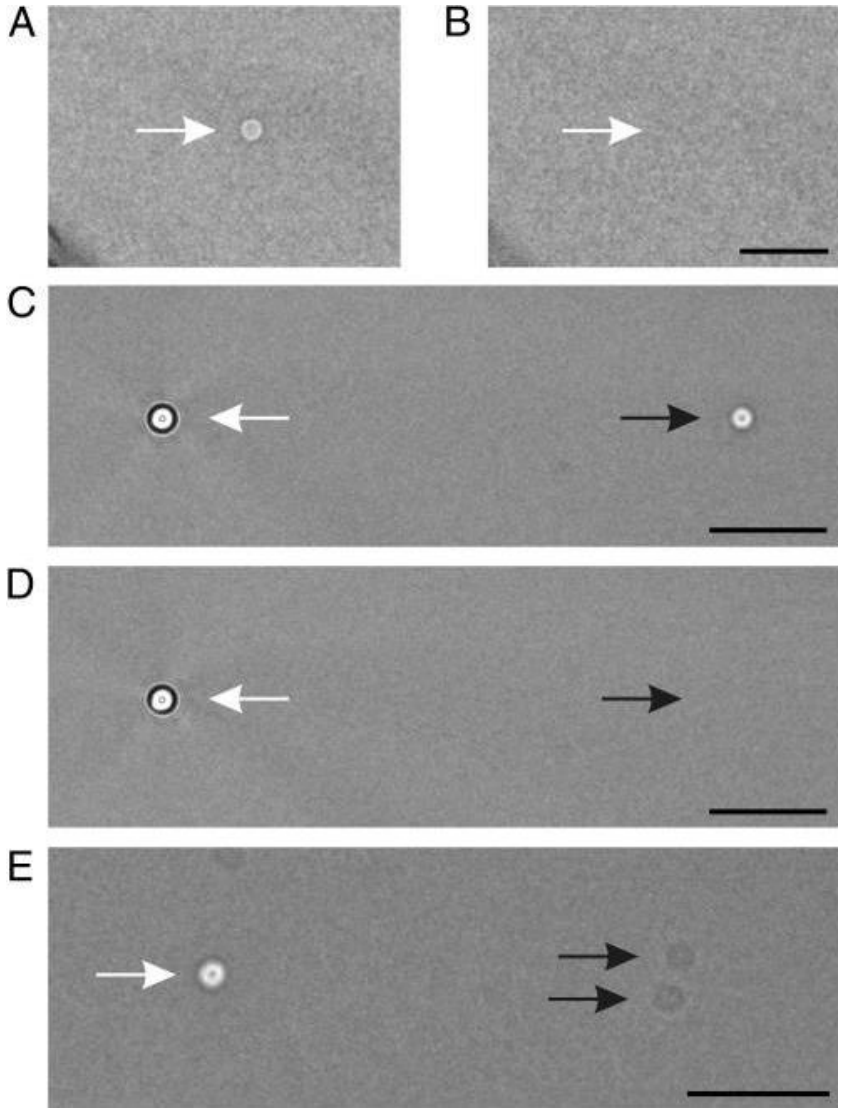

Figure 13: Images of 1 µm beam spots on a thin amorphous carbon film at 225 °c. (A) Low magnification image of a beam spot from a beam current of 1 nA and 100 nC dose at 15 mm defocus. (B) The same spot as (A) taken in-focus. (C) Hole (white arrow) produced with a focused ion beam SEM close to the beam spot (black arrow), defocus: 50 mm. (D) The same area as observed in (C) but taken after 5 days at 50 mm defocus. (E) A new beam spot (white arrow) next to old beam spots created 10 days earlier (black arrows) at 50 mm defocus. (Scale bar: 5 µm). Figure was adopted from (Danev et al., 2014).

Furthermore, the recovery speed of the phase shift patches was examined as a function of the temperature of the carbon film and the use of a liquid nitrogen-cooled anticontamination device (ACD). As it is shown in Figure 14 the recovery speed of the patches is temperature independent. However, the recovery is slowing down when the ADC was cooled, i.e. with liquid nitrogen. This result showed that there might be a direct connection between residual gases in the vacuum of the microscope which is Tecnai F20 in this case (e.g. residual gases from water, vacuum oils) and the recovery of the carbon surface. This in turn led to the conclusion that the Volta potential effect is most probably related to the surface chemistry of the film rather than due to changes of the bulk film material (Danev et al., 2014).

Beam spot patch recovery depends on whether the ACD is on or off. Since ACD can effect on the pressure and temperature of the gas molecules inside the vacuum of the microscope therefore it influences the adsorption rate on the surface of the carbon film. Based on the limited experimental data one can conclude that the recovery speed of the VPP in a microscope with good vacuum and with a large cryo-shield would be longer. On the other hand, the vacuum inside Tecnai F20 microscope is worse than Titan Krios, it is expected that the recovery speed of the VPP in Titan is longer than Tecnai F20.

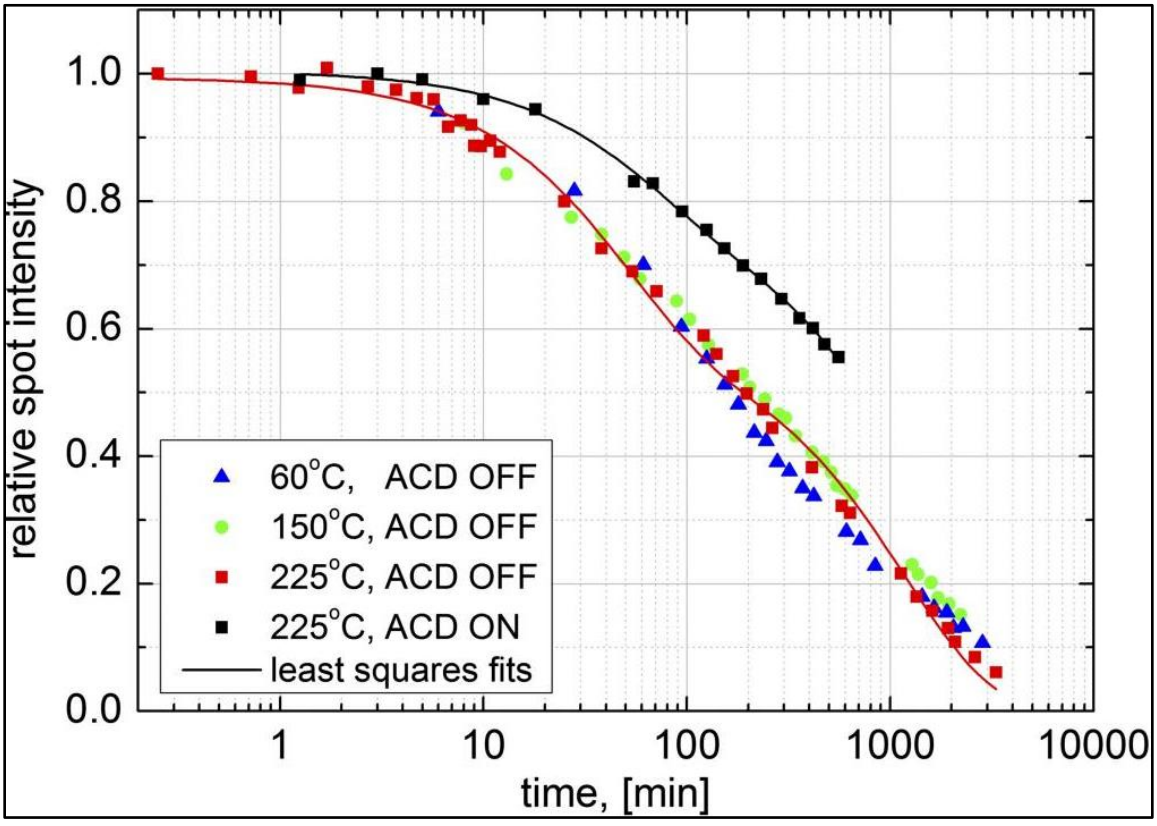

Figure 14: Observation of the recovery of beam-created spots on a thin amorphous carbon. The average intensity versus time during the relaxation of the amorphous carbon with/without anticontamination device. The beam spot (0.5 µm) was normalized by the original spot intensity after it was measured relative to the background. Figure was adopted from (Danev et al., 2014).

Here are some facts to exclude the possibility of the BIPS is not due to electrostatic charging effect as suggested in 2012 and caused CTF distortion (Danev et al., 2014):

1. The CTF behavior is opposite to that of beam induced electrostatic charging - defocused consecutive images show contrast enhancement and an inward movement of the FFT rings towards the center of the power spectrum which is an outward movement of the FFT rings in case of having beam induced electrostatic charging (Danev et al., 2014).
2. The observed phase shift patch from the electron beam in a low magnification mode, with sufficient defocus, shows a bright spot which is opposite to the Berriman effect. Berriman effect suggests that the primary electron beam irradiation creates a region of positive charge by loss of secondary electrons which has opposite sign compared to the negative Volta potential. Berriman effect considers this effect is due to beam-induced charging (Danev et al., 2014; Downing et al., 2004).
3. Figure 13A and Figure 13B show the experimental fact that the mechanism underlying the performance of the VPP is not due to beam-induced electrostatic charging effect. An explanation would be that the beam spot is not visible from the in-focus image while it would have been visible in case of beam-induce etching of the film (Danev et al., 2014).

Figure 15 illustrates the CTF from the VPP image compared to the no phase plate Thon rings from an amorphous carbon film specimen. The Thon rings with VPP indicate close to $\pi/2$ phase shift and are complementary to the no phase plate Thon rings. There is no distortion in the phase plate CTF. Moreover, Figure 15 shows the rotationally averaged and background normalized profiles of the FFTs with their CTF fits in black. In the CTF model of the VPP image, there is an additional parameter for the CTF estimation which is the phase shift compared to no VPP CTF. Both VPP and non-VPP FFTs show a very good fit. The defocus values used for CTF fitting from VPP image and non-VPP image are 482 nm defocus and 487 nm defocus respectively. The CTF fit for the VPP image gave a phase shift value of 0.54 π which is close to the ideal value of $\pi/2$. The 5 nm defocus difference between the VPP and non-VPP images is negligible and within the fitting error showing that the VPP does not exhibit any beam-induced charging or CTF deformation (Danev et al., 2014).

The signal from images acquired with the VPP is approximately 18% less than the signal from images without the VPP. This signal-loss caused by the 12 nm thin film of the phase plate is slightly higher than the expected decrease of 7 %. This additional decrease could come from several sources, such as (Danev et al., 2014):

1- Inelastic scattering from the phase plate could increase the noise and thus the background signal therefore the overall signal is decreased.
2- Thermal noise or oscillations of the Volta potential could be an additional factor increasing the background noise and contribute to a decrease in the overall signal.
3- Phase modulation arising from the roughness of the phase plate film could have an adverse effect as well; however, this contribution would be very small.

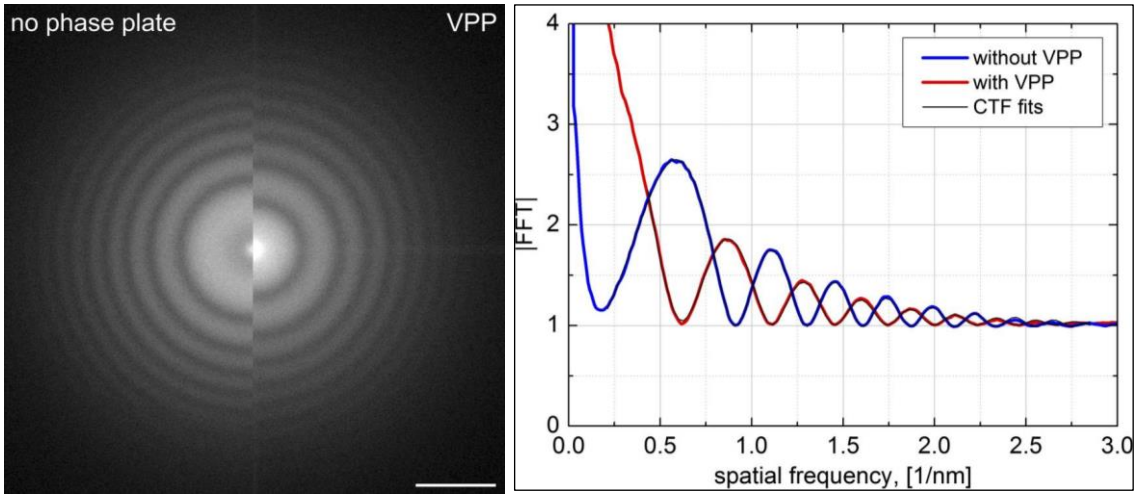

Figure 15: CTF performance of the VPP. (A) Fourier transforms of high magnification images with/without the VPP. (B) Rotationally averaged and background normalized profiles of the FFTs shown in A. (Scale bar: 1 nm^{-1}). Figure was adopted from (Danev et al., 2014).

Figure 16 shows expected VPP cut-on frequencies being on-plane (25-nm beam size) and off-plane (1000-nm beam size) condition compared to the observed positions experimentally. The solid arrows show the expected cut-on frequencies while the dashed arrows show the approximate experimental cut-on frequencies. To understand the best performance range of the VPP the phase shift patch of the on-plane (smaller beam size) and off-plane condition (larger beam size) were measured. The patch diameter from the on-plane condition was approximately 285 nm in diameter (11 times larger than the beam) while the patch size from the off-plane condition was 0.6 times of the beam size. The enlargement of the patch size in an on-plane condition could be arising from different reasons e.g. low-angle scattered electrons or secondary electron or auger electrons or combination of all activating the area around the central beam on the VPP. In the case of the larger beam the effective patch size is smaller than the actual beam which can be explained by the fact of being off-plane. Using the phase plate in an off-plane condition causes phase shift profile blurriness in Fourier space.

As shown in Figure 16, the cut-on frequency of the on-plane condition is lower than the off-plane condition and is thus suitable for high-contrast imaging of large specimen features. Moreover, phase shift development in an off-plane condition is larger than in an on-plane condition which is another indication for better performance of the VPP in on-plane condition (Figure 12A). In order to have high contrast and non-blurry images, the phase shift of the VPP should not develop too much therefore slow phase shift development is an advantage for imaging purposes (Danev et al., 2014).

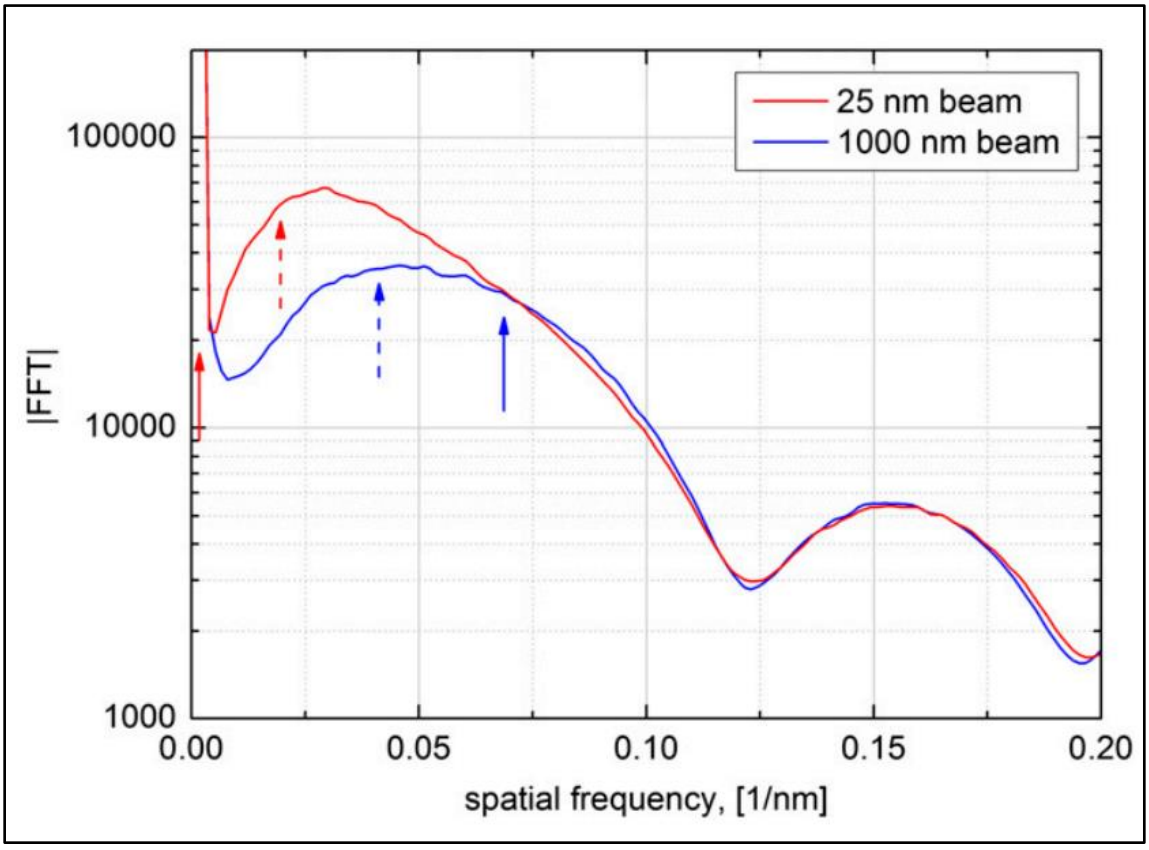

Figure 16: Rotationally averaged moduli of FFTs versus spatial frequency of images from the VPP in on-plane(25-nm beam diameter) and off-plane (1000-nm beam diameter) conditions. The solid arrows show the theoretical estimation of the cut-on frequencies and the dashed arrows show the approximate positions of the experimental cut-on frequencies. Figure was adopted from (Danev et al., 2014).

3.1.3. VPP performance vs Zernike phase plate and conventional TEM

Figure 17 shows a comparison of lacy carbon images taken with a ZPP (Figure 17A) and the VPP (Figure 17C). The ZPP image has fringing artifacts and lower contrast than the VPP image. Moreover, an additional software was used to filter the ZPP image to reduce the fringing artifacts (Figure 17B) (Danev et al., 2014).

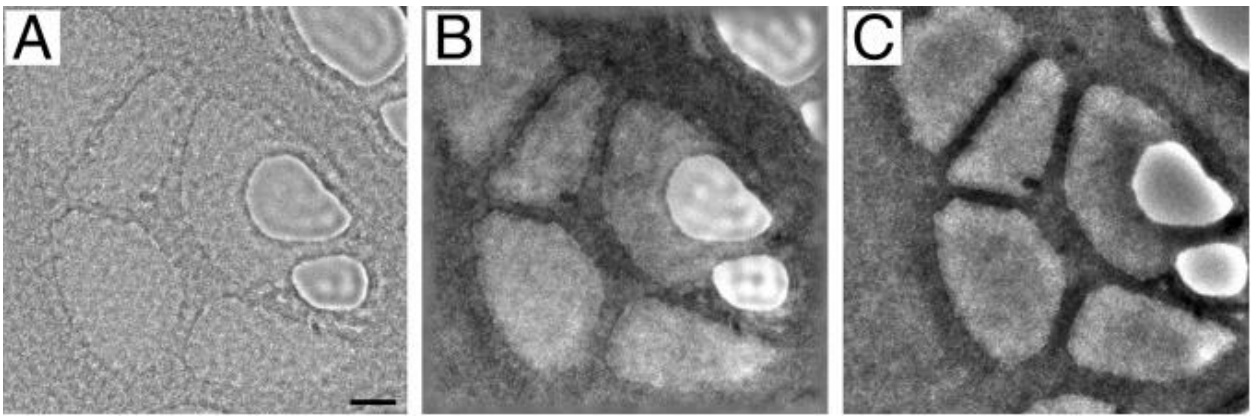

Figure 17: Lacy carbon film micrographs. (A) A micrograph acquired using a Zernike Phase plate. (B) Software-filtered version of A micrograph to reduce the fringing artefacts. (C) VPP image of the same sample. (scale bar: 20 nm). Figure was adopted from (Danev et al., 2014).

To test the performance of the VPP with a real biological sample, a vitrified worm sperm flagellum from *Lumbricus terrestris* earth worm was used. Figure 18A contains the micrograph taken with 5 µm defocus which shows lower contrast than the image taken with the VPP close to focus (Figure 18B). The doublet microtubules are well observed in both images (balck solid arrows) but some membrane proteins attaching to the inner and outer side of the cell membrane are easier to see in the VPP micrograph (dashed black arrows). In addition, there are no Fresnel fringes around the gold nanoparticles or a contaminant in the VPP micrograph which are visible in the image taken with defocus (white arrows).

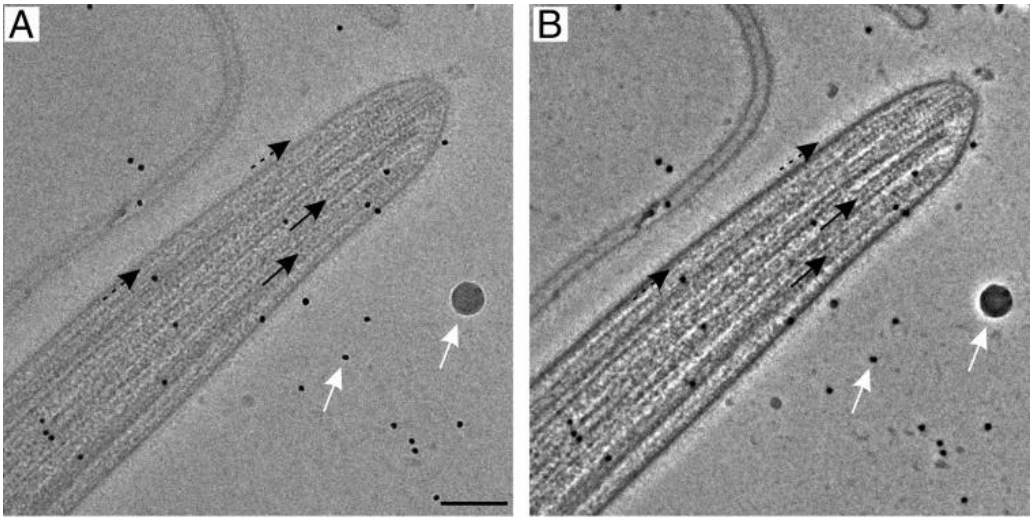

Figure 18: Micrographs of vitrified flagellum from Lumbricus terrestris sperm. (A) Micrograph acquired with 5 µm defocus without using the VPP. (B) A micrograph taken in-focus using the VPP. (Scale bar: 100 nm). Figure was adopted from (Danev et al., 2014).

Experiments in this section showed the development, some analysis and performance of the VPP which is based on beam-induced Volta potential on the surface of heated amorphous carbon film. The same phenomenon was responsible for the aging of the ZPP. After installation of the ZPP, the performance of

the phase plate gradually deteriorates which is independent of the usage. This behavior is called “aging” of the phase plate. Beam-induced contamination and CTF deformation are prevented by heating the film of the phase plate to around 200 °C. VPP has several advantages compared to the ZPP, such as longer life time, ease of use, no fringing artefacts and easy to automate the data acquisition. The longer life time comes from the fact that the created phase shift patches will disappear after a few days depending on how good the vacuum of the microscope is. The ease of use comes from not having a central hole to be precisely aligned on the central beam. The smooth onset of the phase shift of the VPP causes a bright halo around high-contrast features but no fringing artefacts. VPP should be used in the on-plane condition which has the lowest possible cut-on frequency and slower phase shift development.

The phase shift development of the VPP depends primarily on the total dose which can be calculated before starting the data acquisition and used to decide the time interval for changing the position on the VPP by moving to a fresh area (Danev et al., 2014). If the phase shift develops to the value more than 0.75π the image becomes blurry which should be avoided during the acquisition (Danev et al., 2017).

3.2. Applications of the Volta phase plate

3.2.1. Phase contrast single particle analysis of the small protein complex Prx3

The first attempt with the VPP revealed a 7.3 Å structure from 44 in-focus micrographs which were manually recorded. At this level of resolution secondary structure elements were visible and a folded C-terminus was detected similar to the reconstructions of Prx3 filaments and other Prx isoforms (Khoshouei et al., 2016; Schroder et al., 2000; Yewdall et al., 2016). (Figure 19B, D).

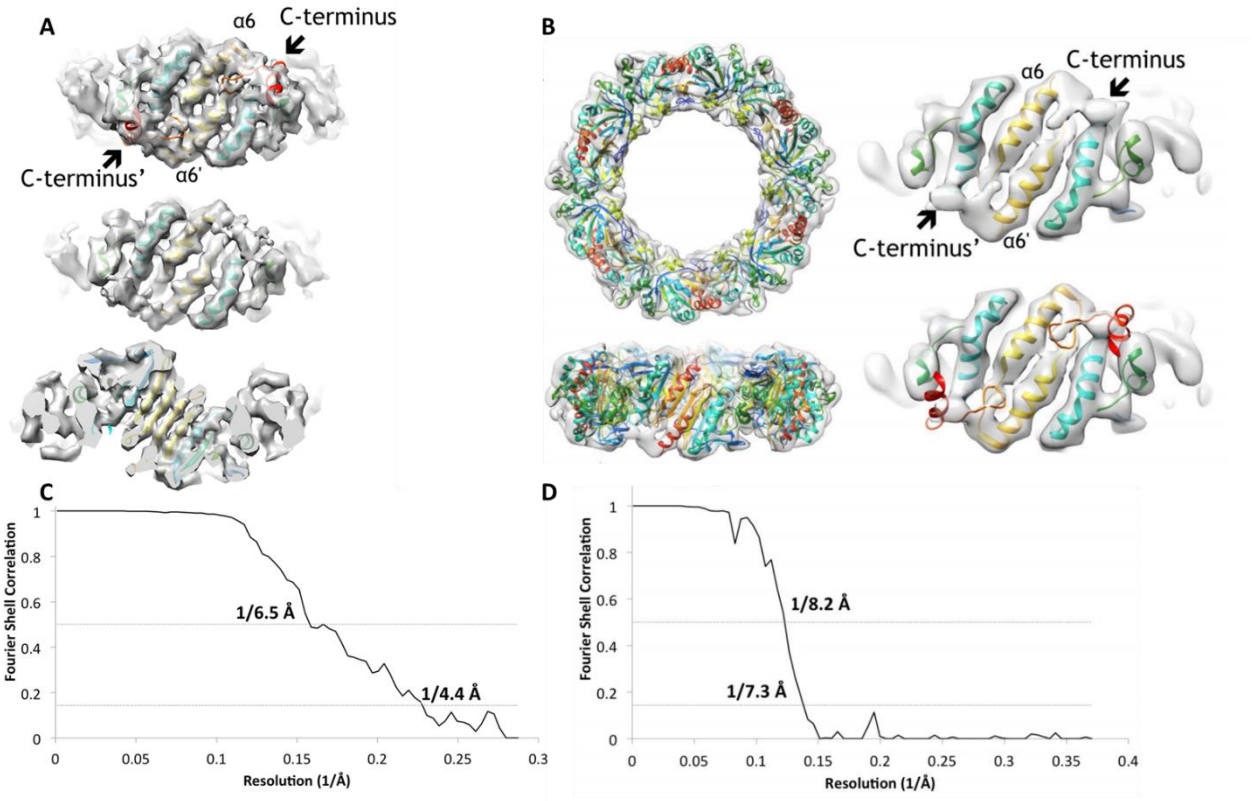

Figure 19: 3D density map of hPrx3 with docked crystal structure. (A) VPP reconstruction of hPrx3 with an overlaid crystal structure of hPrx2 (PDB 1QMV (Schroder et al., 2000)) at 4.4 Å resolution. (B) Pseudo-atomic interpretation of hPrx3 with docked crystal structure structure of bovine Prx3 (PDB 1ZYE (Cao et al., 2005)). (C) FSC curve shows hPrx3 at 4.4 Å resolution. (D) FSC curve of hPrx3 at 7.3 Å resolution. Data from (A) was taken automatically while the data from (B) was taken manually as a first attempt. Figure was adopted from (Khoshouei et al., 2016).

Based on the first attempt, VPP could be used for this particular specimen without further sample optimization or need to perform random conical tilt reconstruction (using tilted sample images) which could limit the resolution. The second attempt produced a structure at 4.4 Å resolution which was significantly better than the first attempt. (Figure 19A, C). The second map allowed better interpretation

of the structure including the C-terminal alpha helix. The main reason for not achieving a better resolution with the first dataset was the manual data acquisition which significantly limited the data volume and reduced the focusing accuracy (performed by observing a live FFT).

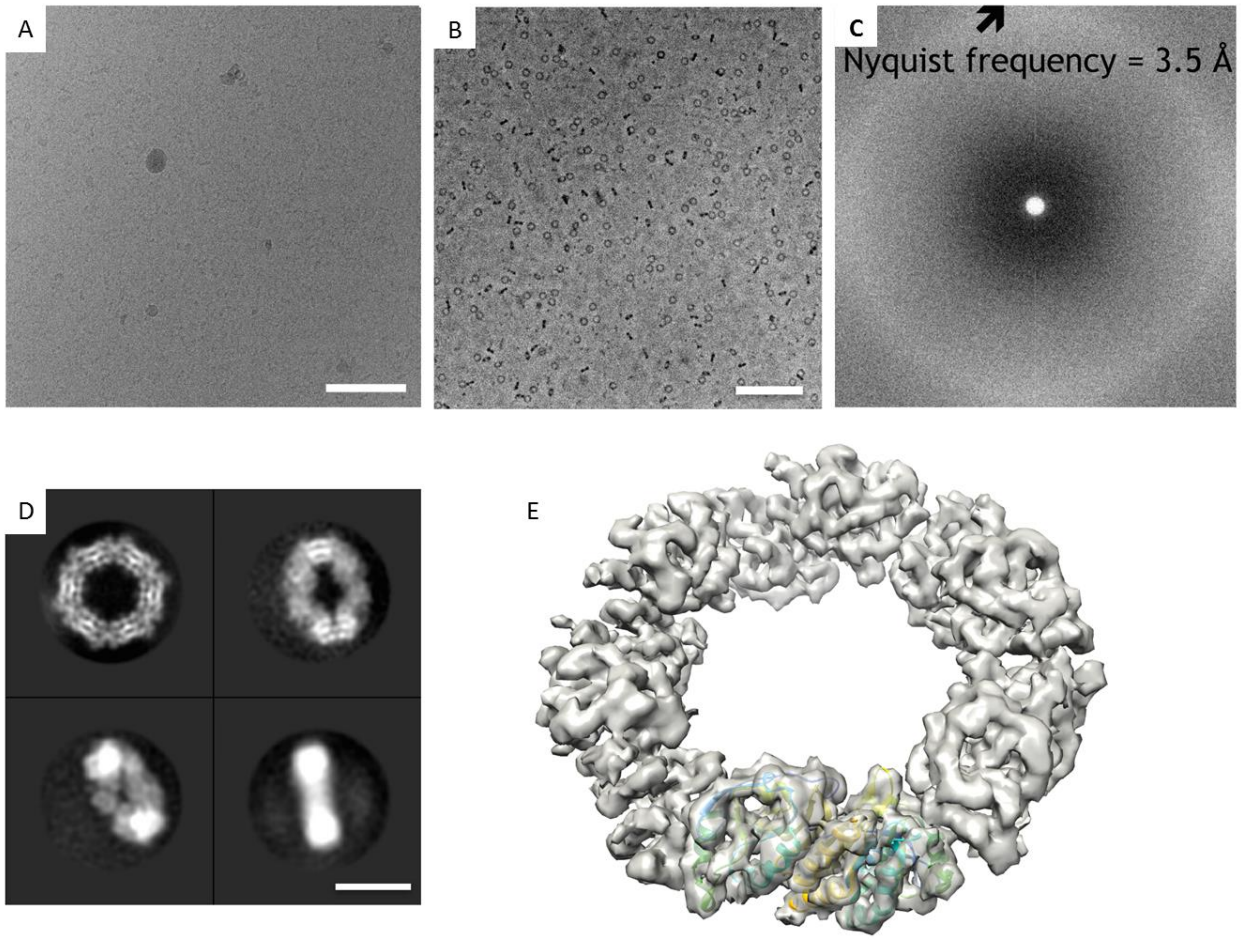

Figure 20: Structure of hPrx3 at near atomic resolution. (A) Micrograph of hPrx3 dodecamers in thick ice taken conventiaonally with 2.4 µm defocus (Scale bar: 100 nm). (B) In-fcus VPP micrograph enabing visualiation of particles in different orientations (Scale bar: 100 nm). (C) Fourier transform of (B) showing continuous signal with no oscillations of contrast transfer fuction. (D) Representative 2D class averages showing different orientations in thick ice (Scale bar: 10 nm). (E) Reconstructed 3D electron scattering potential map at 4.4 Å resolution with docked bovine Prx3 dimer structure. Figure was adopted from (Khoshouei et al., 2016).

Figure 20A shows a micrograph taken without using the VPP with 2.4 µm defocus exhibiting poor contrast. Figure 20B shows VPP electron micrograph in-focus presenting different orientations of particles with significantly higher contrast. Four representative 2D class averages are shown in Figure 20D featuring secondary structure motifs. Reconstructed 3D electron scattering potential map and a docked bovine Prx3 dimer crystal structure (PDB 1ZYE (Cao et al., 2005)) are shown in Figure 20E at 4.4 Å resolution. Despite the presence of 18% signal loss with the VPP described in subsection 3.1, this structure shows that SPA

using the VPP is not limited to a certain intermediate resolution seen in the application of other types of phase plates and manifested by very high B-factors (Khoshouei et al., 2016; Murata et al., 2010).

In-focus VPP micrographs have a CTF without any oscillations provide uniform information transfer from low to high spatial frequencies (Figure 20C). Given prominent attempts in high resolution structure determination of other similarly sized samples, it may be possible to solve the structure of hPrx3 by defocus based data acquisition (Bai et al., 2015b; Liang et al., 2015). However, without using a phase plate to increase the contrast, higher defocus has to be applied which would attenuate high resolution information in the micrographs (Cheng et al., 2015). The side views of hPrx3 were only present in thick ice areas. This first SPA attempt with the VPP showcases the possibility of getting near atomic structures of a relatively small complexes in thick ice. It was the first indication of the possibilities offered by the VPP in the study of more challenging samples in terms of molecular size, preferred orientation in thin ice, having more flexibility or particles embedded in detergent micelles or nanodiscs. In addition, the VPP could become a replacement for negative staining methods which are commonly used for sample screening and optimization but introduce structural artefacts.

3.2.2. Phase-plate cryo-EM structure of a class B GPCR-G-protein complex

This attempt resulted in a structure of a membrane protein of around 150 kDa at near atomic resolution. It was significant not only in technical terms but was also remarkable in the amount of biological information it provided. Here are some highlights:

1- First near-atomic resolution cryo-EM structure of a GPCR.
2- First full-length class B GPCR structure.
3- First full-length and active state class B GPCR structure. At the time of writing the manuscript, around 40 inactive class A GPCRs have been solved by X-ray crystallography technique, only few agonist-bound GPCR structures were available and only one GPCR complex structure had a full heterotrimeric Gαβγ protein. Among class B GPCRs, there were 2 inactive structures of the transmembrane domain solved by X-ray crystallography which were modified in order to be crystallized.
4- First full-length structure in combination with heterotrimeric G protein and intact peptide agonist bound.

The class B GPCR investigated in this study was the calcitonin receptor (CTR). It is a therapeutic target for bone diseases treatment. The purified CTR has a toroidal belt of detergent forming a micelle around the hydrophobic transmembrane domain. In general, membrane proteins are difficult targets for cryo-EM because they are small and are embedded in a detergent micelle or a nanodisc. The additional density of the micelle could interfere with the alignment of the particles during data processing but the results demonstrated that VPP single particle analysis is capable of dealing with such challenges (Rawson et al., 2016; Tsai et al., 2017).

A VPP micrograph of the plunge frozen sCT-CTR-G_s complex is presented in Figure 21A. 2D class averages showed secondary structure features with diverse orientations of particles (Figure 21B) which hinted at the possible successful 3D reconstruction. The transmembrane domain density was clearly visible even though it was embedded in a detergent micelle (Liang et al., 2017).

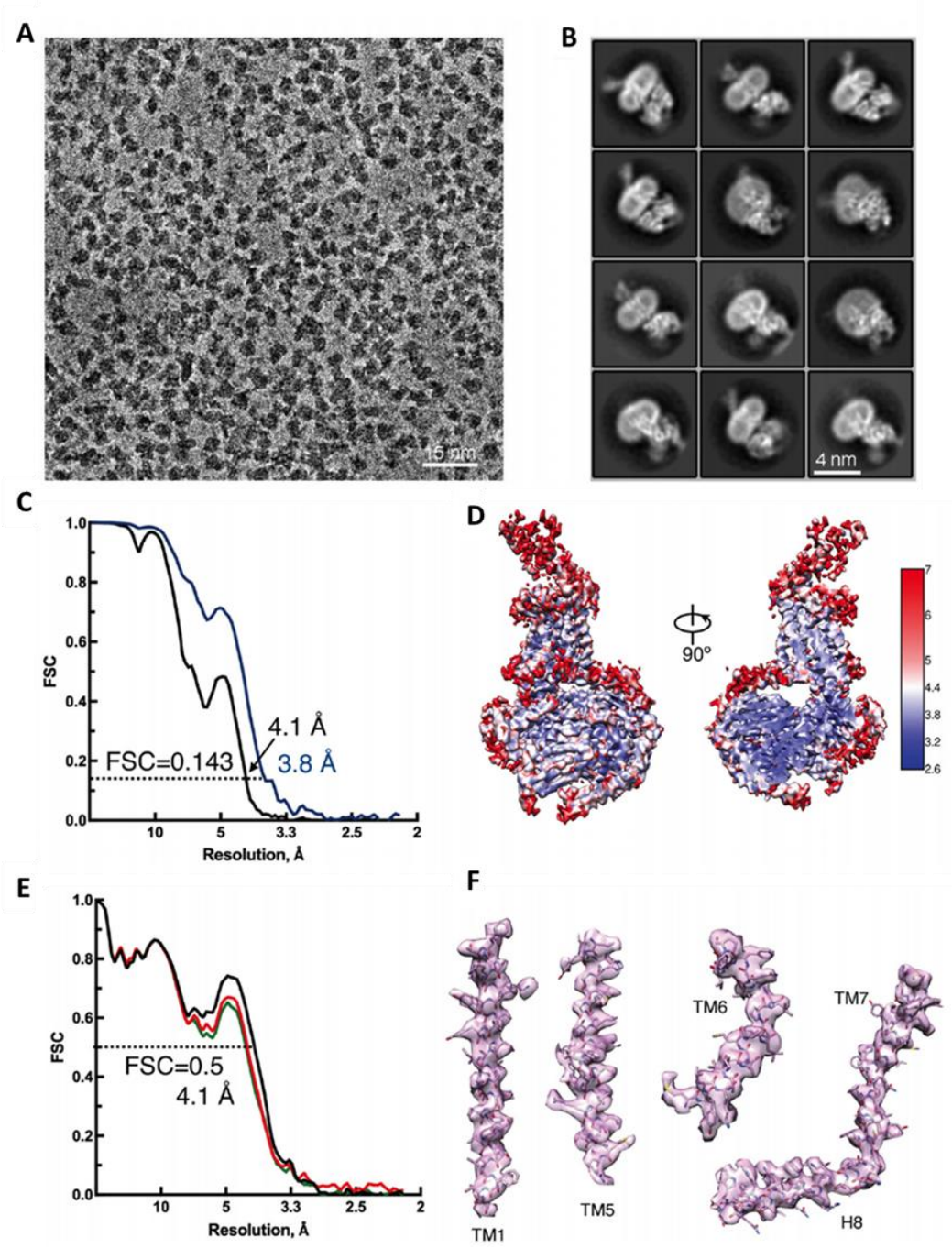

Figure 21: VPP cryo-EM structure of sCT-CTR-G_s complex. (A) VPP cryo-EM micrograph of sCT-CTR-G_s complex (scale bar: 15 nm). (B) Representative 2D class averages of the complex in maltose-neopentyl glycol/cholestrol hemisuccinate detergent micelle (scale bar: 4 nm). (C) FSC curves showing the nominal resolution of transmembrane domain (black) and G_s protein complex (blue) without the alpha helical domain at 4.1 Å and 3.8 Å resolution with the criterion of 0.143. (D) Local resolution map of the complex. (E) FSC curves of the refined model versus the cry-EM map (black), FSC curve of model refinement with the half map versus the same map (red) and FSC curve of the refined model with a half map versus the other half map (green) with the criterion of 0.5. (F) Transmembrane helices 1, 5, 6, 7 and 8 density. Figure was adopted from (Liang et al., 2017).

FCS curves in Figure 21C show a nominal global resolution of the transmembrane domain and G_s region of the complex. From the local resolution map, it was understood that the G_s protein part of the complex had the highest resolution while the extracellular domain had the lowest resolution in the cryo-EM map (Figure 21D). The weaker densities in the extracellular loops, intracellular loops and on top of the transmembrane helix 6 (TM6) were due to flexibility in those regions which could be required for the function of the receptor. FSC curves shown in Figure 21E are from the refined model versus the half map as well as between the refined model and the other half map for cross validation (Liang et al., 2017).

Not only the extracellular domain was less well resolved but also the $G\alpha_s$ α-helical domain had some flexibility and thus had lower resolution (Figure 22) (Liang et al., 2017).

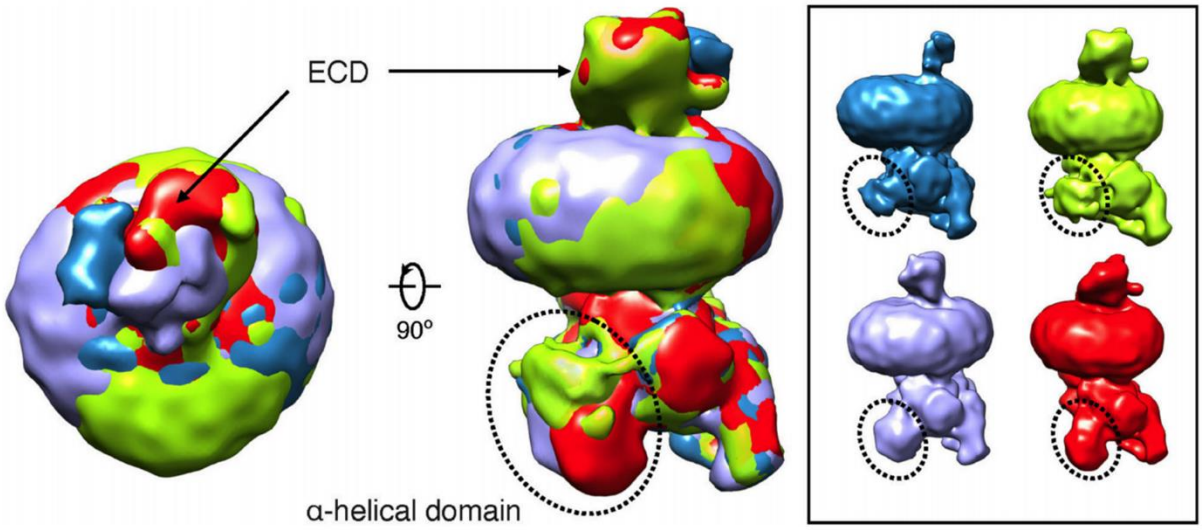

Figure 22: Extracellular domain and alpha helical domain flexibility. Different 3D classes show the flexibility of $G\alpha_s$ alpha helical and extra cellular domain of the CTR complex. Left panel shows the ovelaid maps from top and side views. Right panel shows four different classes which are representatives of $G\alpha_s$ alpha helical dynamics. Figure was adopted from (Liang et al., 2017).

Figure 23 shows the cryo-EM map of CTR at near atomic resolution. The map contains the transmembrane helix bundle with an additional density inserted within an opening area of the alpha helical bundle (attributed to sCT), G_s protein with nanobody and extracellular N-terminal domain. Due to poor resolution of the extracellular domain, Figure 23B shows the model except for the N-terminal domain. However, as discussed in the related paper there is an agreement with the isolated extracellular domain sCT structure (PDB accession code: 5II0) which could be fitted into the N-terminal domain of the CTR structure (Liang et al., 2017). Around residue 130, there is an additional density which could be due to predicted glycosylation in this area (Figure 24A) (Liang et al., 2017).

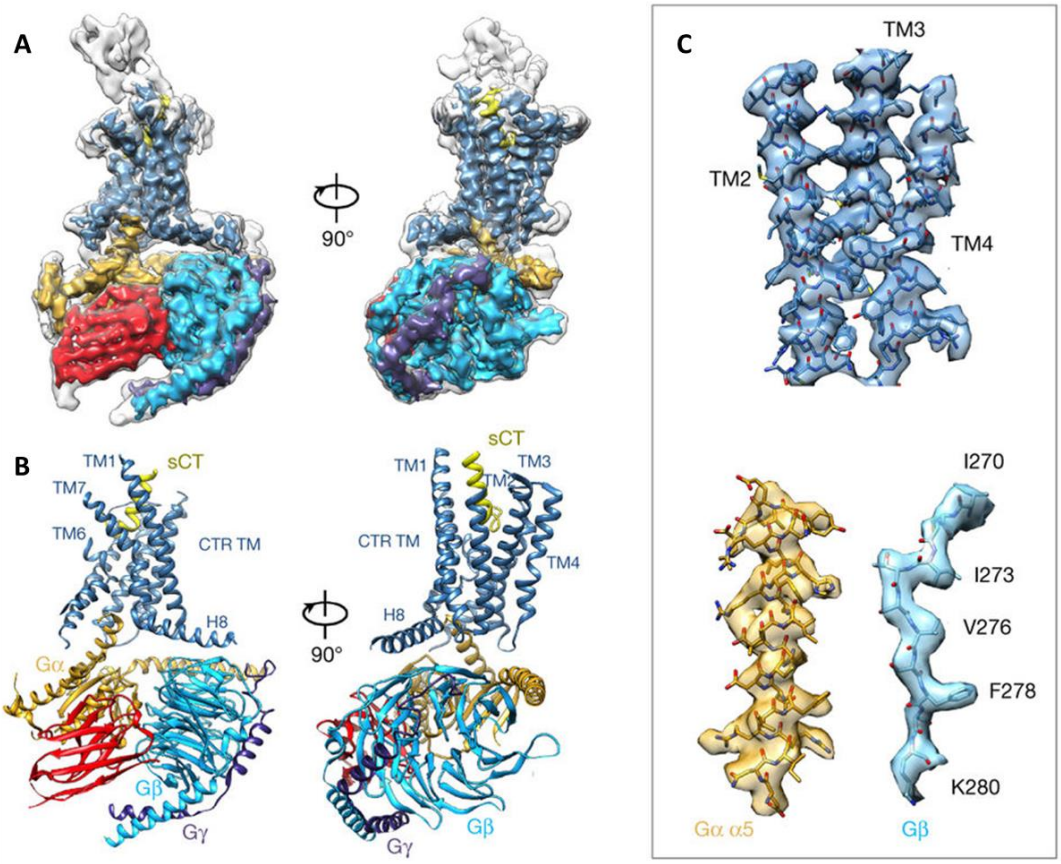

Figure 23: VPP structure of sCT-CTR-G_s. (A)Orthogonal views of sCT-CTR-G_s cryo-EM map. The colored density is the sharpened map with different regions (transmembrane domain is in blue; sCT is yellow; heterotrimeric G_s is copper, light blue and purple; Nanobody is in red) overlaid with the non-sharpened map. (B) The model based on the cryo-EM map. (C) Snapshots of different parts (transmembrane domain, Ras-like domain of G_α α5 and Gβ versus the model. Figure was adopted from (Liang et al., 2017).

As published in previous literature, the CTR orthosteric binding sites of some class B GPCRs are deeper than what is shown in the current study of the sCT-CTR structure (Figure 24B). The N terminus is located approximately one helical turn above a conserved polar network (Figure 24B). Polar residues are rarely found within the transmembrane core due to unfavorable hydrophobic environment. Sequence alignment of related receptors have identified a number of polar residues are conserved across all members of class B GPCRs (Wootten et al., 2013). These polar transmembrane residues are important for maintaining helical interaction and they form interaction networks that are required for protein conformational changes. The interaction networks are found to be implicated in receptor activation and stability, controlling effector specificity and biased agonism (Wootten et al., 2016a; Wootten et al., 2016b; Yin et al., 2017). Studies of these conserved polar networks facilitates the understanding of complex mechanism for activation and signal transduction of class B GPCRs.

Weak density in the cryo-EM map of the peptide made the N terminus modeling ambiguous.

Most likely the sCT has extensive contacts with all the transmembrane domains except TM4. Figure 24B shows outward movement of TM6 and TM7 which could be crucial to accommodate the N terminus part of the peptide (Liang et al., 2017).

At the time of writing of the manuscript there were no active class B GPCR structures available to compare with the CTR therefore a comparison was made based on inactive class B GPCR and class A GPCR (Liang et al., 2017).

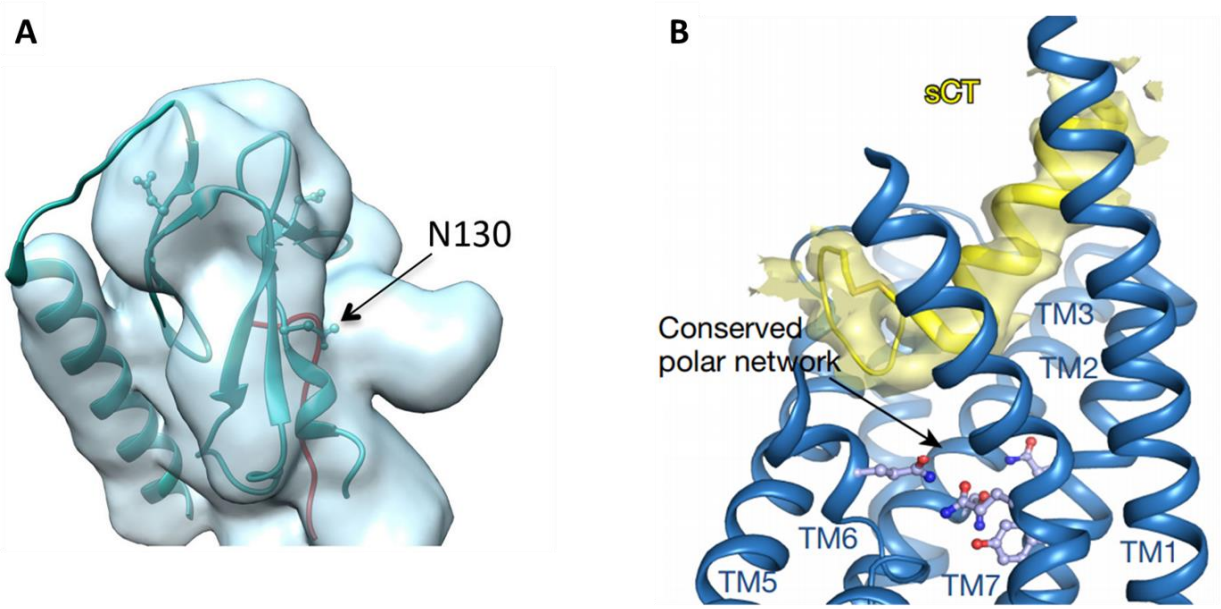

Figure 24: N-terminal ECD of the CTR and CTR transmembrane bundle. (A) Rigid body fitting of PDB: 5II0 into corresponding region of the CTR structure. (B) sCT structure in yellow in the CTR 7 transmembrane bundle in blue. Figure was adopted from (Liang et al., 2017).

After comparing inactive class B GPCR with the active CTR structure, it was understood that TM6 has a large outward movement (~ 15 Å) on the cytoplasmic side (Figure 25A). Alongside the outward movement, disordering and unwinding of TM6 was observed on the extracellular side (TM6 was kinked around 60° in the center). There was an inward movement at the top of TM1 and small outward movement on top of TM5 in the CTR structure compared to both inactive class B GPCRs (Figure 25A). The kink angle of TM7 in the CTR structure was similar to the inactive CRF_1R (yellow). On the extracellular side there was a 9 Å outward movement of TM7 in the CTR structure compared to the GCGR structure (purple) (Liang et al., 2017).

A class A GPCR (β_2AR) was also compared with the sCT-CTR_G_s complex. There were minor differences in terms of the G protein conformation in the class A GPCR (Figure 25B, grey) versus the CTR-G_s part (Figure 25B, Gαs, light blue; Gγ, purple; nanobody, red). There were several differences on the extracellular side

which are important for the peptide accommodation. TM1-3 and TM5-7 had the same location on the cytoplasmic side in both class A and B GPCR. TM5 helix was more extended in β_2AR-G_s complex than the CTR complex (Figure 25D). There was a long helix 8 present in the CTR structure while it was not observed in β_2AR complex (Figure 25B). TM6 and TM7 were more kinked in CTR and also a large inward shift towards TM7 was observed on the extracellular side of TM1 (Figure 25C). TM4 in the CTR structure had a different position compared to the β2AR complex on both the extracellular and the cytoplasmic sides (Figure 25C and Figure 25D). TM4 is an important component because it is the predominant interface for dimerization of class B GPCRs. Disruption of this interface leads to attenuation of G-protein signaling for all receptors (Liang et al., 2017).

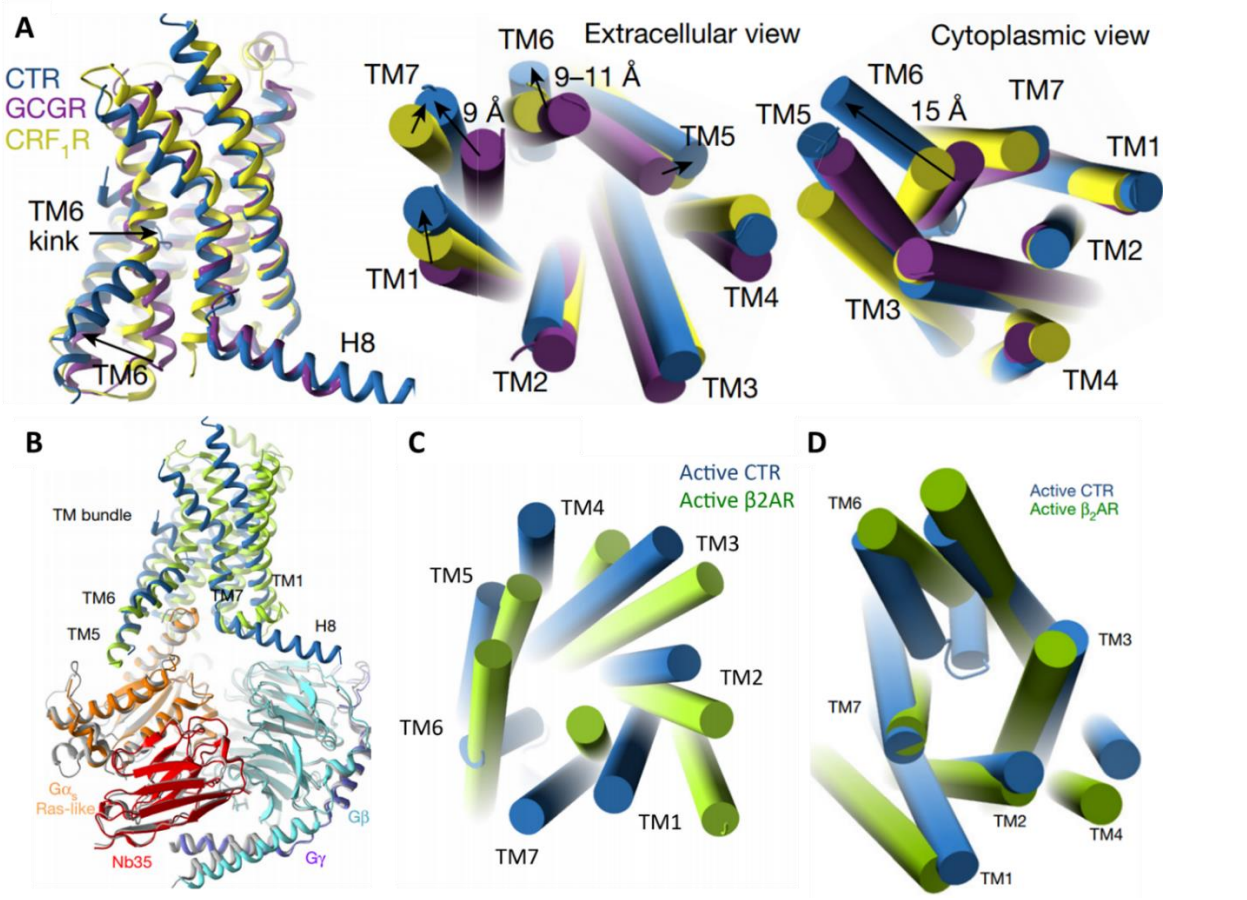

Figure 25: Comparison of inactive class B GPCR, class A GPCR and the activated CTR structure. (A) left panel shows the side view of the transmembrane bundle of sCT-CTR-G_s (blue) superposed on the transmembrane bundles of CRF_1R (PDB:4Z9G, yellow) and GCGR (PDB: 5EE7, purple). Middle panel shows the extracellular view and right panel shows the cytoplasmic view. (B) side view of CTR structure (CTR, blue; $G\alpha_s$, light blue; Gγ, purple; nanobody(Nb35), red) overlaid with β_2AR –Gs complex (G protein, grey; β2AR, green). (C) Extracellular view of CTR (blue) and β2AR (green) transmembrane domains. (D) Cytoplasmic view of CTR (blue) and β_2AR (green) transmembrane domains. Figure was adopted from (Liang et al., 2017).

In conclusion, a class B GPCR structure was solved using the VPP. VPP helped to reliably pick the particles and motion correct the subframes despite the relatively small particle size. The VPP structure provided insights into flexibility of the ternary complex and a peptide agonist binding site of the native unmodified protein. This could open a new pathway for design and drug development for this specific class of GPCRs.

3.2.3. Cryo-EM structure of haemoglobin at 3.2 Å determined with the Volta phase plate

For the first trial, in-focus VPP micrographs were collected (Figure 26A and Figure 26B). Since there were no visible Thon rings we could not estimate the CTF and therefore the data was reconstructed without any CTF correction. The reconstructed data led to a 6 Å resolution structure which was quite promising considering the small dataset and the low number of particles (Figure 26C). In-focus data acquisition requires very precise focusing for each micrograph which slows down significantly the acquisition rate. Additionally, the strong spherical aberration of the objective lens becomes a limiting factor when the resolution approaches 3Å , therefore for the second dataset we applied the defocused VPP hybrid approach (Danev and Baumeister, 2016).

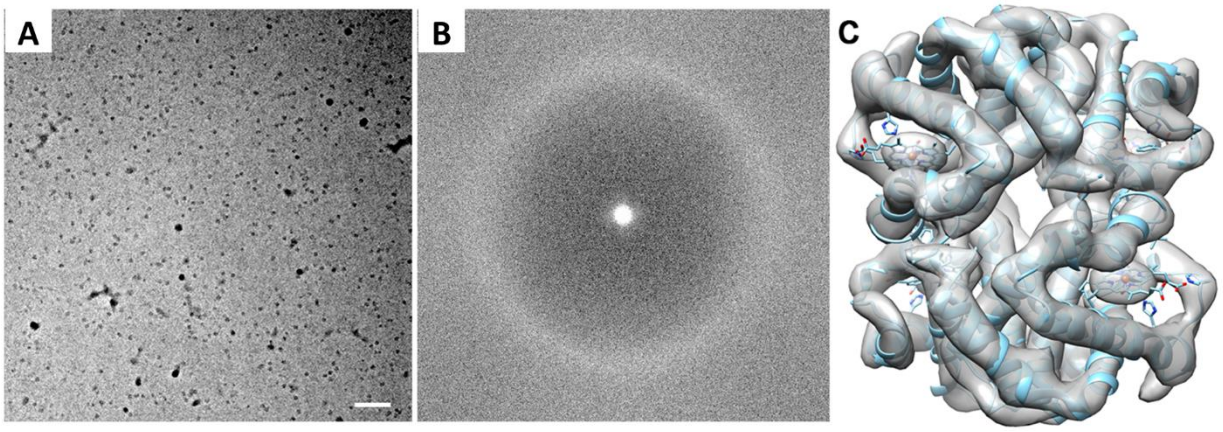

Figure 26: In-focus VPP imaging of Hgb. (A) VPP micrograph of met Hgb acquired at 20 nm defocus (scale bar: 50 nm). (B) Power spectrum of the micrograph in A, showing continuous information transfer from low-to-high spatial frequencies, with the amorphous ice ring visibile at 3.7 Å. (C) Three dimensional electron scattering potential map with fitted PDB model from crystal staructure (PDB 1A9W). Figure was adopted from (Khoshouei et al., 2017c).

Figure 27A shows a VPP micrograph from the second dataset with applied defocus. Hgb particles are clearly discernible in the micrograph were easy to pick. The power spectrum of the micrograph in Figure 27A is shown in Figure 27B where the Thon rings are visible and were suitable for accurate CTF estimation (Khoshouei et al., 2017c).

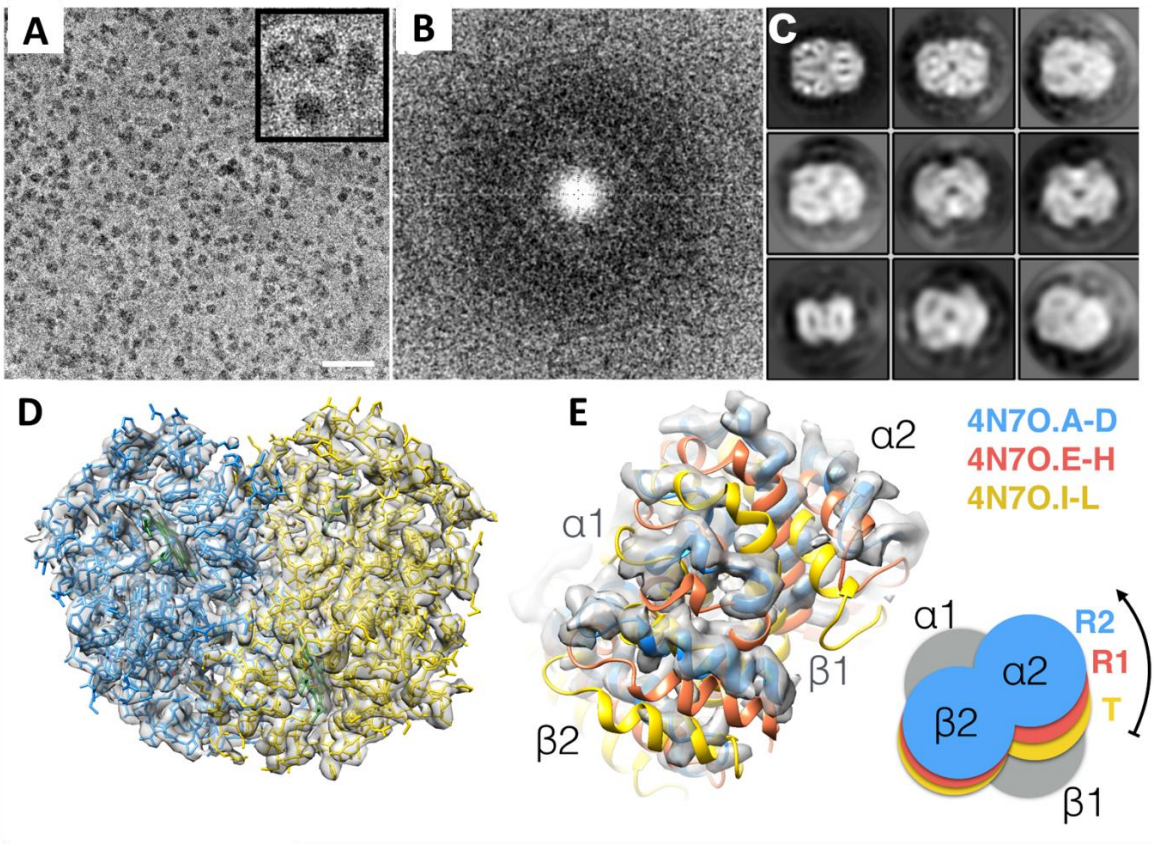

Figure 27: VPP imaging of Hgb at 500 nm defocus. (A) VPP micrograph of Hgb (scale bar: 30 nm). (B) Power spectrum of the image in (A). (C) Representative 2D class averages showing secondary structure features. (D) 3D electron scattering potentioal map and its related model of Hgb. (E) Reconstructed map of Hgb with three fitted models from three different states of Hgb present in crystal structure PDB 4N7O. The VPP dataset was consistent with PDB 4N7O in R2 state. Figure was adopted from (Khoshouei et al., 2017c).

Figure 27C contains representative 2D class averages of the Hdb which already show secondary structure features. The reconstructed volume is shown in Figure 27D with a resolution of 3.2Å. At this level of resolution, it was possible to see the side-chain densities and moreover to build an atomic model. As shown in Figure 27E, the reconstructed volume was fitted with three different conformations present in an available crystal structure (PDB 4N7O) adopting two relaxed states (R1/R2) and a tight state (T) (Shibayama et al., 2014). Using rigid-body fitting to dock the three conformations yielded cross-correlation values of 43%, 47% and 62% for T, R1 and R2 states respectively, which then led to the conclusion that the VPP structure in the R2 state (Khoshouei et al., 2017c).

At the achieved resolution, prosthetic haem groups and side chain densities were observed (Figure 28A). The 3D electron scattering potential map also contained water molecules as illustrated in Figure 28B with red spherical densities (Khoshouei et al., 2017c).

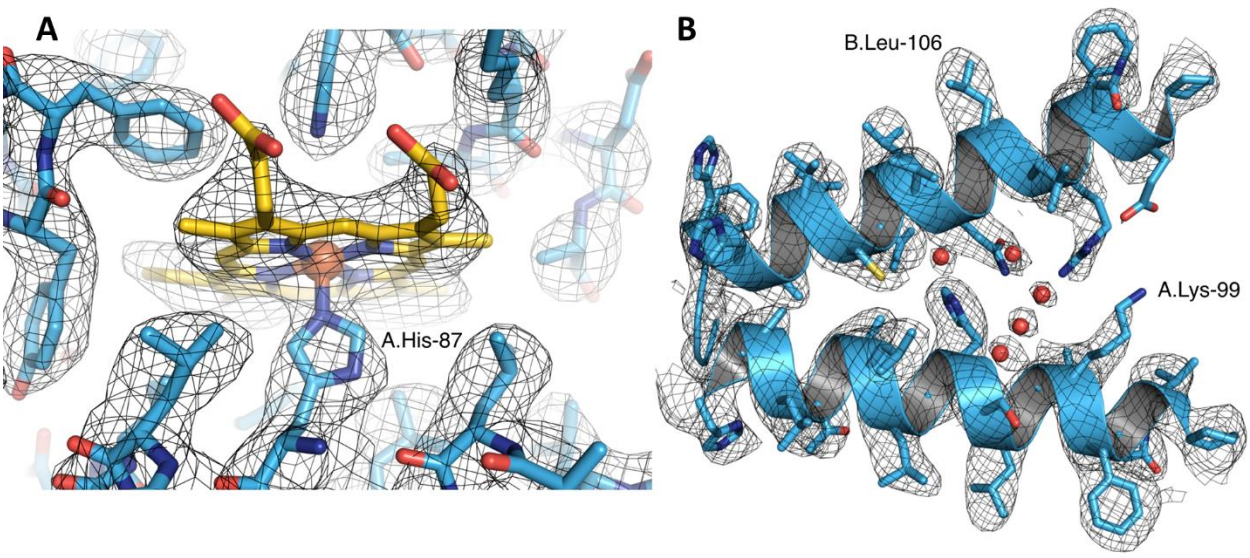

Figure 28: Details of the VPP reconstructed volume at 3.2 Å resolution. (A) The visibility of prosthetic haem group connected to a histidine residue. (B) visibility of side chains and water molecules (red spherical densities). Figure was adopted from (Khoshouei et al., 2017c).

The water molecule densities (red spheres in Figure 28B andFigure 29) were within hydrogen-binding distances from hydrogen-binding partners. The results were consistent with the conserved water molecules in a crystal structure of Haemoglobin (PDB 2DN1) (Park et al., 2006). To confirm the fidelity of the water densities, the dataset was reconstructed without imposing symmetry. The result reaffirmed the hypothesis with densities present at conjugate sites of the asymmetrically reconstructed map (Figure 29C, D and E) (Khoshouei et al., 2017c).

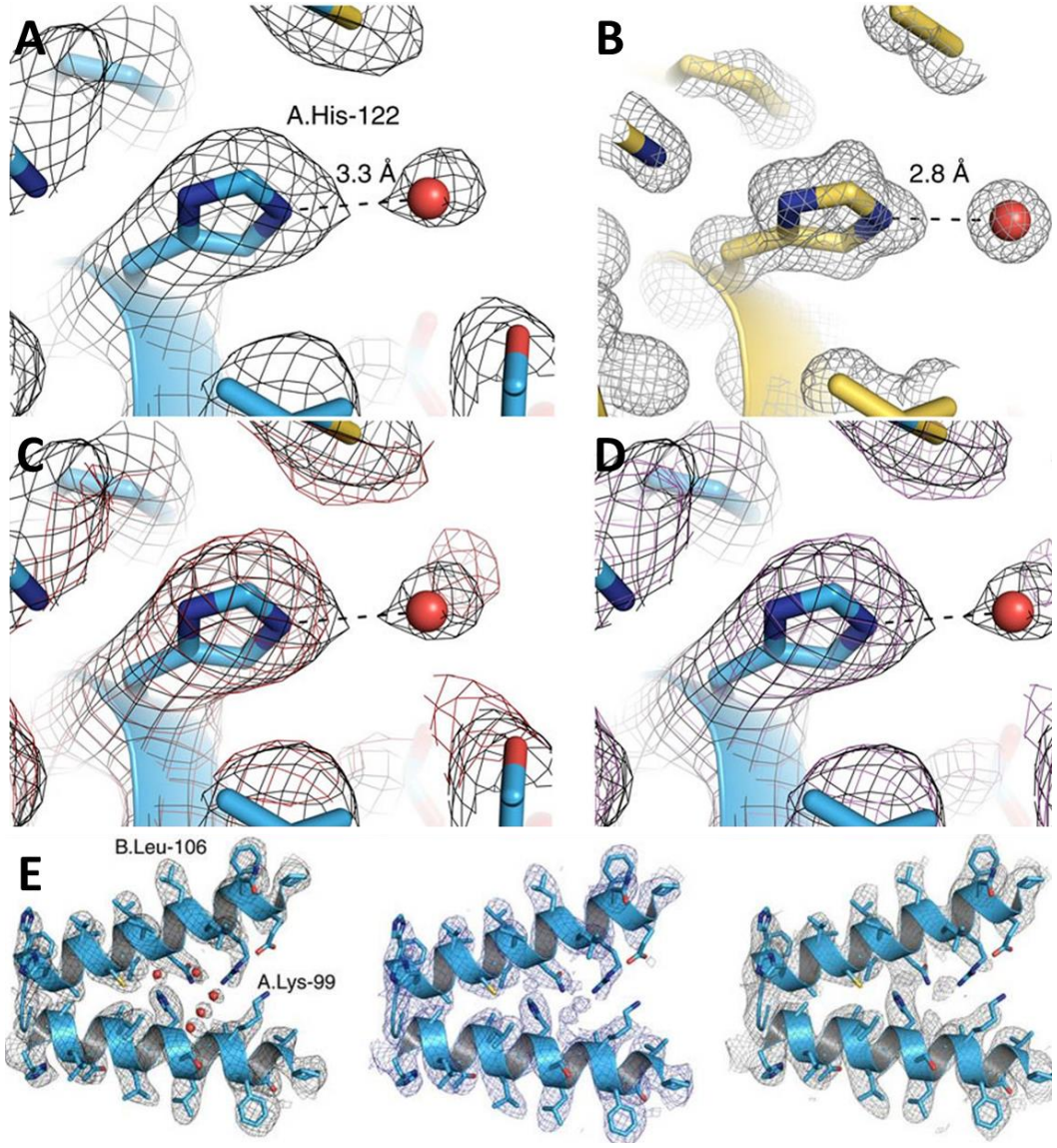

Figure 29: Validation of putative water molecules. (A) Reconstruction of the dataset with imposed C2 symmetry showing a water molecule ia the same position as a high resolution crystal structure (PDB 2DN1). (B) High resolution crystal structure of Hgb (PDB 2DN1). (C and D) overlaid two conjugate sides from the asymmetric map. (E) Visibilty of side chain densities and water molecules in reconstructions with imposed C2 symmetry (left panel), no symmetry (middle panel) and no symmetry from a subset of particles (right panel). Figure was adopted from (Khoshouei et al., 2017c).

Figure 30 shows the local resolution maps with and without imposed symmetry. The global resolution in both cases was determined by the so-called 'gold-standard' Fourier shell correlation=0.143 criterion shown in Figure 30 (Khoshouei et al., 2017c).

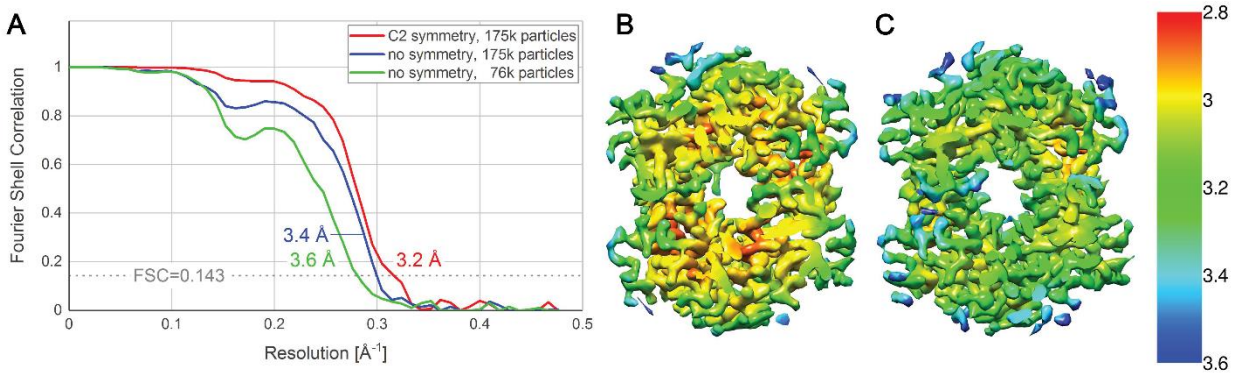

Figure 30: Resolution estimation. (A) FSC curves from C2 symmetry reconstruction (red curve), asymmetric reconstruction of the full dataset (blue curve) and asymmetric reconstruction from a subset of particles (green curve) at resolutions of 3.2 Å, 3.4 Å and 3.6 Å respectively. Local resolution maps from the C2 symmetry (B) and asymmetric (C) reconstructions of the full dataset. Figure was adapted from (Khoshouei et al., 2017c).

The most time consuming part of this project was the data analysis where the 3D classification and 3D auto-refinement steps were 10 times slower than similarly sized data sets from different proteins with a larger molecular weight. The reason is the broader Bayesian probability distributions and wider searches in 3D classification and 3D auto-refinement in Relion where in the case of larger particles the Bayesian probability distributions are narrower. Motion correction took 3 days and 17 hours with 4 hours of particle picking. 3D classification and 3D auto-refinement with imposed symmetry took 233 and 49 hours respectively while 3D auto-refinement for the reconstruction without imposing any symmetry took 175 hours (Khoshouei et al., 2017c).

In conclusion, the results demonstrated the possibility of structure determination of small complexes, such as Hgb, at atomic resolution with the help of the VPP. Solving structures at this level of resolution could be an alternative tool for determining the predominant conformation of a small complex in its native state complementing X-ray crystallography or nuclear magnetic resonance spectroscopy. The VPP holds promise for opening the doors to routine cryo-EM structural studies of complexes with molecular weights below 100 kDa which are currently very challenging (Khoshouei et al., 2017c).

3.2.4. Revisiting the structure of myoglobin with cryo-electron microscopy

After solving the structure of haemoglobin with molecular weight of 64 kDa, the next sample we tried is myoglobin with molecular weight of 17 kDa, roughly one fourth of that of haemoglobin. This makes myoglobin much more challenging, even with the VPP. Figure 31A shows a VPP micrograph of myoglobin with its corresponding power spectrum. Figure 31B presents 2D class averages from the dataset where different orientation of myoglobin could be observed. For comparison, Figure 31C shows a low-pass filtered crystal structure of myoglobin (PDB 1wla).

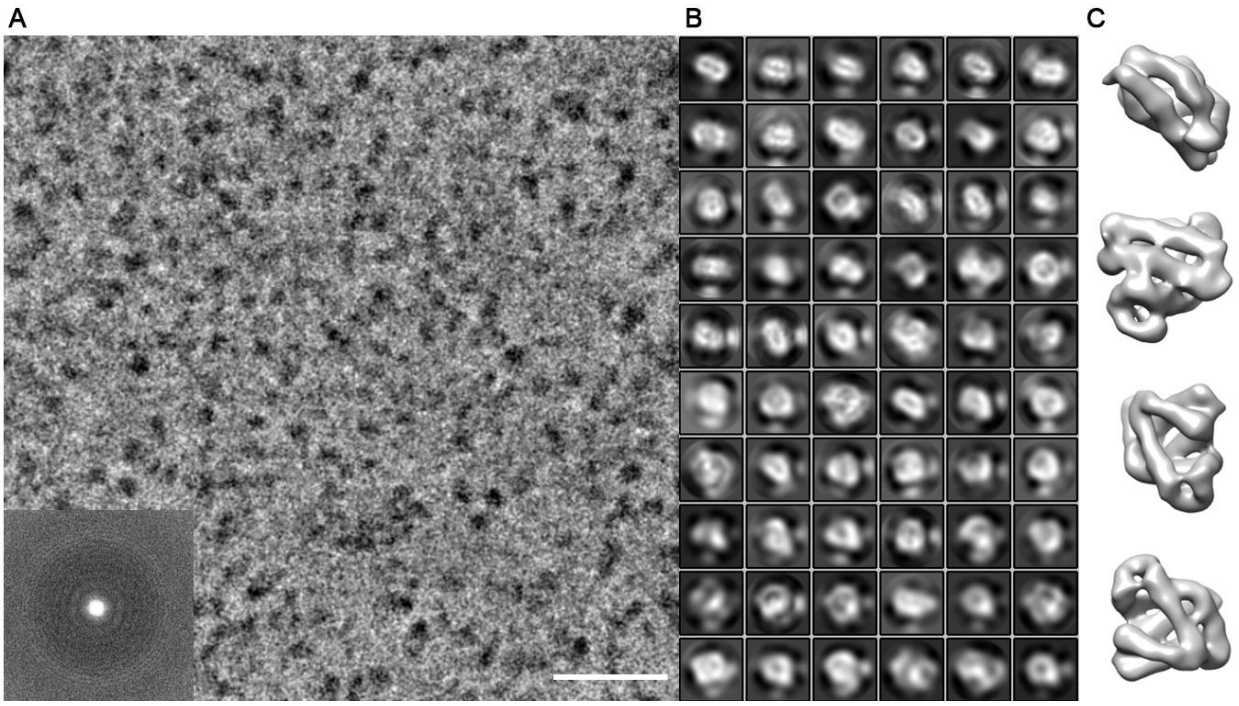

Figure 31: VPP imaging of myoglobin. (A) VPP micrograph of myoglobin and its corresponding power spectrum at 500 nm defocus (scale bar: 20 nm). (B) Representative 2D class averages. (C) Low-pass filtered crystal structure of myoglobin PDB 1wla for comparison with VPP cryo-em 2D class averages. Figure was adopted from (Khoshouei et al., 2017a).

Even though myoglobin 2D class averages were promising for getting a 3D structure, we were not able to produce a 3D reconstruction; 3D refinement attempts did not converge. This possibly shows that at the current technology level, myoglobin is too small and its individual particle images did not contain enough signal for accurate alignment and orientation determination (Khoshouei et al., 2017a).

3.2.5. Whole cell phase contrast cryo-electron tomography

An overview of a grid square containing mature worm sperm cells is shown in Figure 32A. The cell is about 80 µm long and has different compartments such as tubular acrosome (Figure 32B), nucleus (Figure 32C), midpiece (Figure 32D) and flagellum (Figure 32E). Based on 10 observed cells the acrosome, nucleus and midpiece have lengths of 4 to 5 µm, 17-18 µm and 1.5 to 2 µm respectively (Figure 32F). The acrosome is located on the proximal end of the nucleus and tapers in width from 470 nm at the nucleus end to 170 nm at the rounded tip. The nucleus has an elongated and straight structure and is filled with condensed chromatin. It has a constant width of 400-430 nm. The midpiece is the shortest fragment of the cell (1.5 to 2 µm) and has a width of approximately 470 nm. It contains six mitochondria with juxtaposed faces and is located between the nucleus and the flagellum. The largest organ is the flagellum with a width of approximately 400-450 nm. It contains a bundle of microtubules connected with numerous repetitive structures. Figure 32F contains a stitched batch-tomogram of the main part of a sperm cell, up to the beginning of the flagellum.

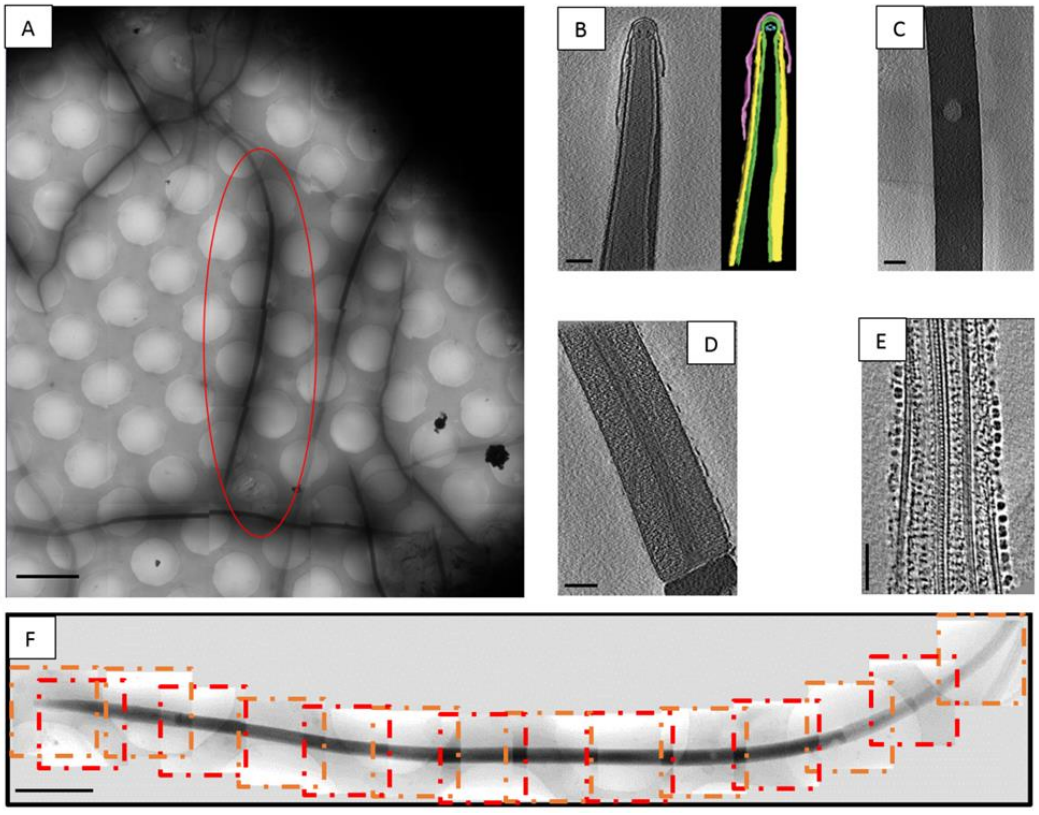

Figure 32: Batch CET with the VPP of different compartments of a Lumbricus terrestris sperm cell. (A) An overview of a grid square containing several sperm cells. (B) Acrosome. (C) Nucleus. (D) Midpiece. (E) Flagellum. (F) A batch-tomogram consisting of 15 stitched single tomograms. Scale bars: (A) 5 µm, (B, C, D, E) 200 nm, (F) 2µm.

Single tomograms were taken from different parts of the worm sperm in order to visualize compartments in more detail. Figure 33A, B show the tip of the acrosome. The acrosome contained several layers with various electron density, consistent with previous electron microscopy results (Henley, 1973; Jamieson, 1978; Jamieson, 1982; Shay, 1972). The high contrast provided by the VPP makes the visualization of transmembrane proteins possible. They were connected to the apical end of the acrosome (Figure 33B, black arrows).

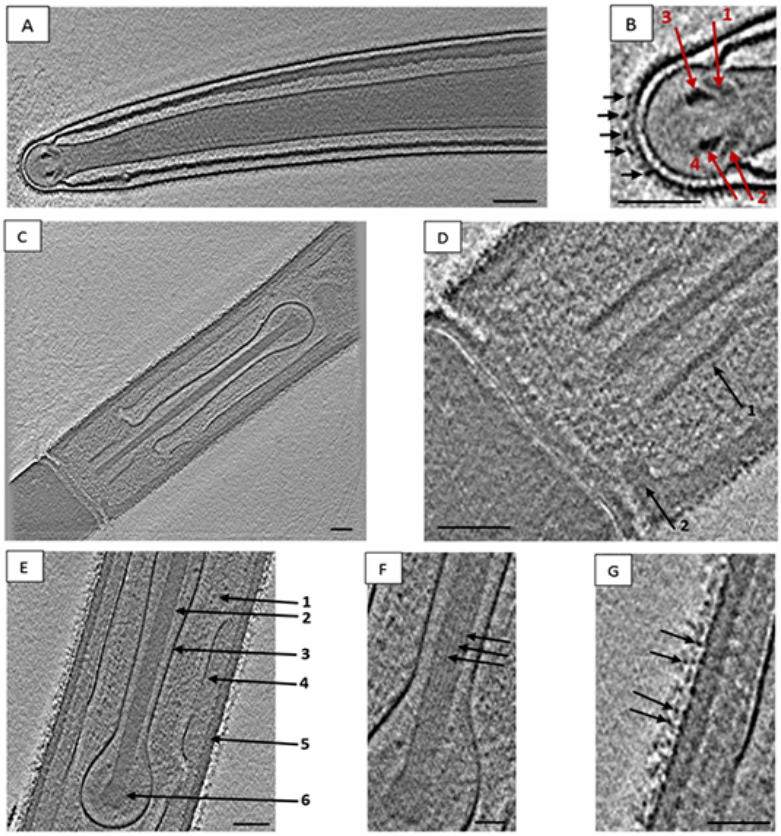

Figure 33: Single-axis VPP CET of the acrosome part of a Lumbricus terrestris sperm cell. (A) Acrosome. (B) Zoomed-in tip of the acrosome. Red arrows point to transmembrane proteins on the outer surface of the tip. Arrows 1 and 2 show a ring-shaped structure in the acrosome tip. Arrows 3 and 4 show another ring-like structure which has been observed in previous studies. (C) The end of the acrosome before its connection to the nucleus. (D) Zoomed-in basal compartment (arrow 1) and limen (arrow 2) of the acrosome. (E) Coagulum (arrow1), axial rod (arrow 2), inner and outer acrosomal vesicle's walls (arrows 3 and 4), wide layer (arrow 5) and capitulum (arrow 6). (F) Zoomed-in capitulum and axial rod. (G) Visibility of protein complexes on the outer surface of the membrane (black arrows). Scale bars: 100 nm.

Different parts of the acrosome are shown in Figure 33E. Acrosome contains coagulum (arrow1) (contents of the acrosomal vesicle), axial rod (arrow 2), inner and outer acrosomal vesicle walls (arrows 3 and 4), wide layer (arrow 5) and capitulum (arrow 6). All the organs are encapsulated between two plasmatic membranes around the cell. The basal compartment of the acrosome is shown in Figure 33D and it

contains a sheath of node and limen (arrows 1 and 2). Furthermore, the fibrous structure of the axial rod of the acrosome is visible in Figure 33F (black arrows) which has never been observed in previous works. The distance between the fibrils was measured to be about 8.4 nm. Figure 33G shows protein complexes on the cell membrane which are very difficult to see without the VPP (black arrows).

The nucleus contains condensed chromatin which is relatively dense and thus can impair the visibility of other existing structures. In order to have a thin section of the nucleus and try to visualize its structure focused ion beam (FIB) was used to remove a portion of the cell. Figure 34A shows the FIB-milled nucleus part of a sperm cell.

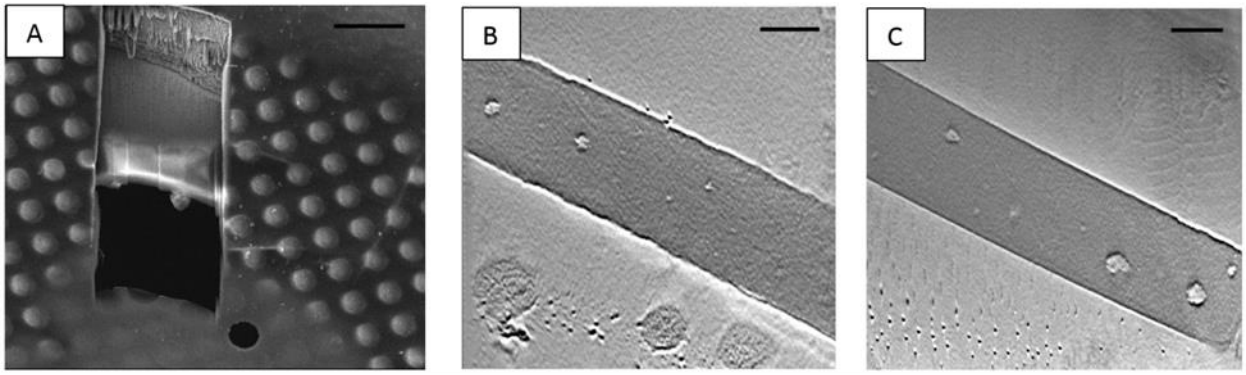

Figure 34: Single-axis CET with the VPP of a FIB-milled wedge of the sperm nucleus. (A) SEM image of the FIB-milled wedge of the nucleus using around 19 µm rectangular milling window, 30 keV acceleration voltage and a shallow milling angle of 7 degrees. (B, C) Slices through a tomographic reconstruction from the FIB-milled wedge. Scale bars: (A) 10 µm, (B, C) 200 nm.

Figure 34B, C contain slices from a tomogram collected using the FIB-milled wedge specimen. The only visible structures in the nucleus were several holes with various sizes within the packed chromatin. The holes had some decorations around their periphery. The nature and origin of these holes was not well known but they could have been a result of condensation failure in the last step of spermiogenesis when the majority of the DNA is bound to protamines and minority is still bound to histones (Boitrelle et al., 2013).

Figure 35A-C show slices from tomograms of the midpiece. The midpiece is an important organ providing the energy for fertilization and locomotion. Figure 35A inset shows a cross-section of few pyramidal mitochondria located around the central axis. Each mitochondrion contained dense materials which were tightly packed, twisted and formed cylindrical and straight structures (Ferraguti and Jamieson, 1987). Figure 35B shows a zoomed-in slice of a tomogram where few cristae were present in each mitochondrion. A slice of another tomogram taken with smaller pixel size is shown in Figure 35C where a few more details

were visible, such as granules in the area between midpiece and flagellum, the transition gate and the triplet microtubules before the transition gate (inset image of Figure 35C).

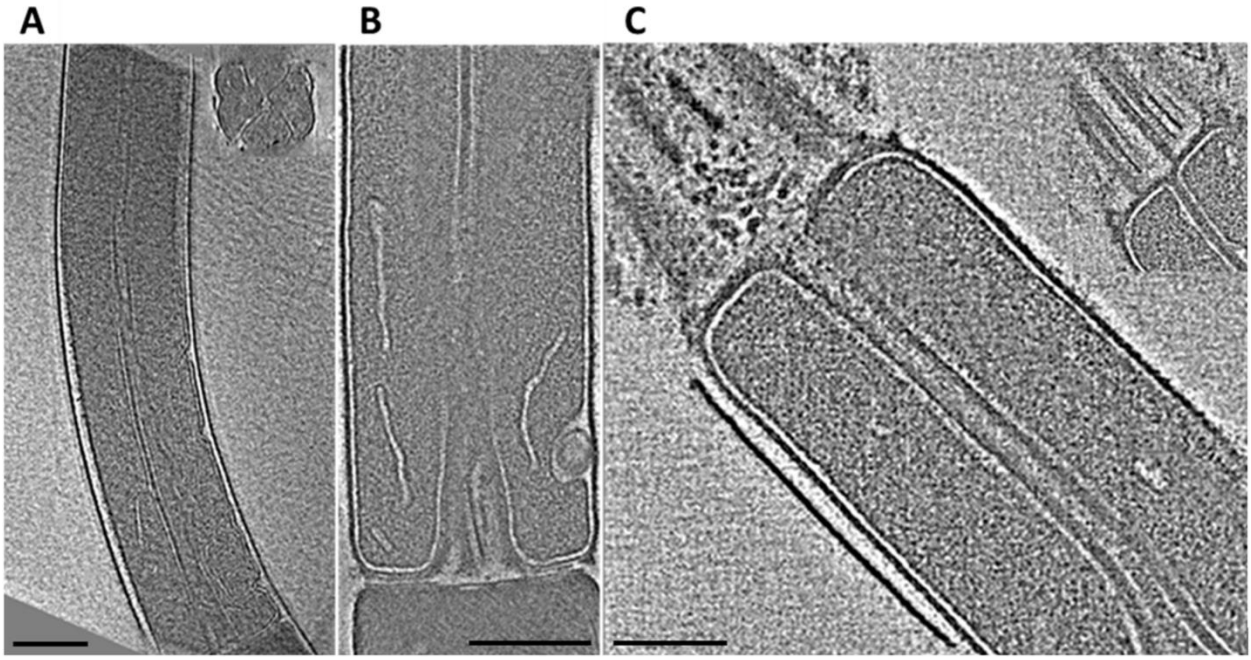

Figure 35: Dual-axis VPP CET of the midpiece. (A) A slice through the tomogram with its corresponding cross section showing juxtaposed mitochondria. (B) A zoomed-in slice containing a few cristae. (C) A slice from a tomogram taken at higher magnification showing the transition gate and some granules between the midpiece and the flagellum. The inset image shows triplet microtubules close to the midpiece. Scale bars: 200 nm.

In this tomographic technique (dual-axis CET) the total electron dose is divided between two single axis tomograms. Therefore, the contrast of each tomogram is weaker than the contrast for one single axis tomogram at the same total electron dose. The combination of dual-axis CET with the VPP facilitates the tracking part of the reconstruction which is critical for the quality of reconstruction and the alignment of the two single tomograms.

Figure 36A-C show slices from a tomogram of the flagellum. The flagellum is responsible for the motility of the sperm cell. It consists of nine pairs of peripheral microtubule doublets (Figure 36B, black arrows), two central singlets and dense granules (Figure 36A). The dense granules are glycogen and serve as energy storage for ATP production by the six mitochondria located in the midpiece (Anderson et al., 1967). The improved contrast by the VPP made other fine features in the flagellum visible. Radial spokes Figure 36C, arrow 1) are components of the flagellum that serve as mechanochemical transducers that control the sliding motion of the microtubules. Inner and outer dynein are the subunits generating the sliding motion between the nine doublets and are shown in Figure 36C (arrow 2 and 3) (Pigino et al., 2011). Another visible fine structure resolved in the tomogram slice is the repetitive cross bridges between the central

microtubule pair. The distance between these cross bridges was measured to be around 16 nm (Figure 36A). This is consistent with previous observation in thin-sectioned lamellibranch gill cilia (Warner, 1976).

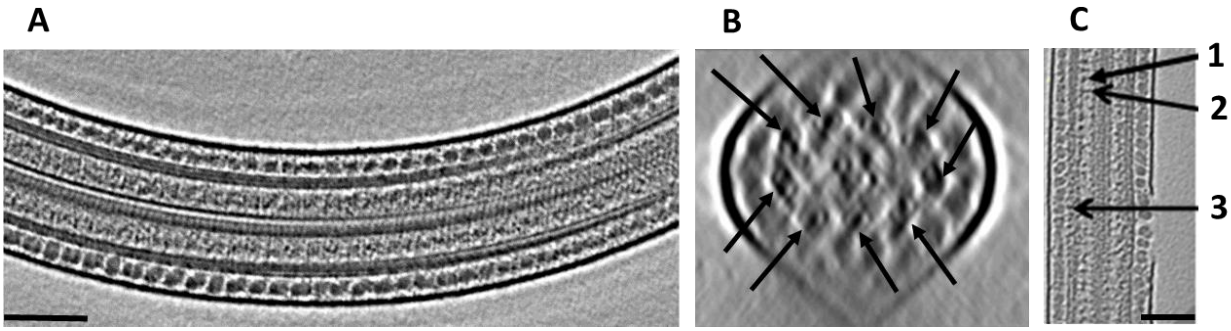

Figure 36: Single-axis VPP CET of the flagellum. (A) One slice through the reconstructed tomogram showing two connected microtubule singlets with cross bridges in the middle, two microtubule doublets and glycogen granules (black spheres). (B) Cross section through the flagellum showing 9 microtubule doublets (black arrows). (C) Visibility of radial spokes, inner and outer dynein (black arrows 1-3 respectively). Scale bars: 200 nm.

In conclusion, batch cryo-tomography with the VPP was demonstrated. This technique enabled a better understanding of the morphology of the whole vitrified cell and not only a small portion of it. Different parts of the acrosome were visualized with single-axis CET. In addition to what has already been described in the literature a ring shape structure at the tip of the acrosome, the fibrous structure of the axial rod and protein complexes on the surface of the acrosome tip were revealed. In order to investigate the structural details of the nucleus, a FIB-milled cryo-specimen was observed with the VPP. The only visible structures were holes with various sizes and decorations around their periphery. The origin of the holes was not clear but they could be extra volumes left over after the majority of the DNA has bound to protamines. Dual-axis CET combined with the VPP was used to mitigate the missing wedge problem and to investigate the structure of the midpiece. Several tightly packed mitochondria with juxtaposed walls and few cristae were observed. Those tightly packed mitochondria form a cylindrical structure between the nucleus and the flagellum. The contrast improvement by the VPP made the granules at the transition gate between the midpiece and the flagellum visible. These granules could be the source or the product of ATP synthesis in the mitochondria. The flagellum was also imaged using CET combined with the VPP. The results showed 9 pairs of peripheral microtubule doubles and 2 central singlets with dense glycogen granules around the microtubules. In addition, radial spokes, inner and outer dynein were clearly visible in tomograms. The improved contrast by the VPP made it possible to resolve the cross-bridges between the two microtubule singlets.

3.2.6. Subtomogram analysis using the Volta phase plate

As shown in Figure 37A, isolated mammalian 80S ribosomes were clearly visible in a single slice from an unfiltered reconstructed VPP tomogram (Khoshouei et al., 2017b).

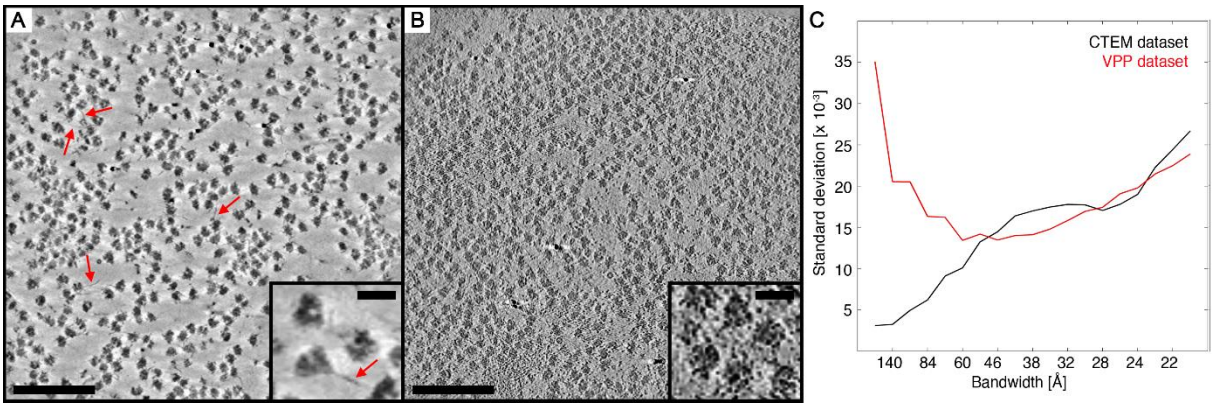

Figure 37: A VPP tomogram vs a CTEM tomogram of isolated mammalian 80S ribosomes. (A) One slice from an unfiltered in-focus VPP tomogram taken with a pixel size of 2.1 nm. (B) One slice from an unfiltered CTEM tomogram taken at a nominal defocus of 3.5 µm and a pixel size of 2.1 nm. (C) Mean standard deviation vs spatial frequency from 100 subtomograms from the tomograms shown in (A) and (B). (scale bars from full tomograms: 200 nm, scale bars from inset images: 30 nm). Figure was adopted from (Khoshouei et al., 2017b).

Figure 37B shows one slice from a CTEM reconstructed tomogram taken with nominal target defocus of 3.5 µm exhibiting lower contrast compared to VPP tomogram. The visibility of filamentous structures coming out of some ribosomes was striking in the VPP tomogram (Figure 37A). These were most likely ribosomal RNA expansion segments (Melnikov et al., 2012). To compare the contrast of ribosomes in VPP tomograms and CTEM tomograms, mean standard deviation of 100 subtomograms containing ribosome was measured at various spatial frequencies. The contrast in VPP subtomograms was 3 to 10 fold higher at low frequencies (Figure 37C).

In order to investigate the suitable focusing parameters, 10 different tomograms were acquired as shown in Figure 38 Defocus target of 0 and no defocus offset were two critical parameters for retention of high-resolution signal in the VPP dataset.

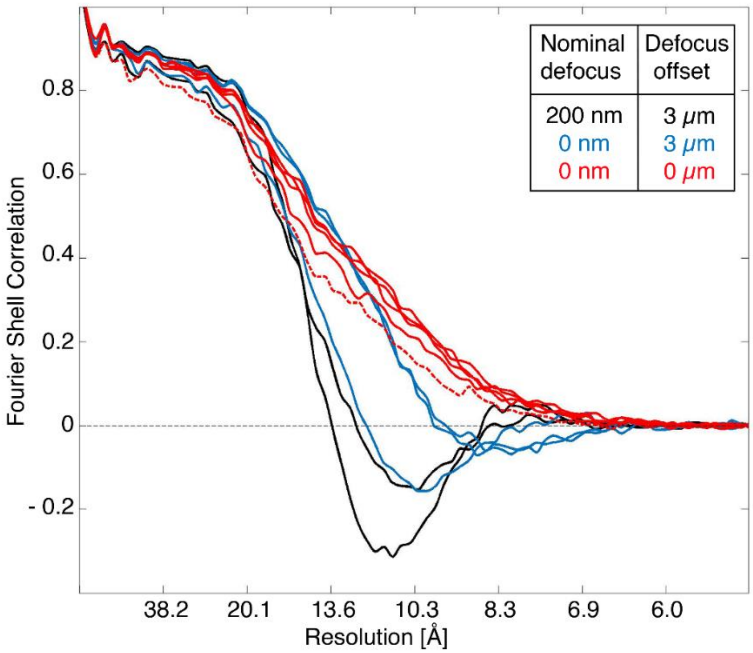

Figure 38: VPP datasets with different focusing parameters. VPP dataset were acquired using several target defocus and defocus offset values. 400 ribosome subvolumes from each tomogram were aligned and averaged to measure FSCR curves against EMD-5592. Figure was adapted from (Khoshouei et al., 2017b).

Figure 39 shows constrained cross-correlation approach to pick each subtomogram. After visualizing five of picked particles, the correct correlation cutoff was used to select the actual ribosome and reject the false positives.

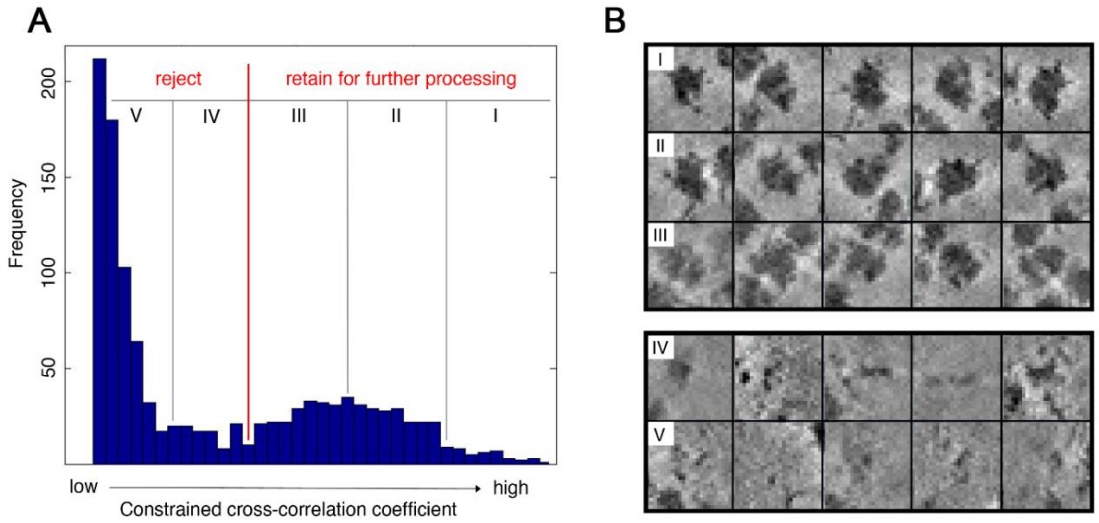

Figure 39: Particle picking using constrained cross-correlation approach. (A) Constrained cross-correlation peaks after template matching. The red line shows the correlation cutoff used for selecting particles. (B) Illustration of five groups of picked particles with different cross-correlation coefficients. Through visual inspection, peaks in sections IV-V were rejected as being false positives. Subtomograms with peaks in sections I-III were selected for further processing. Figure was adapted from (Khoshouei et al., 2017b).

Figure 40A contains curves used to measure the resolution of 1400 averaged subtomograms from the VPP and CTEM datasets at 9.6 Å and 10.6 Å respectively (based on Fourier-shell cross correlation (FSCR) criterion with 0.33 threshold against EMD-5592 (Anger et al., 2013)).

The FSCR curve from CTEM recapitulates oscillations of the CTF at some frequencies showing the reduced SNR in the vicinity of those frequencies while the VPP FSCR curve does not show those oscillations (Figure 40A, B) (Khoshouei et al., 2017b).

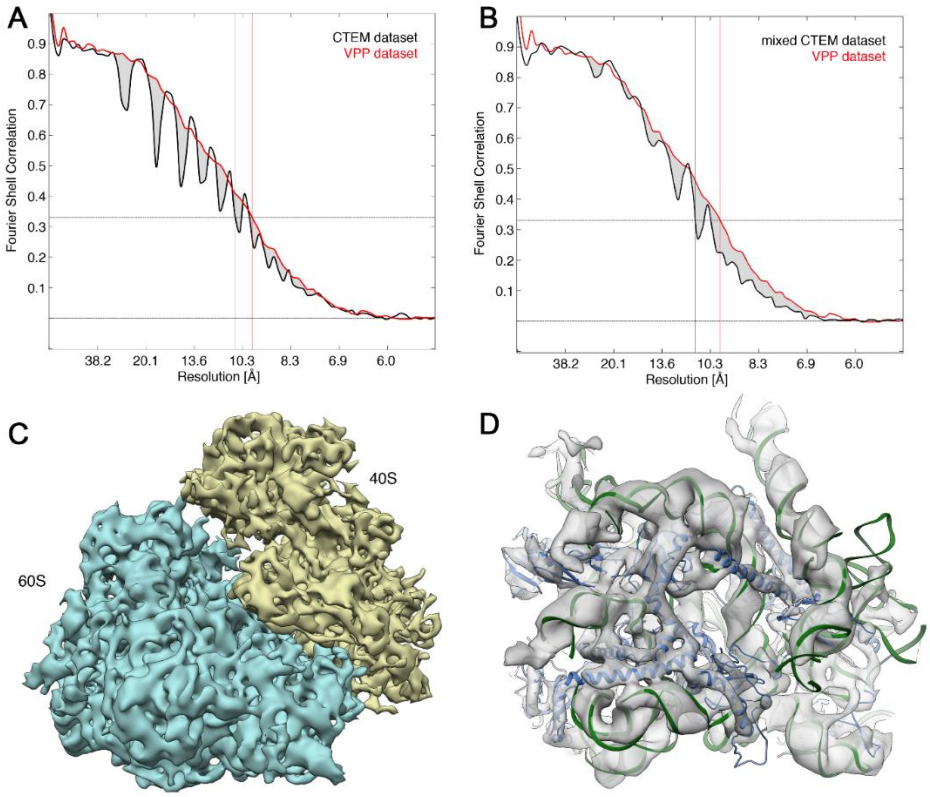

Figure 40: VPP structure of mammalian 80S ribosome. (A) FSCR curves of VPP (red) and CTEM (black) datasets against EMD-5592. The estimated resolutions of the VPP and CTEM subtomogram averages were 9.6 Å and 10.6 Å respectively. (B) FSCR curves of VPP (red) and CTEM with mixed defocus values (black) against EMD-5592 (Anger et al., 2013) showing resolutions of 9.6 Å and 11.2 Å respectively. Gray areas in (A) and (B) illustrate the lower SNR in CTEM due to CTF oscillations. (C) VPP subtomogram structure of ribosome at 9.6 Å resolution. (D) overlaid atomic model of ribosome structure with VPP structure (transparent gray) showing ribosomal RNA region (green) and ribosomal alpha helices (blue). Figure was adopted from (Khoshouei et al., 2017b).

In single particle studies images are taken with a range of defocus values to compensate for the low signal at some frequencies due to CTF oscillations. Several tomograms with varying defocus values, from 2.4 to 3.7 µm, were collected using CTEM in order to determine if the resolution will be improved. Figure 40B shows the FSCR curves from VPP (red) and mixed CTEM (black) datasets. Less oscillations are evident in the mixed CTEM compared to single defocus CTEM but there is still some missing information in the grey areas. Structures from the two CTEM defocus strategies are shown in Figure 41 with superimposed EMD

5592 atomic model. Some details such as RNA double helix (green) and alpha helices (blue) were well visible in this resolution range (Figure 41B and D). The structure from the mixed defocus (2.4, 3.0, 3.3 and 3.7 µm) yielded a resolution of 11.2 Å (Figure 41C and D) (Anger et al., 2013; Khoshouei et al., 2017b).

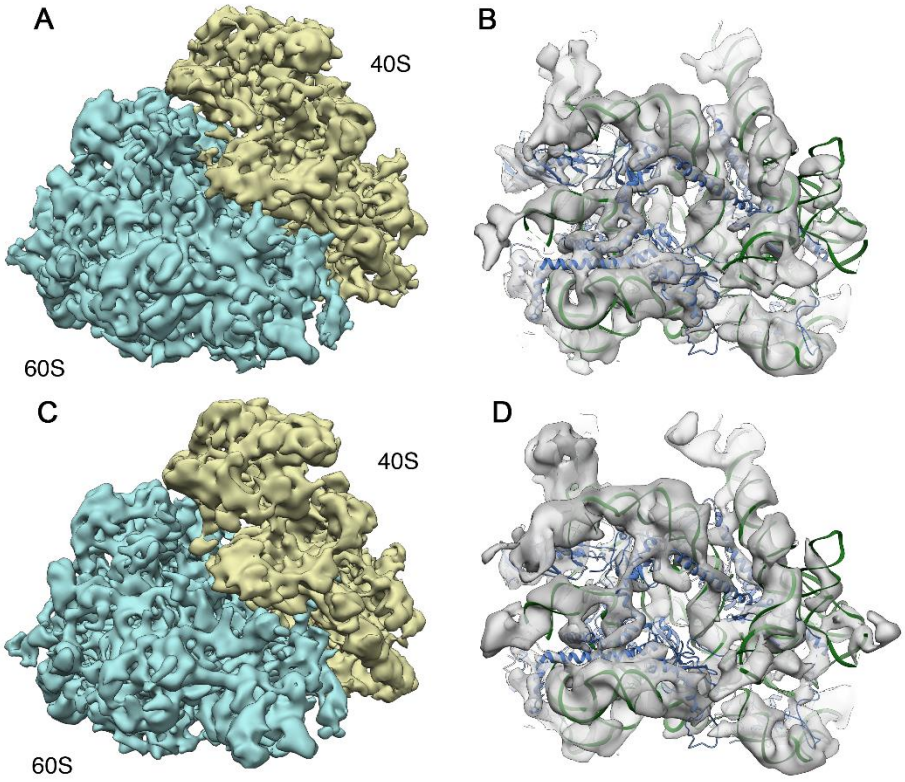

Figure 41: CTEM structures of 80S ribosome. (A) Subtomogram average structure of 80S ribosome taken with a single defocus. (B) overlaid EMD-5592 (Anger et al., 2013) atomic model with the structure in (A). (C) Subtomogram average structure of 80S ribosome taken with a range of defocus values. (D) overlaid EMD-5592 (Anger et al., 2013) atomic model with the structure in (C). Figure was adopted from (Khoshouei et al., 2017b).

In order to examine the relation between the obtainable resolution and the number of subtomograms from VPP and CTEM, different size of aligned subsets of ribosome subtomograms were averaged. Figure 42 shows the FSCR curves for each strategy. For each subset of subtomograms the achieved resolution from VPP dataset was higher meaning that lower number of VPP subtomograms are needed to get the same resolution than with CTEM (Figure 42D). In that context, it is beneficial to use VPP in cellular tomography where fewer copies of a given protein are available (Khoshouei et al., 2017b).

The areas under FSCR was measured as a function the number of averaged subtomograms (Figure 42A-C and Figure 42E). Figure 42E indicates higher signal content in averages from the VPP dataset than the CTEM approches (by around 7%). The averages of subtomogram subsets were calculated using the shifts

and rotations from the global 1400 subtomogram alignment (solid curves) or were re-aligned within each subset (dashed lines) (Figure 42E) (Khoshouei et al., 2017b).

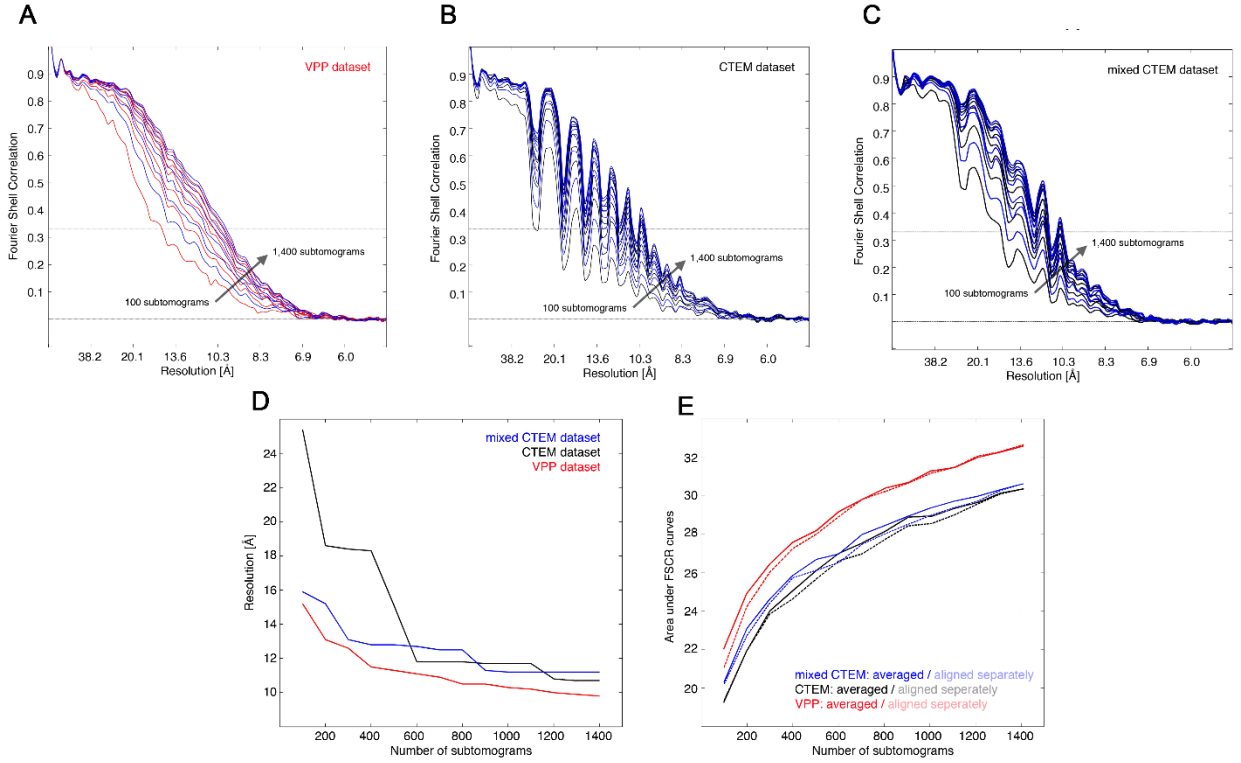

Figure 42: FSCR curves for differently sized subtomogram subsets and dependence of achieved resolution on the number of subtomograms. (A) VPP FSCR (B) CTEM FSCR and (C) mixed defocus CTEM FSCR curves against EMD-5592 (Anger et al., 2013). (D) Resolution plots against the number of subtomograms for the three datasets. (E) Area under the FSCR curves against the number of subtomograms. The solid lines refer to calculated averages using shifts and rotations determined from 1400 subtomograms. The dashed lines refer to calculated averages using the alignments within each subset of subtomograms. Figure was adopted from (Khoshouei et al., 2017b).

The difference between dashed lines and solid lines in Figure 42E was a result of the lower SNR in the iteratively updated reference for smaller subset of particles. This difference was comparable between all three approaches (Khoshouei et al., 2017b).

FSCR curves from individual aligned subtomograms were computed in order to compare the CTEM datasets with the VPP dataset. As shown inFigure 43, the signal content of the two CTEM approaches was comparable between them, while the VPP dataset showed higher areas under the FSCR curves of individual subtomograms. It should be noted that the FSCR curves were calculated between individual aligned subtomograms and a missing-wedge-modified low-pass filtered high resolution structure of the human Ribosome (EMD-5592) (Anger et al., 2013; Khoshouei et al., 2017b).

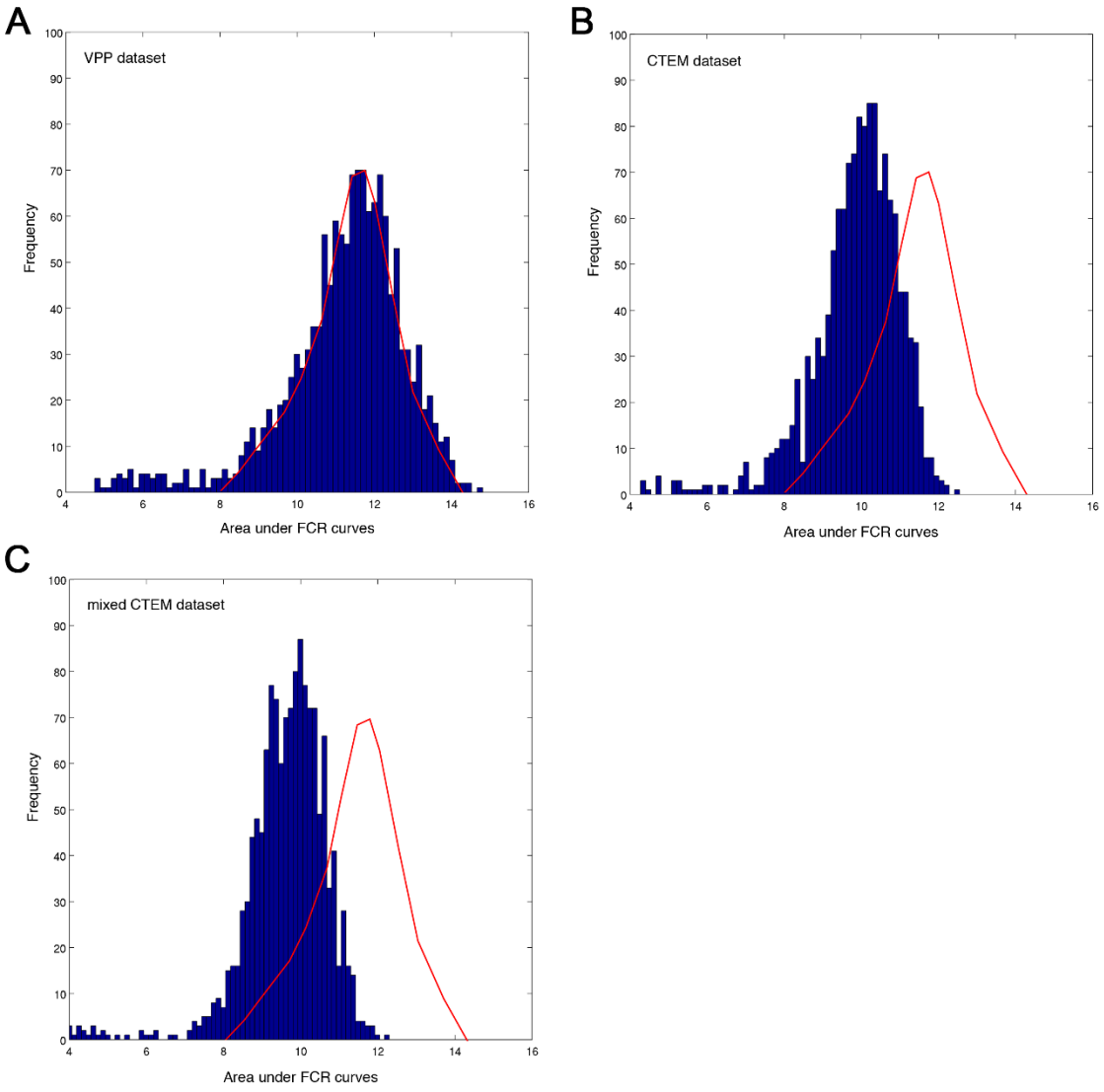

Figure 43: Comparison of the information content of CTEM subtomograms with VPP subtomograms. Distribution of the area under FCR curves of (A) VPP dataset, (B) CTEM dataset at a single defocus value, (C) CTEM dataset with mixed defocus values. The red curve represents the VPP distribution for comparison with the CTEM datasets. Figure was adopted from (Khoshouei et al., 2017b).

4. Conclusion and Outlook

This thesis indicated the use of a heated amorphous carbon film as a VPP positioned at the back focal plane of the objective lens of the TEM. As a result, the central diffraction beam interacts with the thin film containg dangling carbon atoms which modifies the physical and chemical properties of the carbon film surface. Therefore, a negative Volta potential results in a phase shift between unscattered central beam and the scattered ones causing increased contrast in the image. The phase shift coming from the intergration of a 3D electrostatic potential along the beam path above and below the surface of the carbon film is not constant and increases with the accumulated electron dose. The advantage of the VPP are longer life time, no fringing artefacts, the ease of use and possibility for automated data acquisition.

As the first application of the VPP in SPA in the current thesis, Prx3 structure was solved at near atomic resolution. This application shows the possibilities offered by the in-focus VPP imaging in the study of more challenging samples in terms of molecular size, preferred orientation in thin ice or having high salt and Glycerol concentration in the buffer which decrease the SNR of cryo-em images. In addition, the VPP could become a replacement for negative staining methods to optimize the sample for cryo-em in the native state.

Moreover, VPP helped in obtaining the structure of a class B GPCR-G-protein complex which was not solved by cryo-em. VPP imaging delivered insights into flexibility and conformational change of this complex in two parts of a peptide agonist binding site and alpha helical domains. This application could show the possibility of using the VPP for design and drug development of the class B GPCRs.

Furthermore, VPP demonstrated breaking the barriers in cryo-em filed in terms of the structure determination of the smallest protein complex up to date. Human Hb structure reached 3.2 Å resolution which is an indication for the possibility of solving the structure of small complexes which could not be studied by X-ray crystallography.

CET was the second application of the VPP. At first, VPP was used for cellular tomography which enabled understanding of the morphology of the whole vitrified cell. The improved contrast provided by the VPP caused understanding some fine details of the sperm cell from a Lumbricus terrestris earth worm which was not studied before.

Lastly, VPP was used for subtomogram averaging of isolated ribosomes. It was shown that signal transfer was continuous over the whole frequency region from the VPP dataset compared to the conventional dataset. Contrast from the VPP dataset was considerably improved. The resolution from the VPP dataset was 1 Å better compared to the conventional dataset with the same number of subtomograms. At the end, less subtomograms were needed to obtain averages with a comparable resolution which is an important factor in cellular tomography where the number of identical macromolecular complexes is limited to be averaged.

A Appendix

Abbreviations

Å	= Angstrom
LM	= Light microscope
EM	= Electron microscopes
CTF	= Contrast transfer function
SPA	= Single particle analysis
CET	= Cryo-electron tomography
SEM	= Scanning electron microscope
Cryo-FIB	= Cryo-focused ion beam
Cryo-TEM	= Cryo-transmission electron microscopy
STEM	= Scanning transmission electron microscopy
FEG	= Field emission gun
TEM	= Transmission electron microscope
CCD	= Charged coupled device
DQE	= Detective quantum efficiency
CMOS	= Complementary metal-oxide-semiconductor
DDD	= Direct detection device
Cryo-EM	= Cryo-electron microscopy
CTEM	= Conventional transmission electron microscopy
2D	= Two dimensional
3D	= Three dimensional

ML = Maximum likelihood

FSC = Fourier shell correlation

VPP = Volta phase plate

ZPP = Zernike phase plate

BIPS = Beam-induced phase shift

SNR = Signal-to-noise ratio

PDB = Protein data bank

Prxs = Peroxiredoxins

Prx3 = Peroxiredoxin3

C-terminal = Carboxy terminal

GPCRs = G-protein-coupled receptors

Hgb = Human haemoglobin

kDa = Kilo dalton

NMR = Nuclear magnetic resonance

Ni-IMAC = Nickel immobilized metal affinity chromatography

LMNG = Lauryl maltose neopentyl glycol

NAMD = Nanoscale molecular dynamics

ML = Maximum likelihood

MDFF = Molecular dynamic flexible fitting

ACD = Anticontamination device

Bibliography

Abrishami, V., Vargas, J., Li, X., Cheng, Y., Marabini, R., Sorzano, C.O., and Carazo, J.M. (2015). Alignment of direct detection device micrographs using a robust Optical Flow approach. J Struct Biol *189*, 163-176.

Adams, P.D., Afonine, P.V., Bunkoczi, G., Chen, V.B., Davis, I.W., Echols, N., Headd, J.J., Hung, L.W., Kapral, G.J., Grosse-Kunstleve, R.W.*, et al.* (2010). PHENIX: a comprehensive Python-based system for macromolecular structure solution. Acta Crystallogr D Biol Crystallogr *66*, 213-221.

Anderson, W.A., Weissman, A., and Ellis, R.A. (1967). Cytodifferentiation during spermiogenesis in Lumbricus terrestris. J Cell Biol *32*, 11-26.

Anger, A.M., Armache, J.-P., Berninghausen, O., Habeck, M., Subklewe, M., Wilson, D.N., and Beckmann, R. (2013). Structures of the human and Drosophila 80S ribosome. Nature *497*, 80-85.

Asano, S., Fukuda, Y., Beck, F., Aufderheide, A., Forster, F., Danev, R., and Baumeister, W. (2015). Proteasomes. A molecular census of 26S proteasomes in intact neurons. Science *347*, 439-442.

Bai, X.C., McMullan, G., and Scheres, S.H. (2015a). How cryo-EM is revolutionizing structural biology. Trends Biochem Sci *40*, 49-57.

Bai, X.C., Yan, C., Yang, G., Lu, P., Ma, D., Sun, L., Zhou, R., Scheres, S.H.W., and Shi, Y. (2015b). An atomic structure of human gamma-secretase. Nature *525*, 212-217.

Bartesaghi, A., Merk, A., Banerjee, S., Matthies, D., Wu, X., Milne, J.L., and Subramaniam, S. (2015). 2.2 A resolution cryo-EM structure of beta-galactosidase in complex with a cell-permeant inhibitor. Science *348*, 1147-1151.

Bauerlein, F.J.B., Saha, I., Mishra, A., Kalemanov, M., Martinez-Sanchez, A., Klein, R., Dudanova, I., Hipp, M.S., Hartl, F.U., Baumeister, W.*, et al.* (2017). In Situ Architecture and Cellular Interactions of PolyQ Inclusions. Cell.

Ben-Shem, A., Jenner, L., Yusupova, G., and Yusupov, M. (2010). Crystal Structure of the Eukaryotic Ribosome. Science *330*, 1203-1209.

Boersch, H. (1947). Über die Kontraste von Atomen im Elektronenmikroskop. Zeitschrift für Naturforschung A *2*, 615-633.

Boitrelle, F., Albert, M., Petit, J.M., Ferfouri, F., Wainer, R., Bergere, M., Bailly, M., Vialard, F., and Selva, J. (2013). Small human sperm vacuoles observed under high magnification are pocket-like nuclear concavities linked to chromatin condensation failure. Reprod Biomed Online *27*, 201-211.

Briggs, J.A. (2013). Structural biology in situ--the potential of subtomogram averaging. Curr Opin Struct Biol *23*, 261-267.

Brown, A., Long, F., Nicholls, R.A., Toots, J., Emsley, P., and Murshudov, G. (2015). Tools for macromolecular model building and refinement into electron cryo-microscopy reconstructions. Acta Crystallogr D Biol Crystallogr *71*, 136-153.

Cao, Z., Roszak, A.W., Gourlay, L.J., Lindsay, J.G., and Isaacs, N.W. (2005). Bovine mitochondrial peroxiredoxin III forms a two-ring catenane. Structure *13*, 1661-1664.

Chan, K.Y., Trabuco, L.G., Schreiner, E., and Schulten, K. (2012). Cryo-electron microscopy modeling by the molecular dynamics flexible fitting method. Biopolymers *97*, 678-686.

Cheng, Y., Grigorieff, N., Penczek, P.A., and Walz, T. (2015). A primer to single-particle cryo-electron microscopy. Cell *161*, 438-449.

Congreve, M., and Marshall, F. (2010). The impact of GPCR structures on pharmacology and structure-based drug design. Br J Pharmacol *159*, 986-996.

Crowther, R.A., DeRosier, D.J., and Klug, A. (1970). The reconstruction of a three-dimensional structure from projections and its application to electron microscopy. Proceedings of the Royal Society of London A Mathematical and Physical Sciences *317*, 319-340.

D'Haese, J., and Hinssen, H. (1987). Isolation and characterization of a Ca2+-activated actin-modulating protein from obliquely striated muscle. Journal of Comparative Physiology B *157*, 615-623.
Danev, R., and Baumeister, W. (2016). Cryo-EM single particle analysis with the Volta phase plate. Elife *5*.
Danev, R., Buijsse, B., Khoshouei, M., Plitzko, J.M., and Baumeister, W. (2014). Volta potential phase plate for in-focus phase contrast transmission electron microscopy. Proc Natl Acad Sci U S A *111*, 15635-15640.
Danev, R., Glaeser, R.M., and Nagayama, K. (2009). Practical factors affecting the performance of a thin-film phase plate for transmission electron microscopy. Ultramicroscopy *109*, 312-325.
Danev, R., Kanamaru, S., Marko, M., and Nagayama, K. (2010). Zernike phase contrast cryo-electron tomography. J Struct Biol *171*, 174-181.
Danev, R., and Nagayama, K. (2001a). Complex Observation in Electron Microscopy. II. Direct Visualization of Phases and Amplitudes of Exit Wave Functions. Journal of the Physical Society of Japan *70*, 696-702.
Danev, R., and Nagayama, K. (2001b). Transmission electron microscopy with Zernike phase plate. Ultramicroscopy *88*, 243-252.
Danev, R., and Nagayama, K. (2008). Single particle analysis based on Zernike phase contrast transmission electron microscopy. Journal of Structural Biology *161*, 211-218.
Danev, R., and Nagayama, K. (2010). Phase plates for transmission electron microscopy. Methods Enzymol *481*, 343-369.
Danev, R., and Nagayama, K. (2011). Optimizing the phase shift and the cut-on periodicity of phase plates for TEM. Ultramicroscopy *111*, 1305-1315.
Danev, R., Tegunov, D., and Baumeister, W. (2017). Using the Volta phase plate with defocus for cryo-EM single particle analysis. Elife *6*.
De Rosier, D.J., and Klug, A. (1968). Reconstruction of Three Dimensional Structures from Electron Micrographs. Nature *217*, 130-134.
Downing, K.H., McCartney, M.R., and Glaeser, R.M. (2004). Experimental characterization and mitigation of specimen charging on thin films with one conducting layer. Microsc Microanal *10*, 783-789.
Drewes, C.D., and Pax, R.A. (1974). Neuromuscular physiology of the longitudinal muscle of the earthworm, Lumbricus terrestris. 3. Mapping of motor fields. J Exp Biol *60*, 469-475.
Dubochet, J., and McDowall, A.W. (1981). Vitrification of pure water for electron microscopy. Journal of Microscopy *124*, 3-4.
Eibauer, M., Hoffmann, C., Plitzko, J.M., Baumeister, W., Nickell, S., and Engelhardt, H. (2012). Unraveling the structure of membrane proteins in situ by transfer function corrected cryo-electron tomography. Journal of Structural Biology *180*, 488-496.
Elbaum, M., Wolf, S.G., and Houben, L. (2016). Cryo-scanning transmission electron tomography of biological cells. MRS Bulletin *41*, 542-548.
Emsley, P., Lohkamp, B., Scott, W.G., and Cowtan, K. (2010). Features and development of Coot. Acta Crystallogr D Biol Crystallogr *66*, 486-501.
Ferraguti, M., and Jamieson, B.G.M. (1987). Spermiogenesis in Bythonomus lemani and the phylogenetic position of the Lumbriculidae (Oligochaeta, Annelida). In Aquatic Oligochaeta: Proceedings of the Third International Symposium on Aquatic Oligochaeta held in Hamburg, Germany September 29-October 4, 1985, R.O. Brinkhurst, and R.J. Diaz, eds. (Dordrecht: Springer Netherlands), pp. 123-134.
Forster, F., and Hegerl, R. (2007). Structure determination in situ by averaging of tomograms. Methods Cell Biol *79*, 741-767.
Förster, F., Villa, E., Thomas, D., Korinek, A., and Baumeister, W. (2012). 1.14 Structure Determination of Macromolecular Complexes by Cryo-Electron Microscopy in vitro and in situ A2 - Egelman, Edward H. In Comprehensive Biophysics (Amsterdam: Elsevier), pp. 245-276.
Frank, J., Shimkin, B., and Dowse, H. (1981). SPIDER-a modular software system for electron image processing. Ultramicroscopy *6*, 343–358.

Frank, J., and van Heel, M. (1982). Correspondence analysis of aligned images of biological particles. J Mol Biol *161*, 134-137.
Frank, J.J. (2006). Three-dimensional electron microscopy of macromolecular assemblies visualization of biological molecules in their native state, 2 edition edn (Oxford University Press).
Fukuda, Y., Beck, F., Plitzko, J.M., and Baumeister, W. (2017). In situ structural studies of tripeptidyl peptidase II (TPPII) reveal spatial association with proteasomes. Proc Natl Acad Sci U S A *114*, 4412-4417.
Fukuda, Y., Fukazawa, Y., Danev, R., Shigemoto, R., and Nagayama, K. (2009). Tuning of the Zernike phase-plate for visualization of detailed ultrastructure in complex biological specimens. J Struct Biol *168*, 476-484.
Fukuda, Y., Laugks, U., Lucic, V., Baumeister, W., and Danev, R. (2015). Electron cryotomography of vitrified cells with a Volta phase plate. J Struct Biol *190*, 143-154.
Furuhata, M., Danev, R., Nagayama, K., Yamada, Y., Kawakami, H., Toma, K., Hattori, Y., and Maitani, Y. (2008). Decaarginine-PEG-artificial lipid/DNA complex for gene delivery: nanostructure and transfection efficiency. J Nanosci Nanotechnol *8*, 2308-2315.
Gatenby, J.B., and Dalton, A.J. (1959). Spermiogenesis in Lumbricus herculeus; an electron microscope study. J Biophys Biochem Cytol *6*, 45-52.
Glaeser, R.M. (1999). Review: electron crystallography: present excitement, a nod to the past, anticipating the future. J Struct Biol *128*, 3-14.
Glaeser, R.M. (2016). How good can cryo-EM become? Nat Methods *13*, 28-32.
Goddard, T.D., Huang, C.C., and Ferrin, T.E. (2007). Visualizing density maps with UCSF Chimera. J Struct Biol *157*, 281-287.
Goldstein, J.I., Newbury, D.E., Echlin, P., Joy, D.C., Lyman, C.E., Lifshin, E., Sawyer, L., and Michael, J.R. (2003). The SEM and Its Modes of Operation. In Scanning Electron Microscopy and X-ray Microanalysis: Third Edition (Boston, MA: Springer US), pp. 21-60.
Grigorieff, N. (2007). FREALIGN: high-resolution refinement of single particle structures. J Struct Biol *157*, 117-125.
Henderson, R. (1995). The potential and limitations of neutrons, electrons and X-rays for atomic resolution microscopy of unstained biological molecules. Q Rev Biophys *28*, 171-193.
Henderson, R., and Unwin, P.N.T. (1975). Three-dimensional model of purple membrane obtained by electron microscopy. Nature *257*, 28-32.
Henley, C. (1973). Ultrastructure of the spermatozoon of the earthworm as revealed by negative staining. Journal of Morphology *140*, 197-213.
Hohn, M., Tang, G., Goodyear, G., Baldwin, P.R., Huang, Z., Penczek, P.A., Yang, C., Glaeser, R.M., Adams, P.D., and Ludtke, S.J. (2007). SPARX, a new environment for Cryo-EM image processing. J Struct Biol *157*, 47-55.
Hoppert, M. (2005a). Electron Microscopy. In Microscopic Techniques in Biotechnology (Wiley-VCH Verlag GmbH & Co. KGaA), pp. 147-286.
Hoppert, M. (2005b). Light Microscopy. In Microscopic Techniques in Biotechnology (Wiley-VCH Verlag GmbH & Co. KGaA), pp. 1-145.
Hrabe, T., Chen, Y., Pfeffer, S., Kuhn Cuellar, L., Mangold, A.-V., and Förster, F. (2012). PyTom: A python-based toolbox for localization of macromolecules in cryo-electron tomograms and subtomogram analysis. Journal of Structural Biology *178*, 177-188.
Huang, B., Bates, M., and Zhuang, X. (2009). Super-resolution fluorescence microscopy. Annu Rev Biochem *78*, 993-1016.
Jamieson, B. (1978). A comparison of spermiogenesis and spermatozoal ultrastructure in Megascolecid and Lumbricid earthworms (Oligochaeta : Annelida). Australian Journal of Zoology *26*, 225-240.
Jamieson, B.G.M. (1982). The ultrastructure of the spermatozoon of Haplotaxis ornamentus (Annelida, Oligochaeta, Haplotaxidae) and its phylogenetic significance. Zoomorphology *100*, 177-188.

Jazayeri, A., Rappas, M., Brown, A.J.H., Kean, J., Errey, J.C., Robertson, N.J., Fiez-Vandal, C., Andrews, S.P., Congreve, M., Bortolato, A.*, et al.* (2017). Crystal structure of the GLP-1 receptor bound to a peptide agonist. Nature *546*, 254-258.

Johnson, H.M., and Parsons, D.F. (1973). Enhanced contrast in electron microscopy of unstained biological material. 3. In-focus phase contrast of large objects. J Microsc *98*, 1-17.

Kendrew, J.C. (1962). Myoglobin and the structure of proteins. Nobel Lecture, 676-677.

Kendrew, J.C., Bodo, G., Dintzis, H.M., Parrish, R.G., Wyckoff, H., and Phillips, D.C. (1958). A three-dimensional model of the myoglobin molecule obtained by x-ray analysis. Nature *181*, 662-666.

Kendrew, J.C., Dickerson, R.E., Strandberg, B.E., Hart, R.G., Davies, D.R., Phillips, D.C., and Shore, V.C. (1960). Structure of myoglobin: A three-dimensional Fourier synthesis at 2 A. resolution. Nature *185*, 422-427.

Khoshouei, M., Danev, R., Plitzko, J.M., and Baumeister, W. (2017a). Revisiting the Structure of Hemoglobin and Myoglobin with Cryo-Electron Microscopy. J Mol Biol *429*, 2611-2618.

Khoshouei, M., Pfeffer, S., Baumeister, W., Forster, F., and Danev, R. (2017b). Subtomogram analysis using the Volta phase plate. J Struct Biol *197*, 94-101.

Khoshouei, M., Radjainia, M., Baumeister, W., and Danev, R. (2017c). Cryo-EM structure of haemoglobin at 3.2 A determined with the Volta phase plate. Nat Commun *8*, 16099.

Khoshouei, M., Radjainia, M., Phillips, A.J., Gerrard, J.A., Mitra, A.K., Plitzko, J.M., Baumeister, W., and Danev, R. (2016). Volta phase plate cryo-EM of the small protein complex Prx3. Nat Commun *7*, 10534.

Kremer, J.R., Mastronarde, D.N., and McIntosh, J.R. (1996). Computer visualization of three-dimensional image data using IMOD. J Struct Biol *116*, 71-76.

Krüger, E., Hinssen, H., and D'Haese, J. (2008). Involvement of a gelsolin-related protein in spermatogenesis of the earthworm Lumbricus terrestris, Vol 332.

Kuhlbrandt, W. (2014). Biochemistry. The resolution revolution. Science *343*, 1443-1444.

Lasker, K., Forster, F., Bohn, S., Walzthoeni, T., Villa, E., Unverdorben, P., Beck, F., Aebersold, R., Sali, A., and Baumeister, W. (2012). Molecular architecture of the 26S proteasome holocomplex determined by an integrative approach. Proc Natl Acad Sci U S A *109*, 1380-1387.

Li, X., Mooney, P., Zheng, S., Booth, C.R., Braunfeld, M.B., Gubbens, S., Agard, D.A., and Cheng, Y. (2013). Electron counting and beam-induced motion correction enable near-atomic-resolution single-particle cryo-EM. Nat Meth *10*, 584-590.

Liang, B., Li, Z., Jenni, S., Rahmeh, A.A., Morin, B.M., Grant, T., Grigorieff, N., Harrison, S.C., and Whelan, S.P.J. (2015). Structure of the L Protein of Vesicular Stomatitis Virus from Electron Cryomicroscopy. Cell *162*, 314-327.

Liang, Y.L., Khoshouei, M., Radjainia, M., Zhang, Y., Glukhova, A., Tarrasch, J., Thal, D.M., Furness, S.G.B., Christopoulos, G., Coudrat, T.*, et al.* (2017). Phase-plate cryo-EM structure of a class B GPCR-G-protein complex. Nature *546*, 118-123.

Liao, M., Cao, E., Julius, D., and Cheng, Y. (2013). Structure of the TRPV1 ion channel determined by electron cryo-microscopy. Nature *504*, 107-112.

Lučić, V., Rigort, A., and Baumeister, W. (2013). Cryo-electron tomography: The challenge of doing structural biology in situ. The Journal of Cell Biology *202*, 407-419.

Mahamid, J., Pfeffer, S., Schaffer, M., Villa, E., Danev, R., Cuellar, L.K., Forster, F., Hyman, A.A., Plitzko, J.M., and Baumeister, W. (2016). Visualizing the molecular sociology at the HeLa cell nuclear periphery. Science *351*, 969-972.

Malac, M., Beleggia, M., Kawasaki, M., Li, P., and Egerton, R.F. (2012). Convenient contrast enhancement by a hole-free phase plate. Ultramicroscopy *118*, 77-89.

Manglik, A., Kim, T.H., Masureel, M., Altenbach, C., Yang, Z., Hilger, D., Lerch, M.T., Kobilka, T.S., Thian, F.S., Hubbell, W.L.*, et al.* (2015). Structural Insights into the Dynamic Process of beta2-Adrenergic Receptor Signaling. Cell *161*, 1101-1111.

Mastronarde, D.N. (1997). Dual-axis tomography: an approach with alignment methods that preserve resolution. J Struct Biol *120*, 343-352.
Mastronarde, D.N. (2005). Automated electron microscope tomography using robust prediction of specimen movements. J Struct Biol *152*, 36-51.
Matricardi, V.R., Moretz, R.C., and Parsons, D.F. (1972). Electron diffraction of wet proteins: catalase. Science *177*, 268-270.
McMullan, G., Faruqi, A.R., Clare, D., and Henderson, R. (2014). Comparison of optimal performance at 300 keV of three direct electron detectors for use in low dose electron microscopy. In ArXiv e-prints.
Melnikov, S., Ben-Shem, A., Garreau de Loubresse, N., Jenner, L., Yusupova, G., and Yusupov, M. (2012). One core, two shells: bacterial and eukaryotic ribosomes. Nat Struct Mol Biol *19*, 560-567.
Merk, A., Bartesaghi, A., Banerjee, S., Falconieri, V., Rao, P., Davis, M.I., Pragani, R., Boxer, M.B., Earl, L.A., Milne, J.L.S*., et al.* (2016). Breaking Cryo-EM Resolution Barriers to Facilitate Drug Discovery. Cell *165*, 1698-1707.
Moriya, T., Saur, M., Stabrin, M., Merino, F., Voicu, H., Huang, Z., Penczek, P.A., Raunser, S., and Gatsogiannis, C. (2017). High-resolution Single Particle Analysis from Electron Cryo-microscopy Images Using SPHIRE. J Vis Exp.
Müller, H., Jian, J., Danev, R., Spence, J., Padmore, H., and Glaeser, R.M. (2010). Design of an electron microscope phase plate using a focused continuous-wave laser. New Journal of Physics *12*, 073011.
Murata, K., Liu, X., Danev, R., Jakana, J., Schmid, M.F., King, J., Nagayama, K., and Chiu, W. (2010). Zernike phase contrast cryo-electron microscopy and tomography for structure determination at nanometer and subnanometer resolutions. Structure *18*, 903-912.
Murshudov, G.N., Skubak, P., Lebedev, A.A., Pannu, N.S., Steiner, R.A., Nicholls, R.A., Winn, M.D., Long, F., and Vagin, A.A. (2011). REFMAC5 for the refinement of macromolecular crystal structures. Acta Crystallogr D Biol Crystallogr *67*, 355-367.
Nagayama, K., and Danev, R. (2008). Phase contrast electron microscopy: development of thin-film phase plates and biological applications. Philosophical Transactions of the Royal Society B: Biological Sciences *363*, 2153-2162.
Nagayama, K., and Danev, R. (2009). Phase-plate electron microscopy: a novel imaging tool to reveal close-to-life nano-structures. Biophys Rev *1*, 37-42.
Nickell, S., Forster, F., Linaroudis, A., Net, W.D., Beck, F., Hegerl, R., Baumeister, W., and Plitzko, J.M. (2005). TOM software toolbox: acquisition and analysis for electron tomography. J Struct Biol *149*, 227-234.
Nogales, E. (2016). The development of cryo-EM into a mainstream structural biology technique. Nature methods *13*, 24-27.
Nogales, E., and Scheres, S.H. (2015). Cryo-EM: A Unique Tool for the Visualization of Macromolecular Complexity. Mol Cell *58*, 677-689.
Park, S.Y., Yokoyama, T., Shibayama, N., Shiro, Y., and Tame, J.R. (2006). 1.25 A resolution crystal structures of human haemoglobin in the oxy, deoxy and carbonmonoxy forms. J Mol Biol *360*, 690-701.
Penczek, P.A. (2010). Fundamentals of three-dimensional reconstruction from projections. Methods Enzymol *482*, 1-33.
Penczek, P.A., Grassucci, R.A., and Frank, J. (1994). The ribosome at improved resolution: new techniques for merging and orientation refinement in 3D cryo-electron microscopy of biological particles. Ultramicroscopy *53*, 251-270.
Perutz, M.F., Rossmann, M.G., Cullis, A.F., Muirhead, H., Will, G., and North, A.C. (1960). Structure of haemoglobin: a three-dimensional Fourier synthesis at 5.5-A. resolution, obtained by X-ray analysis. Nature *185*, 416-422.
Pigino, G., Bui, K.H., Maheshwari, A., Lupetti, P., Diener, D., and Ishikawa, T. (2011). Cryoelectron tomography of radial spokes in cilia and flagella. J Cell Biol *195*, 673-687.

Punjani, A., Rubinstein, J.L., Fleet, D.J., and Brubaker, M.A. (2017). cryoSPARC: algorithms for rapid unsupervised cryo-EM structure determination. Nat Methods *14*, 290-296.
Rasmussen, S.G., DeVree, B.T., Zou, Y., Kruse, A.C., Chung, K.Y., Kobilka, T.S., Thian, F.S., Chae, P.S., Pardon, E., Calinski, D.*, et al.* (2011). Crystal structure of the beta2 adrenergic receptor-Gs protein complex. Nature *477*, 549-555.
Rawson, S., Davies, S., Lippiat, J.D., and Muench, S.P. (2016). The changing landscape of membrane protein structural biology through developments in electron microscopy. Mol Membr Biol *33*, 12-22.
Reimer, L., and Kohl, H. (2008). Transmission Electron Microscopy Physics of Image Formation, 5 edn (New York, NY: Springer New York).
Rigort, A., Bauerlein, F.J., Leis, A., Gruska, M., Hoffmann, C., Laugks, T., Bohm, U., Eibauer, M., Gnaegi, H., Baumeister, W.*, et al.* (2010). Micromachining tools and correlative approaches for cellular cryo-electron tomography. J Struct Biol *172*, 169-179.
Rigort, A., Bauerlein, F.J., Villa, E., Eibauer, M., Laugks, T., Baumeister, W., and Plitzko, J.M. (2012). Focused ion beam micromachining of eukaryotic cells for cryoelectron tomography. Proc Natl Acad Sci U S A *109*, 4449-4454.
Rohou, A., and Grigorieff, N. (2015). CTFFIND4: Fast and accurate defocus estimation from electron micrographs. J Struct Biol *192*, 216-221.
Rosenbaum, D.M., Cherezov, V., Hanson, M.A., Rasmussen, S.G., Thian, F.S., Kobilka, T.S., Choi, H.J., Yao, X.J., Weis, W.I., Stevens, R.C.*, et al.* (2007). GPCR engineering yields high-resolution structural insights into beta2-adrenergic receptor function. Science *318*, 1266-1273.
Rubinstein, J.L., and Brubaker, M.A. (2015). Alignment of cryo-EM movies of individual particles by optimization of image translations. J Struct Biol *192*, 188-195.
Russo, C.J., and Passmore, L.A. (2016). Ultrastable gold substrates: Properties of a support for high-resolution electron cryomicroscopy of biological specimens. J Struct Biol *193*, 33-44.
Schaffer, M., Mahamid, J., Engel, B.D., Laugks, T., Baumeister, W., and Plitzko, J.M. (2017). Optimized cryo-focused ion beam sample preparation aimed at in situ structural studies of membrane proteins. J Struct Biol *197*, 73-82.
Scheres, S.H. (2012a). A Bayesian view on cryo-EM structure determination. J Mol Biol *415*, 406-418.
Scheres, S.H. (2012b). RELION: implementation of a Bayesian approach to cryo-EM structure determination. J Struct Biol *180*, 519-530.
Scheres, S.H. (2014). Beam-induced motion correction for sub-megadalton cryo-EM particles. Elife *3*, e03665.
Scheres, S.H.W. (2010). Maximum-likelihood methods in cryo-EM. Part II: application to experimental data. Methods in enzymology *482*, 295-320.
Scheres, S.H.W., and Chen, S. (2012). Prevention of overfitting in cryo-EM structure determination. Nat Meth *9*, 853-854.
Schroder, E., Littlechild, J.A., Lebedev, A.A., Errington, N., Vagin, A.A., and Isupov, M.N. (2000). Crystal structure of decameric 2-Cys peroxiredoxin from human erythrocytes at 1.7 A resolution. Structure *8*, 605-615.
Schwartz, O., Axelrod, J.J., Haslinger, P., Ophus, C., Glaeser, R.M., and Müller, H. (2016). Continuous 40 GW/cm2 laser intensity in a near-concentric optical cavity. In ArXiv e-prints.
Schweitzer, A., Aufderheide, A., Rudack, T., Beck, F., Pfeifer, G., Plitzko, J.M., Sakata, E., Schulten, K., Forster, F., and Baumeister, W. (2016). Structure of the human 26S proteasome at a resolution of 3.9 A. Proc Natl Acad Sci U S A *113*, 7816-7821.
Shay, J.W. (1972). Ultrastructural observations on the acrosome of Lumbricus terrestris. J Ultrastruct Res *41*, 572-578.
Shibayama, N., Sugiyama, K., Tame, J.R., and Park, S.Y. (2014). Capturing the hemoglobin allosteric transition in a single crystal form. J Am Chem Soc *136*, 5097-5105.

Shimada, A., Niwa, H., Tsujita, K., Suetsugu, S., Nitta, K., Hanawa-Suetsugu, K., Akasaka, R., Nishino, Y., Toyama, M., Chen, L.*, et al.* (2007). Curved EFC/F-BAR-domain dimers are joined end to end into a filament for membrane invagination in endocytosis. Cell *129*, 761-772.
Sigworth, F.J. (2016). Principles of cryo-EM single-particle image processing. Microscopy (Oxf) *65*, 57-67.
Sigworth, F.J., Doerschuk, P.C., Carazo, J.M., and Scheres, S.H. (2010). An introduction to maximum-likelihood methods in cryo-EM. Methods Enzymol *482*, 263-294.
Song, G., Yang, D., Wang, Y., de Graaf, C., Zhou, Q., Jiang, S., Liu, K., Cai, X., Dai, A., Lin, G.*, et al.* (2017). Human GLP-1 receptor transmembrane domain structure in complex with allosteric modulators. Nature *546*, 312-315.
Steitz, T.A. (2008). A structural understanding of the dynamic ribosome machine. Nat Rev Mol Cell Biol *9*, 242-253.
Strandberg, B., Dickerson, R.E., and Rossmann, M.G. (2009). 50 Years of Protein Structure Analysis. Journal of Molecular Biology *392*, 2-32.
Tang, G., Peng, L., Baldwin, P.R., Mann, D.S., Jiang, W., Rees, I., and Ludtke, S.J. (2007). EMAN2: an extensible image processing suite for electron microscopy. J Struct Biol *157*, 38-46.
Taylor, K.A., and Glaeser, R.M. (1974). Electron diffraction of frozen, hydrated protein crystals. Science *186*, 1036-1037.
Tong, J., Arslan, I., and Midgley, P. (2006). A novel dual-axis iterative algorithm for electron tomography. Journal of Structural Biology *153*, 55-63.
Tosaka, M., Danev, R., and Nagayama, K. (2005). Application of Phase Contrast Transmission Microscopic Methods to Polymer Materials. Macromolecules *38*, 7884-7886.
Tsai, C.J., Standfuss, J., and Glaeser, R.M. (2017). Structural biology: Signalling under the microscope. Nature *546*, 36-37.
van Heel, M., and Frank, J. (1981). Use of multivariate statistics in analysing the images of biological macromolecules. Ultramicroscopy *6*, 187-194.
Vinothkumar, K.R., and Henderson, R. (2016). Single particle electron cryomicroscopy: trends, issues and future perspective. Q Rev Biophys *49*, e13.
Warner, F.D. (1976). Ciliary inter-microtubule bridges. J Cell Sci *20*, 101-114.
Williams, D.B.a.C. (2009). Transmission electron microscopy: A textbook for materials science, 2 edition edn (Springer US, Boston, MA).
Wolf, S.G., Houben, L., and Elbaum, M. (2014). Cryo-scanning transmission electron tomography of vitrified cells. Nat Methods *11*, 423-428.
Wootten, D., Reynolds, C.A., Smith, K.J., Mobarec, J.C., Furness, S.G., Miller, L.J., Christopoulos, A., and Sexton, P.M. (2016a). Key interactions by conserved polar amino acids located at the transmembrane helical boundaries in Class B GPCRs modulate activation, effector specificity and biased signalling in the glucagon-like peptide-1 receptor. Biochem Pharmacol *118*, 68-87.
Wootten, D., Reynolds, C.A., Smith, K.J., Mobarec, J.C., Koole, C., Savage, E.E., Pabreja, K., Simms, J., Sridhar, R., Furness, S.G.B.*, et al.* (2016b). The Extracellular Surface of the GLP-1 Receptor Is a Molecular Trigger for Biased Agonism. Cell *165*, 1632-1643.
Wootten, D., Simms, J., Miller, L.J., Christopoulos, A., and Sexton, P.M. (2013). Polar transmembrane interactions drive formation of ligand-specific and signal pathway-biased family B G protein-coupled receptor conformations. Proc Natl Acad Sci U S A *110*, 5211-5216.
Wuthrich, K. (2001). The way to NMR structures of proteins. Nat Struct Biol *8*, 923-925.
Yamaguchi, M., Danev, R., Nishiyama, K., Sugawara, K., and Nagayama, K. (2008). Zernike phase contrast electron microscopy of ice-embedded influenza A virus. J Struct Biol *162*, 271-276.
Yewdall, N.A., Venugopal, H., Desfosses, A., Abrishami, V., Yosaatmadja, Y., Hampton, M.B., Gerrard, J.A., Goldstone, D.C., Mitra, A.K., and Radjainia, M. (2016). Structures of Human Peroxiredoxin 3 Suggest Self-Chaperoning Assembly that Maintains Catalytic State. Structure *24*, 1120-1129.

Yin, Y., de Waal, P.W., He, Y., Zhao, L.H., Yang, D., Cai, X., Jiang, Y., Melcher, K., Wang, M.W., and Xu, H.E. (2017). Rearrangement of a polar core provides a conserved mechanism for constitutive activation of class B G protein-coupled receptors. J Biol Chem *292*, 9865-9881.

Yoshioka, C., Carragher, B., and Potter, C.S. (2010). Cryomesh: a new substrate for cryo-electron microscopy. Microsc Microanal *16*, 43-53.

Yui, H., Minamikawa, H., Danev, R., Nagayama, K., Kamiya, S., and Shimizu, T. (2008). Growth process and molecular packing of a self-assembled lipid nanotube: phase-contrast transmission electron microscopy and XRD analyses. Langmuir *24*, 709-713.

Zernike, F. (1942). Phase contrast, a new method for the microscopic observation of transparent objects part II. Physica *9*, 974-986.

Zhang, K. (2016a).

Zhang, K. (2016b). Gctf: Real-time CTF determination and correction. J Struct Biol *193*, 1-12.

Zheng, S.Q., Palovcak, E., Armache, J.-P., Verba, K.A., Cheng, Y., and Agard, D.A. (2017). MotionCor2: anisotropic correction of beam-induced motion for improved cryo-electron microscopy. Nat Meth *14*, 331-332.

Publications

Title: Volta potential phase plate for in-focus phase contrast transmission electron microscopy.
Authors: Radostin Danev, Bart Buijsse, **Maryam Khoshouei**, Jürgen M. Plitzko, and Wolfgang Baumeister.
Journal: Proceedings of the National Academy of Sciences of the United States of America
Year: 2014

Title: Removing Contamination-Induced Reconstruction Artifacts from Cryo-electron Tomograms.
Authors: Jose-Jesus Fernandez, Ulrike Laugks, Miroslava Schaffer, Felix J.B. Bäuerlein, **Maryam Khoshouei**, Wolfgang Baumeister, Vladan Lucic.
Journal: Biophysical Journal
Year: 2016

Title: Volta phase plate cryo-EM of the small protein complex Prx3.
Authors: **Maryam Khoshouei**, Mazdak Radjainia, Amy J. Phillips, Juliet A. Gerrard, Alok K. Mitra, Jürgen M. Plitzko, Wolfgang Baumeister & Radostin Danev.
Journal: Nature Communications
Year: 2016

Title: Subtomogram analysis using the Volta phase plate.
Authors: **Maryam Khoshouei** *, Stefan Pfeffer *, Wolfgang Baumeister, Friedrich Förster, Radostin Danev.
Journal: Journal of Structural Biology
Year: 2017

Title: Phase-plate cryo-EM structure of a class B GPCR–G-protein complex.
Authors: Yi-Lynn Liang *, **Maryam Khoshouei** *, Mazdak Radjainia *, Yan Zhang *, Alisa Glukhova, Jeffrey Tarrasch, David M. Thal, Sebastian G. B. Furness, George Christopoulos, Thomas Coudrat, Radostin Danev, Wolfgang Baumeister, Laurence J. Miller, Arthur Christopoulos, Brian K. Kobilka, Denise Wootten, Georgios Skiniotis & Patrick M. Sexton.
* These authors contributed equally
Journal: Nature
Year: 2017

Title: Cryo-EM structure of haemoglobin at 3.2 A determined with the Volta phase plate.
Authors: **Maryam Khoshouei**, Mazdak Radjainia, Wolfgang Baumeister, Radostin Danev.
Journal: Nature Communications
Year: 2017

Title: Isolation and characterization of Metallosphaera turreted icosahedral virus, a founding member of a new family of archael viruses.
Authors: Cassia Wagner, Vijay Reddy, Francisco Asturias, **Maryam Khoshouei**, John E. Johnson, Pilar Manrique, Jacob Munson-McGee, Wolfgang Baumeister, C. Martin Lawrence, Mark J. Young.
Journal: Journal of Virology
Year: 2017

Title: Revisiting the Structure of Hemoglobin and Myoglobin with Cryo-Electron Microscopy.
Authors: **Maryam Khoshouei**, RadostinDanev, Juergen M.Plitzko, Wolfgang Baumeister.
Journal: Journal of Molecular Biology
Year: 2017

Title: Phase-plate cryo-EM structure of a biased agonistbound human GLP-1 receptor–Gs complex.
Authors: Yi-Lynn Liang *, **Maryam Khoshouei** *, Alisa Glukhova *, Sebastian G. B. Furness, Peishen Zhao, Lachlan Clydesdale, Cassandra Koole, Tin T. Truong, David M. Thal, Saifei Lei, Mazdak Radjainia, Radostin Danev, Wolfgang Baumeister, Ming-Wei Wang, Laurence J. Miller, Arthur Christopoulos, Patrick M. Sexton & Denise Wootten.
* These authors contributed equally
Journal: Nature
Year: 2018

Title:Cryo-EM structure of the human adenosine A1 receptor-Gi2-protein complex bound to its endogenous agonist.
Authors: Christopher J. Draper-Joyce *, **Maryam Khoshouei** *, David M. Thal, Yi-Lynn Liang, Anh T.N. Nguyen, Sebastian G.B. Furness, Hariprasad Venugopal, Jo-Anne Baltos, Jürgen M Plitzko, Radostin Danev, Wolfgang Baumeister, Lauren T. May, Denise Wootten, Patrick M. Sexton, Alisa Glukhova, Arthur Christopoulos.
* These authors contributed equally
Journal: Nature
Year: 2018

Title: Cryo-EM structure of the active, Gs-protein complexed, human CGRP receptor.
Authors: Yi-Lynn Liang *, **Maryam Khoshouei** *, Giuseppe Deganutti, Alisa Glukhova, Cassandra Koole, Thomas S. Peat, Mazdak Radjainia, Jürgen M. Plitzko, Wolfgang Baumeister, Laurence J. Miller, Deborah L. Hay, Arthur Christopoulos, Christopher A Reynolds, Denise Wootten, Patrick M. Sexton.
* These authors contributed equally
Journal: Nature
Year: 2018

Acknowledgements

The completion of my PhD journey was made possible by the support and encouragement of many people including my family, mentors, friends and colleagues. It is a pleasure for me to express my deepest appreciations to all the people who contributed to this thesis in different ways. Foremost, I would like to thank Prof. Wolfgang Baumeister for giving me the opportunity to pursue my PhD studies and providing access to the wonderful infrastructure that we have at Max Planck Institute of Biochemistry in Martinsried. I extend my sincere gratitude to my PhD advisor, Dr. Radostin Danev, for accepting me as his PhD student and mentoring me each step of the way. I convey my deep gratitude for his guidance, constructive suggestions and fruitful discussions. His profound knowledge in phase contrast cryo-electron microscopy inspired me to pursue my studies in this field.

At this moment of accomplishment, I would like to thank all members of Prof. Baumeister's department, in particular my friends Ulrike and Tim Laugks for their tremendous help and support, especially with navigating the German language. Their friendship will always stay in my heart and mind. I greatly appreciate the constant support from Prof. Dr. Juergen Plitzko and Guenter Pfeifer, who have taught me much about electron microscopy and also ensure that the electron microscopes are running smoothly. I take this opportunity to thank Birgit Book and Nathalie Leclercq for their assistance, especially with paperwork and logistics, as well as continuous support with the German language. I would like to thank Inga Wolf and Florian Beck for their assistance with computers, software and troubleshooting. I am thankful to my colleagues and collaborators who were involved in projects I was doing during my studies, especially to Dr. Guenther Gerisch, Mary Ecke, Dr. Benjamin Engel and Dr. Julio Ortiz for the worm sperm project, and Dr. Stefan Pfeffer and Prof. Dr. Friedrich Foerster for the ribosome subtomogram averaging project. I convey my gratefulness to Dr. Mazdak Radjainia, Dr. Lynn Liang, Dr. Denise Wootten and Prof. Partrick Sexton for close collaborations that led to outstanding results.

I am indebted to my grandfather for his sincere encouragement and inspiration. He was hoping to see the day when I finish my PhD studies. I wish that his soul rests in peace and solace in heaven. My special gratitude and love go to my parents for their unfailing support and abiding love. They stood by me constantly, throughout difficult times in my research and private life.
Special and profound thanks to my brother who offered invaluable support over the last years in helping take care of my son, Matin. Not only spending time with Matin but also being a role model for him. Last

but not least, my deepest love and thanks goes to Matin for being the pride and joy of my life, who has been beside me all the time. No words can express how much I love Matin. I appreciate all his patience during my studies. I dedicate my PhD thesis to Matin, and I am looking forward to seeing his success in life.